Mon. Not. R. astr. Soc. (1985) **216,** 273–334

Elliptical galaxies with separable potentials

Tim de Zeeuw* *Sterrewacht Leiden, Postbus 9513, 2300 RA Leiden, The Netherlands*

Accepted 1985 March 12. Received 1985 March 12; in original form 1984 June 25

Summary. The perfect ellipsoid is presented: an inhomogeneous triaxial mass model with a gravitational potential that is of Stäckel form. The equations of motion are separable in ellipsoidal coordinates and all stellar orbits have three isolating integrals that are known explicitly. The orbital structure in the perfect ellipsoid is generic for all centrally concentrated triaxial mass models with a finite central density and a Stäckel potential, and it is tractable by analytic means. The orbital shapes are classified in terms of the values of the integrals of motion. This classification becomes particularly transparent in terms of the action integrals. Individual orbit densities can be computed without integration of the equations of motion, and some examples are shown. There are four families of general orbits: boxes, inner and outer long axis tubes and short axis tubes. These are identical to the major orbit families that occur in Schwarzschild's ellipsoid and are thought to be of prime importance for the structure of elliptical galaxies. Special values of the axis ratios of the perfect ellipsoid lead to a simpler orbital structure. The prolate, oblate and spherical limits are treated, as well as the elliptic and circular discs and the needle. The existence of the perfect ellipsoid shows that ellipsoidal coordinates are the natural coordinates for the description of triaxial systems. The relevance of mass models with Stäckel potentials for the construction of self-consistent models of elliptical galaxies is discussed.

1 Introduction

A realistic self-consistent equilibrium model for an elliptical galaxy should have at least the two following properties:

(i) The density distribution must be stratified on concentric, nearly ellipsoidal surfaces. Such a triaxial mass model is the simplest model that is compatible with the observed brightness contours of ellipticals.

(ii) Most individual stellar orbits in it must possess three independent isolating integrals of motion, i.e. two in addition to the energy integral. These integrals are required in order to

*Present address: Institute for Advanced Study, Princeton, NJ 08540, USA.

maintain the anisotropic velocity dispersions which are needed to support a triaxial equilibrium shape (Binney 1978a, b; Illingworth 1981).

Few models satisfy these requirements. To date, all of them are numerical and have been constructed either by linear programming techniques (Schwarzschild 1979, 1982) or by brute force N-body calculations (e.g. Wilkinson & James 1982; van Albada 1982). No simple expressions are known for the two non-classical integrals of motion enjoyed by most of the stars in these models. As a result the phase-space distribution function, which is a function of all three isolating integrals (Jeans 1915; Lynden-Bell 1962b), is known only as a set of occupation numbers of individual orbits.

This paper is the first in a series in which we try to improve upon this situation. We consider inhomogeneous triaxial mass models in which all stellar orbits have three exact isolating integrals of motion, for arbitrary ratios of the axes of the model. The integrals are known explicitly and the orbits can therefore be described by analytic means.

The existence of these mass models is based on the existence of the special potentials for which the Hamilton–Jacobi equation is separable, and therefore admit three independent isolating integrals. Liouville (1846), Bertrand (1852) and Jacobi (1866) already discuss such potentials. They were first systematically studied by Stäckel (1890, 1891, 1893), Levi Civita (1904) and Dall'Acqua (1908). Independently, Eddington (1915a) introduced them in stellar dynamics. Later investigations were made by Weinacht (1924), Clark (1936) and Lynden-Bell (1962c). For all these potentials the Hamilton–Jacobi equation separates in ellipsoidal coordinates, or their degenerate forms. We shall refer to them as *Stäckel potentials*.

The orbits in a Stäckel potential can be found by straightforward integration of the Hamilton–Jacobi equation. However, a full classification of orbits can be made without such an integration. The fact that the motion is separable means that an individual orbit can be considered as the sum of three motions, one in each coordinate. The stars are thus constrained – by the integrals of motion – to *move between coordinate surfaces*. As a result, all possible orbital shapes can be found by a simple inspection of the coordinate system in which the Hamilton–Jacobi equation separates.

Another useful property of orbits in a separable potential is that their individual density distribution is known explicitly and moreover is easily evaluated. This makes it straightforward to construct self-consistent models by means of, e.g. Schwarzschild's (1979) method, in which a mass model is reconstructed from the densities of individual orbits in it by linear programming, while avoiding laborious numerical integrations (Schwarzschild 1979, 1982; Richstone 1980).

In the present paper we study the stellar orbits in a particular mass model with a gravitational potential that is of Stäckel form. It is the triaxial generalization of an oblate spheroidal model discovered by Kuzmin (1953, 1956) in his classic study of separable models of the Galaxy. The present model is the only inhomogeneous triaxial body with a potential of Stäckel form in which the density is stratified exactly on similar, concentric aligned ellipsoids and is nowhere singular (de Zeeuw & Lynden-Bell 1985). We shall call it the *perfect ellipsoid*.

It will turn out that the orbital structure in the perfect ellipsoid is *generic* for all triaxial mass models that are centrally concentrated, have a finite central density, and a Stäckel potential. Furthermore, the general orbits in these separable models correspond precisely to the four major families of orbits that occur in Schwarzschild's (1979) non-rotating elliptical galaxy model (the Schwarzschild ellipsoid). These are just the orbit families that are of most importance for determining the structure of triaxial galaxies (Schwarzschild 1981).

In Section 2 we briefly discuss the ellipsoidal coordinates in which the Hamilton–Jacobi equation is separable. In Section 3 we present the perfect ellipsoid and show that its gravitational potential is of Stäckel form. The classification of orbital shapes in Stäckel potentials is

discussed in Section 4 and applied to the perfect ellipsoid in Section 5. The degeneracies that occur for special values of the axis ratios of the perfect ellipsoid are treated in Section 6. Individual orbit densities are considered in Section 7. In Section 8 we introduce action-angle variables, and we show how the orbital frequencies can be computed. The orbit classification in terms of the action integrals is presented in Section 9. The results are discussed in Section 10.

2 Coordinates

Ellipsoidal coordinates were introduced in mathematical physics by Lamé (1837) and Jacobi (1839). Numerous authors have discussed their properties (e.g. Jacobi 1866; Whittaker & Watson 1902; Morse & Feshbach 1953; Lyttleton 1953). In this section we consider the shapes of the coordinate surfaces, which are the surfaces bounding the orbits in Stäckel potentials. We first discuss elliptic coordinates in a plane.

2.1 ELLIPTIC COORDINATES

Let (x, y) be Cartesian coordinates in a plane. Following the notation of Lynden-Bell (1962c) we define elliptic coordinates (λ, μ) as the roots for τ of

$$\frac{x^2}{\tau+\alpha}+\frac{y^2}{\tau+\beta}=1, \tag{1}$$

where α and β are constants; we assume $\alpha<\beta$, and we take $\mu<\lambda$. The following inequality holds

$$-\beta\leq\mu\leq-\alpha\leq\lambda. \tag{2}$$

Expressions for x and y in terms of λ and μ are

$$x^2=\frac{(\lambda+\alpha)(\mu+\alpha)}{(\alpha-\beta)}, \qquad y^2=\frac{(\lambda+\beta)(\mu+\beta)}{(\beta-\alpha)}, \tag{3}$$

from which we find

$$\lambda+\mu=-\alpha-\beta+x^2+y^2, \qquad \lambda\mu=\alpha\beta-\beta x^2-\alpha y^2. \tag{4}$$

Fig. 1 shows the coordinate lines. Curves of constant λ are ellipses with the major axis in the y-direction. They all have identical foci at $x=0$, $y=\pm\sqrt{\beta-\alpha}$. The ellipse $\lambda=-\alpha$ is the segment of the y-axis between the foci. Curves of constant μ are hyperbolae, with the same foci. For $\mu=-\beta$ they coincide with the x-axis; $\mu=-\alpha$ corresponds to the parts of the y-axis outside the foci.

Through each point (x, y) there is one ellipse and one hyperbola of the confocal family, and these two curves are perpendicular to each other in this point. The line element $ds^2=dx^2+dy^2$ of

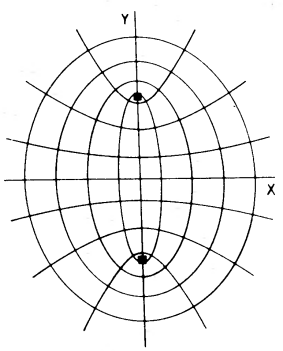

Figure 1. Elliptic coordinates in a plane. The filled squares are the foci.

these curvilinear orthogonal coordinates is equal to $P^2d\lambda^2+Q^2d\mu^2$, with metric coefficients P and Q given by

$$P^2=\frac{\lambda-\mu}{4(\lambda+\alpha)(\lambda+\beta)}, \qquad Q^2=\frac{\mu-\lambda}{4(\mu+\alpha)(\mu+\beta)}. \tag{5}$$

Near the origin the elliptic coordinates are approximately Cartesian. At large distances from the origin the ellipses become progressively rounder ($\lambda\rightarrow\infty$) and the hyperbolae are nearly identical to their asymptotes, which are straight lines through the origin. Thus, very far from the origin, the elliptic coordinates resemble ordinary polar coordinates. The asymptotic relations are given in Appendix A.

The transformation $(x, y)\rightarrow(\lambda, \mu)$ is unique. However, a choice of values for λ and μ only determines x^2 and y^2, so in general corresponds to four points $(\pm x, \pm y)$.

2.2 ELLIPSOIDAL COORDINATES

Let (x, y, z) be Cartesian coordinates. We define ellipsoidal coordinates (λ, μ, ν) as the three roots for τ of

$$\frac{x^2}{\tau+\alpha}+\frac{y^2}{\tau+\beta}+\frac{z^2}{\tau+\gamma}=1, \tag{6}$$

where α, β and γ are constants with $\alpha<\beta<\gamma$, and we take $\nu<\mu<\lambda$. The three roots satisfy the inequality

$$-\gamma\leq\nu\leq-\beta\leq\mu\leq-\alpha\leq\lambda. \tag{7}$$

The relations between (x, y, z) and (λ, μ, ν) are

$$x^2=\frac{(\lambda+\alpha)(\mu+\alpha)(\nu+\alpha)}{(\alpha-\beta)(\alpha-\gamma)},$$

$$y^2=\frac{(\lambda+\beta)(\mu+\beta)(\nu+\beta)}{(\beta-\alpha)(\beta-\gamma)},$$

$$z^2=\frac{(\lambda+\gamma)(\mu+\gamma)(\nu+\gamma)}{(\gamma-\alpha)(\gamma-\beta)}, \tag{8}$$

and

$$\lambda+\mu+\nu=-\alpha-\beta-\gamma+x^2+y^2+z^2,$$

$$\lambda\mu+\mu\nu+\nu\lambda=\alpha\beta+\beta\gamma+\gamma\alpha-(\beta+\gamma)x^2-(\gamma+\alpha)y^2-(\alpha+\beta)z^2,$$

$$\lambda\mu\nu=-\alpha\beta\gamma+\beta\gamma x^2+\gamma\alpha y^2+\alpha\beta z^2. \tag{9}$$

By equation (7), λ, μ and ν cover adjacent intervals of one variable which we shall later call τ. We shall describe the coordinate surfaces by covering this variable from high to low values.

Surfaces of constant λ are *ellipsoids*. For very large λ they are nearly spherical with radius $\sqrt{\lambda+\alpha}$. As λ diminishes the ellipsoids shrink and become more pronouncedly triaxial with the long axis in the z-direction and the short axis in the x-direction. This continues until at $\lambda=-\alpha$ the short axis has become zero and the ellipsoid degenerates into the area inside the *focal ellipse* $y^2/(\beta-\alpha)+z^2/(\gamma-\alpha)=1$. Fig. 2a shows the surfaces of constant λ. For cross-reference to the other figures the points $z=\pm\sqrt{\gamma-\alpha}$ at which the focal ellipse intersects the z-axis are marked by

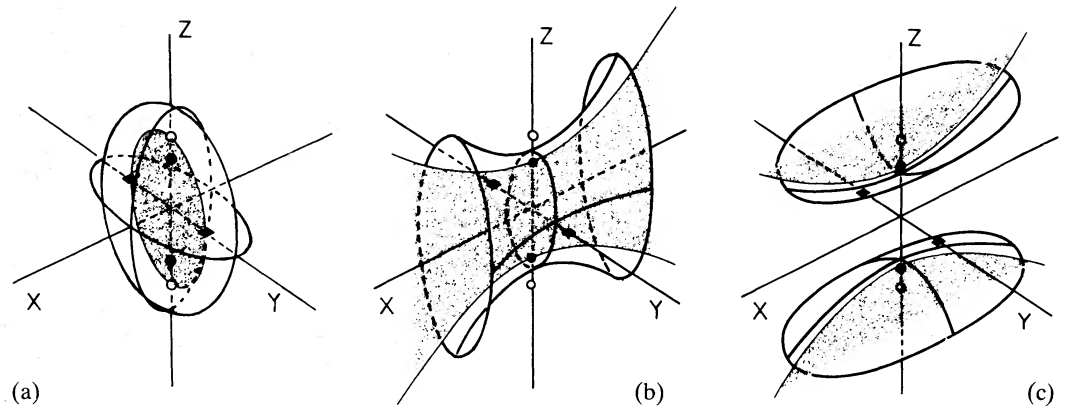

Figure 2. Ellipsoidal coordinates. The three pairs of foci are denoted by the open and filled circles and the filled squares. (a) Surfaces of constant λ are ellipsoids. The degenerate ellipsoid $\lambda=-\alpha$, inside the focal ellipse, is shaded. (b) Surfaces of constant μ are hyperboloids of one sheet. The degenerate hyperboloid $\mu=-\beta$, between the two branches of the focal hyperbola, is shaded. (c) Surfaces of constant ν are hyperboloids of two sheets. The degenerate hyperboloid $\nu=-\beta$ is shaded.

open circles and the points $y=\pm\sqrt{\beta-\alpha}$ at which it intersects the y-axis by squares. The foci of the focal ellipse are at $z=\pm\sqrt{\gamma-\beta}$ and are marked by filled circles.

The surface $\mu=-\alpha$ is the part of the plane $x=0$ outside the focal ellipse. All surfaces of constant μ are *hyperboloids of one sheet* around the x-axis (Fig 2b). With decreasing μ the ellipse by which this hyperboloid cuts the $x=0$ plane shrinks and finally, at $\mu=-\beta$, coincides with the piece of the z-axis between the foci at $z=\pm\sqrt{\gamma-\beta}$. At the same time the entire hyperboloid degenerates into the part of the plane $y=0$ between the two branches of the *focal hyperbola* $x^2/(\alpha-\beta)+z^2/(\gamma-\beta)=1$. This hyperbola intersects the z-axis at the filled circles and has the open circles as its foci.

The surface $\nu=-\beta$ is confined to the plane $y=0$ but covers the parts outside that covered by $\mu=-\beta$. With falling ν these parts open up into *hyperboloids of two sheets* around the z-axis. They gradually widen and approach the $z=0$ plane. At $\nu=-\gamma$ they coincide with this plane (Fig. 2c).

Through each point (x, y, z) there is one ellipsoid λ, one hyperboloid of one sheet μ and one hyperboloid of two sheets ν. These three surfaces are perpendicular to each other in this point. The line element $ds^2=dx^2+dy^2+dz^2$ of the coordinates is equal to $P^2d\lambda^2+Q^2d\mu^2+R^2d\nu^2$, where the metric coefficients are given by

$$P^2=\frac{(\lambda-\mu)(\lambda-\nu)}{4(\lambda+\alpha)(\lambda+\beta)(\lambda+\gamma)},\quad Q^2=\frac{(\mu-\nu)(\mu-\lambda)}{4(\mu+\alpha)(\mu+\beta)(\mu+\gamma)},\quad R^2=\frac{(\nu-\lambda)(\nu-\mu)}{4(\nu+\alpha)(\nu+\beta)(\nu+\gamma)}. \tag{10}$$

Near the origin the coordinates (λ, μ, ν) are approximately Cartesian. At large distances from the centre the ellipsoids become -- as we have seen – progressively more nearly spherical and the hyperboloids are almost indistinguishable from their asymptotic surfaces which are cones around the x-axis (μ) and around the z-axis (ν). The asymptotic relations are given in Appendix A.

Table 1. Elliptic coordinates in each of the principal planes.

Plane		Foci	Labels of coordinate curves		
			Plane	Ellipses	Hyperbolae
$x=0$,	central part	$z=\pm\sqrt{\gamma-\beta}$	$\lambda=-\alpha$	μ	ν
	outer part		$\mu=-\alpha$	λ	ν
$y=0$,	central part	$z=\pm\sqrt{\gamma-\alpha}$	$\mu=-\beta$	λ	ν
	outer part		$\nu=-\beta$	λ	μ
$z=0$,	entire plane	$y=\pm\sqrt{\beta-\alpha}$	$\nu=-\gamma$	λ	μ

In each of the three principal planes the coordinates form an elliptic coordinate system as described in Section 2.1. The complete set of specifications for the three planes is given in Table 1, in agreement with Fig. 2.

Finally, we remark that the transformation from (x, y, z) to (λ, μ, ν) is unique. The converse is not true. Each choice (λ, μ, ν) corresponds in general to eight different points $(\pm x, \pm y, \pm z)$.

2.3 SPECIAL CASES

If two or three of the constants α, β and γ in equation (6) are equal, the ellipsoidal coordinates take special forms. We briefly describe these degeneracies. For further details, see, e.g. Morse & Feshbach (1953).

For $\gamma=\beta$ the coordinates (λ, μ, ν) are *oblate spheroidal coordinates* (λ, μ, χ). Surfaces of constant λ are oblate spheroids with the short axis in the x-direction. Surfaces of constant μ are hyperboloids of revolution around the x-axis. The range of ν is zero, so that it can no longer be used as a coordinate. The surfaces of constant ν of the general case, hyperboloids of two sheets around the z-axis, are now planes containing the x-axis. Thus, they can be labelled by an azimuthal angle χ.

In each plane of constant χ (*meridional plane*) the coordinates (λ, μ) are elliptic coordinates. They are the roots for τ of

$$\frac{x^2}{\tau+\alpha}+\frac{\tilde{z}^2}{\tau+\beta}=1, \qquad \tilde{z}^2=y^2+z^2, \tag{11}$$

where $-\beta\leq\mu\leq-\alpha\leq\lambda$. The foci are at $x=0$, $\tilde{z}=\pm\sqrt{\beta-\alpha}$. The relations between (λ, μ) and $(x, \tilde{z})$ can be deduced easily from equations (3) and (4). In the equatorial plane, $x=0$, the coordinates are polar coordinates $(\tilde{z}, \chi)$ with $\tilde{z}^2=\tau+\beta$ ($\tau=\lambda$ or μ). Note that the circles are labelled by μ for radii $\tilde{z}\leq\sqrt{\beta-\alpha}$ and by λ for $\tilde{z}\geq\sqrt{\beta-\alpha}$. The focal ellipse $\lambda=\mu=-\alpha$ in the (y, z)-plane of the general case now is a *focal circle* with radius $\tilde{z}=\sqrt{\beta-\alpha}$. The coordinate lines in the meridional and equatorial planes are shown in Fig. 20. The line element ds^2 is equal to $P^2d\lambda^2+Q^2d\mu^2+\tilde{z}^2d\chi^2$, with P and Q given in equation (5).

For $\beta=\alpha$, the coordinates (λ, μ, ν) are *prolate spheroidal coordinates* (λ, ϕ, ν). Surfaces of constant λ now are prolate spheroids elongated along the z-axis. Surfaces of constant ν are two sheeted hyperboloids of revolution around the z-axis. The variable μ is equal to $-\beta=-\alpha$ and can no longer be used as a coordinate. The surfaces of constant μ of the general case (hyperboloids of one sheet) are planes that contain the z-axis. They are labelled by an azimuthal angle ϕ.

In each meridional plane (ϕ=constant) the variables (λ, ν) are elliptic coordinates. They are the roots for τ of

$$\frac{\varpi^2}{\tau+\alpha}+\frac{z^2}{\tau+\gamma}=1, \qquad \varpi^2=x^2+y^2, \tag{12}$$

with $-\gamma\leq\nu\leq-\alpha\leq\lambda$. The foci are at $\varpi=0$, $z=\pm\sqrt{\gamma-\alpha}$. The relations between (λ, ν) and (ϖ, z) are similar to those given in equations (3) and (4). In the equatorial plane the coordinates are polar coordinates (ϖ, ϕ) with $\varpi^2=\lambda+\alpha$. The coordinate lines in the meridional and equatorial planes are shown in Fig. 24. The line element of the prolate spheroidal coordinates is equal to $P^2d\lambda^2+\varpi^2d\phi^2+R^2d\nu^2$, where P and Q are expressions in λ and ν similar to those given in equation (5).

For $\gamma=\beta=\alpha$ all three pairs of foci of the ellipsoidal coordinates coincide with the origin and the variables μ and ν lose their meaning. The ellipsoidal coordinates become *spherical coordinates* (r, θ, ϕ) defined by $x=r\sin\theta\cos\phi$, $y=r\sin\theta\sin\phi$ and $z=r\cos\theta$, where $r^2=\lambda+\alpha$.

3 The perfect ellipsoid

3.1 DENSITY DISTRIBUTION

The density distribution of the perfect ellipsoid is given by

$$\varrho=\frac{\varrho_0}{(1+\tilde{m}^2)^2}, \tag{13}$$

where

$$\tilde{m}^2=\frac{x^2}{a^2}+\frac{y^2}{b^2}+\frac{z^2}{c^2}, \qquad a\geq b\geq c\geq 0. \tag{14}$$

The density is stratified on similar concentric ellipsoids with semiaxes $\tilde{m}a$, $\tilde{m}b$ and $\tilde{m}c$. The x-axis is the long axis of the density distribution and the z-axis is the short axis. The central density is ϱ_0. At large distances from the centre ϱ falls off as $\tilde{m}^{-4}$.

The mass $M(\tilde{m})$ within ellipsoidal radius $\tilde{m}$ is

$$M(\tilde{m})=2\pi abc\varrho_0\left\{\arctan\tilde{m}-\frac{\tilde{m}}{1+\tilde{m}^2}\right\}. \tag{15}$$

The total mass M is

$$M=\pi^2 abc\varrho_0, \tag{16}$$

and the half-mass radius $\tilde{m}_{1/2}$ is equal to 2.264437 ....

3.2 DERIVATION OF THE GRAVITATIONAL POTENTIAL

The calculation of the gravitational potential of an ellipsoidally stratified density distribution is classical theory. Using Theorem 12 from Chapter 3 of Chandrasekhar (1969) we find that the potential V of the perfect ellipsoid is given by

$$V=-\pi G\varrho_0 abc\int_0^\infty \frac{1}{[1+x^2/(a^2+u)+y^2/(b^2+u)+z^2/(c^2+u)]}\times\frac{du}{\sqrt{(a^2+u)(b^2+u)(c^2+u)}}, \tag{17}$$

where G is the gravitational constant. Define ellipsoidal coordinates (λ,μ,ν) by choosing in (6)

$$\alpha=-a^2, \qquad \beta=-b^2, \qquad \gamma=-c^2. \tag{18}$$

Straightforward algebra then reduces equation (17) upon substitution of equations (8), and (18) to

$$V=-\pi G\varrho_0 abc\int_0^\infty \frac{\sqrt{(u-\alpha)(u-\beta)(u-\gamma)}}{(u+\lambda)(u+\mu)(u+\nu)}du, \tag{19}$$

which can be separated as

$$V=-\frac{F(\lambda)}{(\lambda-\mu)(\lambda-\nu)}-\frac{F(\mu)}{(\mu-\nu)(\mu-\lambda)}-\frac{F(\nu)}{(\nu-\lambda)(\nu-\mu)}, \tag{20}$$

where

$$F(\tau)=\pi G\varrho_0 abc\int_0^\infty\left[\frac{\sqrt{(u-\alpha)(u-\beta)(u-\gamma)}}{(u+\tau)}+A(u)\tau+B(u)\right]du. \tag{21}$$

Here τ denotes λ, μ or ν. The functions $A(u)$ and $B(u)$ serve to assure the convergence of the integral defining $F(\tau)$ but are otherwise arbitrary. We may use this freedom to give $F(\tau)$ a simple form. The function

$$F(\tau)=(\tau+\alpha)(\tau+\gamma)\,G(\tau), \tag{22}$$

with

$$G(\tau)=\pi G\varrho_0 abc\int_0^\infty \frac{\sqrt{u-\beta}}{\sqrt{(u-\alpha)(u-\gamma)}}\cdot\frac{du}{u+\tau}, \tag{23}$$

is of the form (21) because

$$\frac{(\tau+\alpha)(\tau+\gamma)}{u+\tau}=\frac{(u-\alpha)(u-\gamma)}{u+\tau}+\tau-u+\alpha+\gamma.$$

This is the form we adopt for $F(\tau)$ in equation (20) in the subsequent analysis. The function $G(\tau)$ can be expressed in terms of the incomplete elliptic integrals of the three kinds and is readily evaluated numerically. It is further discussed in Appendix B.

The potential (20) is of Stäckel form (Weinacht 1924), i.e. *the potential of the perfect ellipsoid has the special form for which the equations of motion are separable in the ellipsoidal coordinates* (λ,μ,ν) *that are defined by equations (6) and (18)*. This is true for all value of the axis ratios of the perfect ellipsoid. de Zeeuw & Lynden-Bell (1985) show that the perfect ellipsoid is the only mass model with a Stäckel potential in which $\varrho=\varrho(\tilde{m}^2)$, i.e. in which the density is stratified *exactly* on similar, concentric and aligned ellipsoids, and is nowhere singular. However, many other triaxial mass models with a Stäckel potential exist (de Zeeuw 1985b).

3.3 A SPECIFIC EXAMPLE

All results in the previous sections are valid irrespective of the axis ratios $a:b:c$ of the perfect ellipsoid. It is useful to have an explicit example. For this we take $a=1$, $b=5/8$ and $c=1/2$. The resulting axis ratios are identical to those of the Schwarzschild ellipsoid, although the radial density profile of the latter ellipsoid differs from (13). In order to facilitate a comparison, all figures in the present paper relating to the perfect ellipsoid have been made for these values of a, b and c.

Numerical values of $G(\tau)/GM$ and its derivative $G'(\tau)/GM$ are given in Table 2 for a number of values of ϱ. Both these functions will be used in the orbit analysis. A graph of $G(\tau)/GM$ is shown in Fig. 3. $G(\tau)$ decreases monotonically with increasing τ; It follows from equation (B8) that $G(\tau)\sim GM/\sqrt{\tau}$ at large τ. For other values of the axis ratios $G(\tau)$ has a similar form.

Fig. 4a shows the equipotential curves V equals constant in the (x, y)-plane of the perfect ellipsoid [*cf.* equation (74)]. Since the total mass of the perfect ellipsoid is finite, the potential becomes Keplerian at large distances from the centre and the equipotential curves become rapidly nearly round. This is illustrated for each of the principal planes in Fig. 4b which shows the axis ratios of the equipotential curves as a function of potential energy. The potential equals $-G(-\beta)$ in the centre and approaches zero at large distances. Fig. 4b may be compared with a similar one for the Schwarzschild ellipsoid, fig. 1 in Merritt (1980).

The surfaces of constant density, $\tilde{m}^2$=constant, and the equipotential surfaces both have their long axis in the x-direction and their short axis in the z-direction. At a given radius the equipotential surface is rounder than the equidensity surface. Note that the coordinate surfaces λ=constant are elongated in the opposite manner: they have the z-axis as long axis and the x-axis as short axis.

Table 2. The functions $G(\tau)/GM$ and $G'(\tau)/GM$ for $a=1$, $b=5/8$ and $c=1/2$.

τ	$G(\tau)/GM$	$G'(\tau)/GM$
$\nu-\gamma=0.25$	1.037189	−1.203732
0.30	0.983059	−0.976006
0.35	0.938470	−0.816198
$\mu-\beta=0.390625$	0.907390	−0.717962
0.4	0.900746	−0.698282
0.5	0.839635	−0.536714
0.6	0.791545	−0.431889
0.7	0.752211	−0.358818
0.8	0.719138	−0.305222
0.9	0.690744	−0.264382
$\lambda-\alpha=1.0$	0.665970	−0.232328
1.2	0.624503	−0.185454
1.5	0.576185	−0.140344
2	0.517851	−0.097522
3	0.443134	−0.057868
5	0.361114	−0.029561
7	0.314090	−0.018838
10	0.269910	−0.011607
15	0.226234	−0.006643
20	0.199116	−0.004451
30	0.165816	−0.002517
50	0.131092	−0.001217

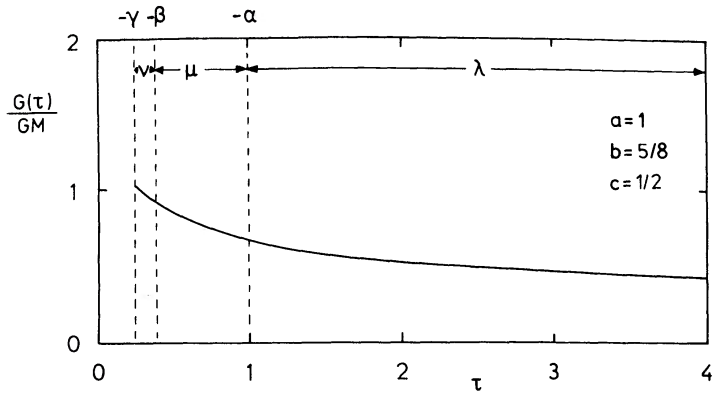

Figure 3. The function $G(\tau)$ for $a=1$, $b=5/8$ and $c=1/2$.

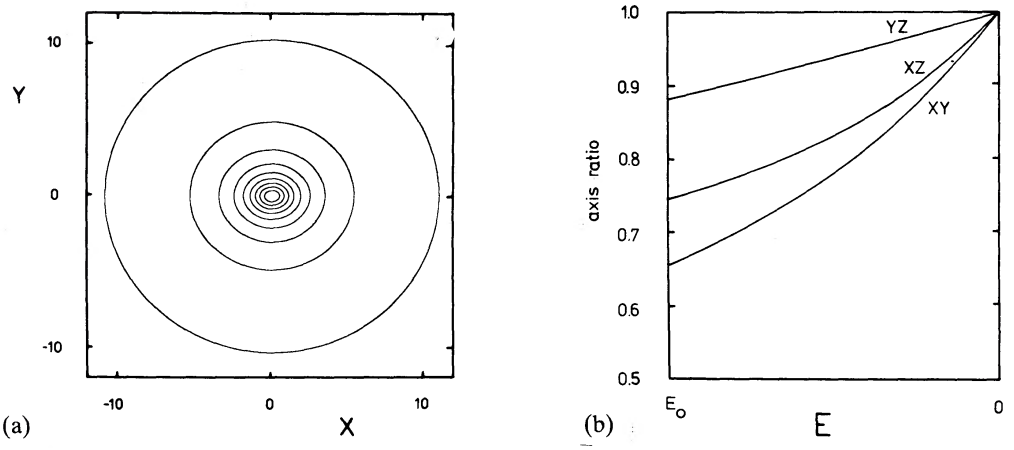

Figure 4. (a) Equipotential curves in the (x, y)-plane of the perfect ellipsoid. Contours are shown for $E/V(0, 0, 0)=0.9, \ldots, 0.1$, in intervals of 0.1. (b) Axis ratios of the equipotential curves in all three principal planes as function of the value of the potential energy.

3.4 SPECIAL CASES

Special values of the axis ratios of the perfect ellipsoid lead to simpler expressions for the gravitational potential, and also – as we shall see in Section 6 – to a simpler orbital structure. We consider briefly the prolate, oblate and spherical models, and also the elliptic and circular disc, and the needle. The reader who is not interested in these degeneracies should turn his attention to Section 4.

3.4.1 Prolate spheroid

For $a>b=c$ the mass model defined in (13) is a prolate spheroid with the x-axis as symmetry axis. From equation (18) it follows that $\gamma=\beta$. The ellipsoidal coordinates (λ, μ, ν) reduce to *oblate spheroidal coordinates* (λ, μ, χ) (*cf.* Section 2.3). The gravitational potential of this perfect prolate spheroid follows from equations (20), (22) and (23) upon substitution of $\nu=-\gamma=-\beta$. The result is

$$V=V(\lambda, \mu)=-\frac{(\lambda+\alpha)\,G(\lambda)-(\mu+\alpha)\,G(\mu)}{\lambda-\mu}. \tag{24}$$

which is manifestly axisymmetric, and of two-dimensional Stäckel form (e.g. Jacobi 1866). The integral (23) for $G(\tau)$ is now elementary. We find

$$G(\mu)=2\pi G\varrho_0 b^2\sqrt{\frac{\alpha}{\mu+\alpha}}\ \operatorname{artanh}\ \sqrt{\frac{\mu+\alpha}{\alpha}},$$

$$G(\lambda)=2\pi G\varrho_0 b^2\sqrt{\frac{-\alpha}{\lambda+\alpha}}\ \arctan\sqrt{\frac{\lambda+\alpha}{-\alpha}}, \tag{25}$$

with $\alpha=-a^2$. This function is regular and smooth. Some special values of $G(\tau)$ and its derivative $G'(\tau)$ are given in Appendix B.

3.4.2 Oblate spheroid

For $a=b>c$ the mass model defined in (13) is an oblate spheroid with the z-axis as symmetry axis. It follows from equation (18) that $\alpha=\beta$ in this case. The coordinates (λ, μ, ν) are *prolate spheroidal coordinates* (λ, ϕ, ν) (*cf.* Section 2.3). The gravitational potential V of this perfect oblate spheroid follows from (20), (22) and (23) upon substitution of $\mu=-\beta=-\alpha$. The result is

$$V=V(\lambda, \nu)=-\frac{(\lambda+\gamma)\,G(\lambda)-(\nu+\gamma)\,G(\nu)}{\lambda-\nu}, \tag{26}$$

which is axisymmetric, as it should be, and of two-dimensional Stäckel form. The integral (23) for $G(\tau)$ is elementary. We find

$$G(\tau)=2\pi G\varrho_0 a^2\sqrt{\frac{-\gamma}{\tau+\gamma}}\ \arctan\sqrt{\frac{\tau+\gamma}{-\gamma}}, \qquad \tau=\lambda \quad \text{or} \quad \nu, \tag{27}$$

with $\gamma=-c^2$. Some special values of $G(\tau)$ and its derivative $G'(\tau)$ are given in Appendix B. The separability of the gravitational potential for this case was first demonstrated by Kuzmin (1953, 1956).

3.4.3 Sphere

For $a=b=c$ the mass model defined in (13) is a sphere. It follows from equation (18) that the ellipsoidal coordinates reduce to spherical coordinates (r, θ, ϕ) (*cf.* Section 2.3). The gravitational potential of the 'perfect sphere' follows from the general expressions (20), (22) and (23) upon substitution of $\mu=\nu=-\gamma=-\beta=-\alpha=a^2$. The result is

$$V=V(\lambda)=-G(\lambda)=-2\pi G\varrho_0 a^2\,\frac{\arctan(r/a)}{(r/a)}, \qquad r=\sqrt{\lambda+\alpha}. \tag{28}$$

3.4.4 Elliptic disc

For $a>b>c=0$ the mass model defined in (13) is an infinitesimally thin elliptic disc in the (x, y)-plane. In order to derive the surface density distribution of the perfect elliptic disc we take in (13) the limit $c\to 0$, while keeping $\Sigma_0=\pi\varrho_0 c/2$ fixed. Then the density becomes $\varrho(x, y, z)=\Sigma(x, y)\delta(z)$, where δ is the Dirac delta function and Σ is the surface density given by

$$\Sigma=\frac{\Sigma_0}{(1+\tilde{m}^2)^{3/2}}, \qquad \tilde{m}^2=\frac{x^2}{a^2}+\frac{y^2}{b^2}. \tag{29}$$

Σ is stratified on similar ellipses with semiaxes $\tilde{m}a$ and $\tilde{m}b$. The central surface density is Σ_0. At large distances from the centre Σ falls off as $\tilde{m}^{-3}$. The total mass within elliptic radius $\tilde{m}$ is

$$M(\tilde{m})=2\pi\Sigma_0 ab\left\{1-\frac{1}{(1+\tilde{m}^2)^{1/2}}\right\}. \tag{30}$$

The total mass M of the disc is equal to $2\pi\Sigma_0 ab$. The half mass radius $\tilde{m}_{1/2}$ equals $\sqrt{3}$.

For $c=0$ we find from (18) that $\gamma=0$. The coordinates (λ, μ, ν) are therefore still ellipsoidal coordinates. The gravitational potential of the perfect elliptic disc is given by the expressions (20), (22) and (23). For $\gamma=0$ the integral $G(\tau)$ can be expressed in terms of the complete elliptic integrals of the three kinds. It is readily evaluated numerically. Properties of $G(\tau)$ are given in Appendix B.

Fig. 5 is a graph of $G(\tau)/GM$ for $a=1$, $b=1/2$ and $c=0$. At small τ the function $G(\tau)$ diverges as $bGM/a\sqrt{\tau}$. At large τ it falls off as $GM/\sqrt{\tau}$. Fig. 6 shows equipotential curves in two of the principal planes. In the disc the potential is smooth, and the equipotential curves quickly become nearly round with increasing radius, in agreement with the finite total mass of the disc. In the z-direction the potential is continuous, but not differentiable at $z=0$. This is due to the presence of the thin disc in the plane $z=0$.

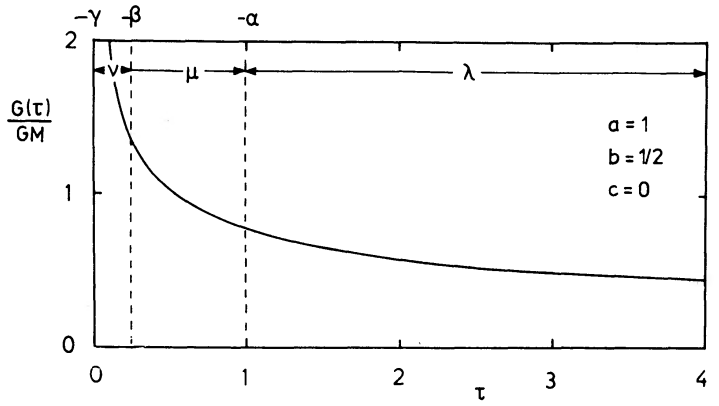

Figure 5. The function $G(\tau)$ for $a=1$, $b=1/2$ and $c=0$.

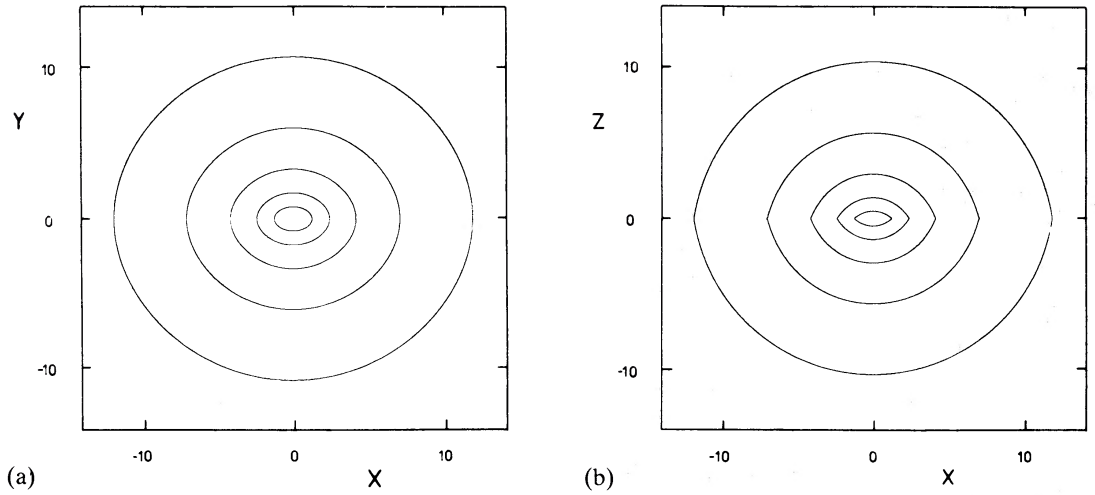

Figure 6. Equipotential curves in two principal planes for the perfect elliptic disc, for $a=1$, $b=1/2$ and $c=0$. (a) (x, y)-plane; (b) (x, z)-plane.

3.4.5 Kuzmin's disc

For $a=b>c=0$ the elliptic disc (29) is axisymmetric. Its surface density can be written as

$$\Sigma=\frac{a^3\Sigma_0}{(\varpi^2+a^2)^{3/2}}, \qquad \varpi^2+x^2+y^2. \tag{31}$$

This is Kuzmin's disc, which sometimes is referred to as *Toomre disc I*. It has been the subject of a number of investigations (e.g. Kuzmin 1953; Toomre 1963; Shu 1969; Miyamoto 1971, 1974; Kalnajs 1976).

From equation (18) it follows that $\beta=\alpha$ and $\gamma=0$. As a result, the coordinates (λ, μ, ν) are prolate spheroidal coordinates (λ, ϕ, ν). This is not surprising, since we can obtain the disc (31) also by collapsing the perfect oblate spheroid along its short axis. We note that the relation between the (λ, ν) and the (ϖ, z) coordinates is given by

$$\varpi^2=\frac{(\lambda+\alpha)(\nu+\alpha)}{\alpha}, \qquad z^2=\frac{\lambda\nu}{-\alpha}, \tag{32}$$

so that $\varpi^2+z^2=\lambda+\nu+\alpha$. The foci of the elliptic coordinates (λ, ν) lie on the z-axis, at $z=\pm\sqrt{-\alpha}=\pm a$.

The gravitational potential of Kuzmin's disc follows from (26) upon taking $\gamma=0$:

$$V=V(\lambda, \nu)=-\frac{\lambda G(\lambda)-\nu G(\nu)}{\lambda-\nu}. \tag{33}$$

The function $G(\tau)$ is now elementary and simple

$$G(\tau)=\frac{GM}{\sqrt{\tau}}, \tag{34}$$

where we have written $M=2\pi\Sigma_0 a^2$, the total mass of the disc.

Substitution of (34) in (33) and transformation to the variables (ϖ, z) by means of (32) produces

$$V=-\frac{GM}{[\varpi^2+(|z|+a)^2]^{1/2}}. \tag{35}$$

This is identical to the result obtained by Toomre (1963) by means of the Fourier–Bessel Theorem. In the disc the potential is simply

$$V=V(\lambda, 0)=-\frac{GM}{\sqrt{\lambda}}=-\frac{GM}{(\varpi^2+a^2)^{1/2}}. \tag{36}$$

As already noted by Kuzmin (1953), it follows from (35) that the potential *above* the disc equals that of a point mass M in the focus at $z=-a$ *below* the disc. The potential *below* the disc is that of a point mass M in the focus at $z=+a$ *above* the disc (see also Hunter 1980). Thus, equipotential surfaces outside the disc are parts of spheres, centred on the appropriate focus.

3.4.6 Needle

For completeness, we briefly consider the case $a>b=c=0$ for which the density (13) is an infinitesimally thin needle along the x-axis. The line density distribution of this needle (or perfect cigar) can be obtained from (13) by taking the limit $b=c\rightarrow 0$, while keeping $\zeta_0=2\Sigma_0 b=\pi\varrho_0 b^2$ constant. Then the density becomes $\varrho(x, y, z)=\zeta(x)\delta(y)\delta(z)$, where ζ is the line density given by

$$\zeta=\frac{\zeta_0}{1+\tilde{m}^2}, \qquad \tilde{m}^2=\frac{x^2}{a^2}. \tag{37}$$

The central line density is ζ_0. At large distances ζ falls off as $1/\tilde{m}^2$. The mass $M(\tilde{m})$ between $-\tilde{m}$ and $\tilde{m}$ is

$$M(\tilde{m})=2a\zeta_0 \arctan \tilde{m}, \tag{38}$$

so that the total mass M of the needle is $\pi a\zeta_0$. The half mass distance is equal to 1.

From equation (18) it follows that $\beta=\gamma=0$. The coordinates (λ, μ, ν) are now oblate spheroidal coordinates (λ, μ, χ), in agreement with the fact that the needle (37) may be obtained by collapsing the perfect prolate spheroid along its short axes. The gravitational potential of the needle follows from (24) and (25) upon substitution of ζ_0 for $\pi\varrho_0 b^2$ in those expressions.

4 Stellar orbits in Stäckel potentials

4.1 EQUATIONS OF MOTION

The Hamiltonian H for motion in a potential $V(\lambda, \mu, \nu)$ is

$$H=\frac{p_\lambda^2}{2P^2}+\frac{p_\mu^2}{2Q^2}+\frac{p_\nu^2}{2R^2}+V(\lambda,\mu,\nu), \tag{39}$$

where $p_\lambda=P^2\dot{\lambda}$, $p_\mu=Q^2\dot{\mu}$ and $p_\nu=R^2\dot{\nu}$ are the momenta conjugate to λ, μ and ν. P, Q and R are given in equation (10). When we substitute $p_\tau=\partial W/\partial\tau$, with $\tau=\lambda, \mu$ or ν, in (39) and equate the resulting expression to the total energy E, we obtain the Hamilton–Jacobi equation. For a potential of Stäckel form (20) we find, after multiplication by $(\lambda-\mu)(\mu-\nu)(\nu-\lambda)$,

$$\begin{aligned}&(\nu-\mu)\left\{2(\lambda+\alpha)(\lambda+\beta)(\lambda+\gamma)\left(\frac{\partial W}{\partial\lambda}\right)^2-F(\lambda)-\lambda^2E\right\}\\&+(\lambda-\nu)\left\{2(\mu+\alpha)(\mu+\beta)(\mu+\gamma)\left(\frac{\partial W}{\partial\mu}\right)^2-F(\mu)-\mu^2E\right\}\\&+(\mu-\lambda)\left\{2(\nu+\alpha)(\nu+\beta)(\nu+\gamma)\left(\frac{\partial W}{\partial\nu}\right)^2-F(\nu)-\nu^2E\right\}=0.\end{aligned} \tag{40}$$

The solution W of this partial differential equation is Hamilton's characteristic function.

Since we already know that the motion is separable, due to the special form (20) of the potential, we write

$$W=W_\lambda(\lambda)+W_\mu(\mu)+W_\nu(\nu). \tag{41}$$

Furthermore, we define

$$U(\tau)=2(\tau+\alpha)(\tau+\beta)(\tau+\gamma)\left(\frac{\partial W_\tau}{\partial\tau}\right)^2-F(\tau)-\tau^2E, \qquad \tau=\lambda,\mu,\nu. \tag{42}$$

Then the Hamilton–Jacobi equation (40) becomes

$$(\nu-\mu)\,U(\lambda)+(\lambda-\nu)\,U(\mu)+(\mu-\lambda)\,U(\nu)=0, \tag{43}$$

and this has to be true for all values of λ, μ and ν. By partial differentiation with respect to τ ($\tau=\lambda$, μ, ν) we find that $U'(\tau)$ is a constant. Hence we must have

$$U(\tau)=j\tau-k, \tag{44}$$

where j and k are constants. By means of (42) we can write

$$\left(\frac{\partial W_\tau}{\partial\tau}\right)^2=p_\tau^2=\frac{\tau^2E-\tau j+k+F(\tau)}{2(\tau+\alpha)(\tau+\beta)(\tau+\gamma)}, \qquad \tau=\lambda,\mu,\nu. \tag{45}$$

These are the equations of motion. Note that p_τ is a function of τ only. Integration produces Hamilton's characteristic function. It is given by (41) with

$$W_\tau=\int\sqrt{\frac{\tau^2E-\tau j+k+F(\tau)}{2(\tau+\alpha)(\tau+\beta)(\tau+\gamma)}}\,d\tau, \qquad \tau=\lambda,\mu,\nu. \tag{46}$$

Thus, $W=W(\lambda,\mu,\nu;E,j,k)$.

The *natural* variables for the description of completely separable motion are the so-called action-angle variables (e.g. Arnold 1978; Goldstein 1980). We shall introduce them in Section 8. First we consider those properties of the stellar orbits that can be deduced from the equations of motion (45) without integrating them.

4.2 INTEGRALS

The constants j and k that occur in (45) are the values of two integrals of motion, J and K, say, that exist in a Stäckel potential in addition to the total energy $H=E$. Expressions for J and K in terms of the coordinates and conjugate momenta may be found by solving (45) for E, j and k. The resulting expressions are most easily written in terms of the quantities X, Y and Z defined as

$$\begin{aligned}
X&=\frac{p_\lambda^2}{2P^2}-\frac{F(\lambda)}{(\lambda-\mu)(\lambda-\nu)},\\
Y&=\frac{p_\mu^2}{2Q^2}-\frac{F(\mu)}{(\mu-\nu)(\mu-\lambda)},\\
Z&=\frac{p_\nu^2}{2R^2}-\frac{F(\nu)}{(\nu-\lambda)(\nu-\mu)}.
\end{aligned} \tag{47}$$

We find (Clark 1936; Lynden-Bell 1962c)

$$H=X+Y+Z,$$
$$J=(\mu+\nu)X+(\nu+\lambda)Y+(\lambda+\mu)Z,$$
$$K=\mu\nu X+\nu\lambda Y+\lambda\mu Z. \tag{48}$$

Note that all three integrals are quadratic in the velocities.

Any function of H, J and K is also an integral of motion. In order to simplify the subsequent analysis we may therefore use any three independent functions of H, J and K as integrals. It is advantageous to retain the total energy $H=E$ as integral. However, it is handy to use instead of J and K integrals I_2 and I_3 defined by

$$I_2=\frac{\alpha^2H+\alpha J+K}{\alpha-\gamma}, \qquad I_3=\frac{\gamma^2H+\gamma J+K}{\gamma-\alpha}. \tag{49}$$

The relation between these integrals and the angular momentum integrals that exist in axisymmetric and spherical potentials is discussed in Section 4.4 (see also de Zeeuw & Lynden-Bell 1985).

In terms of the values i_2 and i_3 of the integrals I_2 and I_3 the equations of motion (45) become

$$p_\tau^2=\frac{(\tau+\alpha)(\tau+\gamma)E-(\tau+\gamma)i_2-(\tau+\alpha)i_3+F(\tau)}{2(\tau+\alpha)(\tau+\beta)(\tau+\gamma)}, \tag{50}$$

where τ is equal to λ, μ or ν.

4.3 ORBIT CLASSIFICATION

For given values E, i_2 and i_3 of the integrals of motion H, I_2 and I_3, an orbit exists if, and only if, p_λ^2, p_μ^2 and p_ν^2 are all three non-negative for some values of λ, μ and ν, respectively. In each of the three coordinates motion is then either an *oscillation* (or libration) between *turning points* defined by $p_\tau^2=0$, or, if $p_\tau^2>0$ for all τ, a *rotation* ($\tau=\lambda$, μ or ν). Which combination of oscillation(s) and rotation(s) in the three coordinates occurs, follows from equation (50) upon substitution of the values of E, i_2 and i_3. This determines the class or *family* to which an orbit belongs. The intervals for which p_λ^2, p_μ^2 and p_ν^2 are non-negative define the volume allowed to the orbit by the integrals of motion. Orbits of different families have allowed volumes of different shapes. In general the frequencies of the motion in each of the three coordinates are incommensurable so that an orbit completely fills its allowed volume.

A complete classification of orbital shapes in a given Stäckel potential is obtained by determining via (50) for each combination of values of E, i_2 and i_3 whether an orbit exists and if so, to what family it belongs. We shall do this in Section 5 for the perfect ellipsoid and display the result in a three-dimensional classification diagram (Fig. 17). This shows the regions in (E, i_2, i_3)-space that correspond to the various orbit families that occur in the perfect ellipsoid.

There are a number of methods for investigating all combinations of E, i_2 and i_3 in a systematic manner. We choose to first fix values of i_2 and i_3 and consider the orbits that exist for different values of E and then repeat this process for other combinations of i_2 and i_3. For this purpose it is convenient to rewrite (50) as

$$p_\tau^2=\frac{E-i_2/(\tau+\alpha)-i_3/(\tau+\gamma)+G(\tau)}{2(\tau+\beta)}, \tag{51}$$

where $G(\tau)$ is defined in equation (22). Equation (51) may be rearranged as

$$E=2(\tau+\beta)p_\tau^2+V_{\rm eff}(\tau), \tag{52}$$

with

$$V_{\rm eff}(\tau)=\frac{i_2}{\tau+\alpha}+\frac{i_3}{\tau+\gamma}-G(\tau). \tag{53}$$

Equation (52) has the familiar form of an energy equation for one-dimensional motion in an effective potential $V_{\rm eff}(\tau)$. However, it differs in two important aspects from such an equation:

(i) It should be considered simultaneously on three intervals, one for ν, one for μ and one for λ, defined by the inequality (7).

(ii) The usual condition that motion is allowed as long as the energy exceeds the effective potential is true for λ and μ but *not* for ν: motion is allowed, i.e. $p_\tau^2\geq 0$, for values of ν, μ and λ that satisfy

$$E\leq V_{\rm eff}(\nu), \qquad E\geq V_{\rm eff}(\mu), \qquad E\geq V_{\rm eff}(\lambda). \tag{54}$$

Nevertheless, just as for one-dimensional motion, we may employ equation (52) to classify orbital shapes graphically: draw, for fixed values i_2 and i_3, the *effective potential curve*, the graph of $V_{\rm eff}$ as function of τ. A comparison with the horizontal lines $E=$constant – keeping in mind (54) – immediately yields the values of λ, μ and ν where motion is allowed (see Fig. 7 below). Turning points occur when $E=V_{\rm eff}(\tau)$, i.e. whenever the effective potential curve crosses the line of constant E.

4.4 SPECIAL CASES

It is of interest to consider briefly the axisymmetric and spherical special cases. This reveals the connection between the 'non-classical' integrals I_2 and I_3 of the triaxial case with the angular momentum integrals. It also shows how the equations of motion (51) reduce to well-known forms.

4.4.1 Prolate spheroid

The gravitational potential (24) of the perfect prolate spheroid has the x-axis as symmetry axis, so that L_x, the angular momentum component parallel to this axis, should be conserved. Indeed, upon setting $\nu=-\gamma=-\beta$ in equations (47)–(49) we find that I_3 becomes

$$I_3=\tfrac{1}{2}p_\chi^2=\tfrac{1}{2}L_x^2. \tag{55}$$

Here $p_\chi=\bar{z}\dot{\chi}=y\dot{z}-z\dot{y}$ is the momentum conjugate to χ; it is equal to L_x. The integral I_2 is still non-classical.

For general axisymmetric potentials motion is usually described as two-dimensional motion in a reduced potential $V_{\rm red}$ in a meridional plane $\chi=$constant (e.g. Ollongren 1962), with

$$V_{\rm red}=V+\frac{l_x^2}{2\bar{z}^2}, \tag{56}$$

where l_x is the value of L_x. In the present case *this reduction occurs naturally*. For $\beta=\gamma$ the range of ν is zero and (51) is valid for λ and μ only. These equations for λ and μ are identical to the

equations of motion in the two-dimensional Stäckel potential $V_{\rm red}(\lambda,\mu)$ given by

$$V_{\rm red}=V+(\beta-\alpha)i_3\frac{1/(\lambda+\alpha)-1/(\mu+\alpha)}{\lambda-\mu}, \tag{57}$$

with V given in (24). It follows from the relations between (λ,μ) and (x,z) – see Section 2.3 – that (57) is identical to (56). Thus, (51) automatically describes motion in a meridional plane. Once the motion in λ and μ has been determined, then that in χ follows from (55).

For given values E, i_2 and $i_3=\frac{1}{2}l_x^2$ of the integrals of motion the area in the meridional plane allowed to the orbit follows from a comparison of the effective potential curve (53) with the line of constant energy for λ and μ (see Fig. 19 below). Only those values of λ and μ are allowed for which $E\geq V_{\rm eff}(\lambda)$ and $E\geq V_{\rm eff}(\mu)$. The allowed area in the meridional plane defines the axisymmetric volume allowed to the orbit. The frequencies of the motions in λ, μ and χ are in general incommensurable, and the orbit will fill its allowed volume.

A complete classification of the orbital shapes is obtained by comparing effective potential curves with lines of constant energy for all values of E, i_2 and i_3 of the integrals of motion. This is done in Section 6.1. The results can then be displayed in a classification diagram, which indicates the orbital shape for each combination of E, i_2 and i_3 (Fig. 21 below).

4.4.2 Oblate spheroid

In this case we know from the axisymmetry of the potential (26) that L_z, the component of the angular momentum parallel to the z-axis, is an integral of motion. Indeed, upon setting $\mu=-\beta=-\alpha$ in equations (47)–(49) we find for I_2

$$I_2=\tfrac{1}{2}p_\phi^2=\tfrac{1}{2}L_z^2, \tag{58}$$

where $p_\phi=\varpi\dot{\phi}=x\dot{y}-y\dot{x}$ is the momentum conjugate to ϕ. It is equal to L_z. The integral I_3 is the famous third integral of Galactic dynamics (e.g. Oort 1928; Kuzmin 1953, 1956; Contopoulos 1960; Hori 1962; Ollongren 1962).

The three-dimensional motion is equivalent to two-dimensional motion in a reduced potential $V_{\rm red}=V+l_z^2/2\varpi^2$ in a meridional plane (Ollongren 1962), where l_z is the value of L_z. Just as in the prolate case, this reduction occurs naturally. For $\beta=\alpha$, the equations of motion (51) are valid only for λ and ν. They are identical to the equations of two-dimensional separable motion in the Stäckel potential $V_{\rm red}$ in a meridional plane $\phi=$constant (see also Hori 1962). Once the motion in λ and ν has been determined, then that in ϕ follows from (58).

For given values E, $i_2=\frac{1}{2}l_z^2$ and i_3 of the integrals H, I_2 and I_3 motion is allowed for all values of λ and ν for which $E\geq V_{\rm eff}(\lambda)$, and $E\leq V_{\rm eff}(\nu)$. These inequalities determine the three-dimensional axisymmetric volume in which the orbit lies. The frequencies of the motions in λ, ϕ and ν are in general incommensurable and the orbit fills its allowed volume. A complete classification of orbital shapes is obtained by a comparison of effective potential curves with lines of constant energy, for all values of i_2, i_3 and E. This is done in Section 6.2.

4.4.3 Kuzmin's disc

If we collapse the perfect oblate spheroid along the symmetry axis we obtain Kuzmin's disc. Motion in the potential of this disc can be analysed in exactly the same way as was described in the above.

We have seen in Section 3.4.5 that the potential above the disc is equal to that of a point mass M in the focus below it, and similarly for the potential below the disc. Since $I_2=\frac{1}{2}L_z^2$ in this case, it

follows that the integral I_3 should be expressible in terms of the integrals of Keplerian motion, albeit in a different way for points above and below the disc.

Taking $\mu=-\beta=-\alpha$ and $\gamma=0$ in equations (47)–(49) we find

$$I_3=\tfrac{1}{2}L_x^2+\tfrac{1}{2}L_y^2+\tfrac{1}{2}a^2\dot{z}^2-a|z|V. \tag{59}$$

Now we write $z^*=z\pm a$ and we take the plus sign for $z>0$ and the minus sign for $z<0$. In other words, we transform to Cartesian coordinates (x, y, z^*) that for points above the disc are centred on the focus below it, and for points below the disc are centred on the focus above it. Then we can write

$$I_3=\tfrac{1}{2}L_x^{*2}+\tfrac{1}{2}L_y^{*2}+a^2H\mp aA_z^*, \tag{60}$$

where

$$A_z^*=\dot{x}L_y^*-\dot{y}L_x^*+z^*V, \tag{61}$$

and $L_x^*=y\dot{z}^*-z^*\dot{y}$, $L_y^*=z^*\dot{x}-x\dot{z}^*$ and $V=-GM/\sqrt{x^2+y^2+z^{*2}}$. The first three terms in (60) are integrals of motion in any potential that is spherical with respect to $(x, y, z^*)=(0, 0, 0)$. The quantity A_z^* is the z-component of the Laplace–Runge–Lenz vector, $\mathbf{A}=\mathbf{r}\wedge\mathbf{L}+\mathbf{r}V$, which is a conserved vector only in the $1/r$ potential (Goldstein 1980, §3.9 and references therein).

4.4.4 Sphere

From equations (47)–(49) we find, upon taking $\mu=\nu=-\gamma=-\beta=-\alpha$,

$$J=\tfrac{1}{2}L^2-2\alpha H, \qquad K=\alpha^2H-\tfrac{1}{2}\alpha L^2, \qquad I_2+I_3=\tfrac{1}{2}L^2, \tag{62}$$

where $L=|\mathbf{L}|$ and $\mathbf{L}=(L_x, L_y, L_z)=(y\dot{z}-z\dot{y}, z\dot{x}-x\dot{z}, x\dot{y}-y\dot{x})$ is the angular momentum vector. From the prolate and the oblate cases discussed in the above we know that L_x and L_z are also integrals. As a result, we have four integrals of motion: E, L_x, L_y and L_z, as it should be in a spherical potential.

Since $\mu=\nu=-\alpha$, the equations of motion (51) are only valid for λ:

$$p_\lambda^2=\frac{E-(i_2+i_3)/(\lambda+\alpha)+G(\lambda)}{2(\lambda+\alpha)}. \tag{63}$$

Substitution of (28) and $\lambda+\alpha=r^2$ produces the well-known equation for radial motion in a spherical potential.

From the conservation of $\mathbf{L}$ it follows that every orbit lies in a plane through the origin. The area filled by an orbit in this plane follows from a comparison of the effective potential curve – $V_{\rm eff}$ versus λ – with a line of constant E. All values of λ are allowed for which $E\geq V_{\rm eff}(\lambda)$.

5 Classification of bound orbits

5.1 FAMILIES OF BOUND ORBITS

For the function $G(\tau)$ given in (23) the effective potential defined in (53) may still have quite different forms depending on the signs of i_2 and i_3. As a result, there is a great variety of orbital shapes in the perfect ellipsoid. The analysis of these shapes in this subsection is complete except for two intentional restrictions: we limit the analysis to bound orbits ($E<0$), and we do not (yet) discuss all limiting and transitional cases between orbits of different families.

Inspection of effective potential curves for all four combinations of signs of i_2 and i_3 reveals that no orbits exist with $i_3<0$. Fig. 7 shows such effective potential curves for the two remaining combinations of signs ($i_2<0$, $i_3>0$ and $i_2>0$, $i_3>0$). We distinguish the cases with $E>V_{\rm eff}(-\beta)$ from those with $E<V_{\rm eff}(-\beta)$. Cross-sections with the principal planes $z=0$, $y=0$ and $x=0$ of the volume allowed to the corresponding orbits are shown in Fig. 8. It is evident that the four cases shown correspond with four different general orbital shapes. We discuss each family separately.

(i) *Boxes.* For the case

$$i_2<0, \qquad i_3>0, \qquad V_{\rm eff}(-\beta)<E<0, \tag{64}$$

the allowed values for λ, μ and ν are (Fig. 7a)

$$-\gamma\leq\nu\leq\nu_{\max}, \qquad -\beta\leq\mu\leq\mu_{\max}, \qquad -\alpha\leq\lambda\leq\lambda_{\max}. \tag{65}$$

The orbit must cross the (x, z)-plane always in an area lying in that bounded by the focal hyperbola (Fig. 8a). The (y, z)-plane is crossed in an area inside the focal ellipse. A star in such an orbit oscillates back and forth in each coordinate, so that it does not have a fixed sense of rotation. Following Schwarzschild's (1979) nomenclature, we identify the orbit as a box orbit.

(ii) *Inner Long Axis Tubes.* For values of the integrals that satisfy

$$i_2<0, \qquad i_3>0, \qquad V_{\rm eff}(\mu_{\rm o})<E<V_{\rm eff}(-\beta), \tag{66}$$

where μ_0 is the value of μ for which $V_{\rm eff}$ reaches a minimum, the allowed values for λ, μ and ν are (Fig. 7b)

$$-\gamma\leq\nu\leq-\beta, \qquad \mu_{\min}\leq\mu\leq\mu_{\max}, \qquad -\alpha\leq\lambda\leq\lambda_{\max}. \tag{67}$$

The orbit lies completely outside and around the x-axis (Fig. 8b). It must cross the (x, z)-plane outside the focal hyperbola. The (y, z)-plane is crossed inside the focal ellipse. A star in this orbit has a fixed sense of rotation around the x-axis since there are no turning points in ν. The orbit is a tube orbit around the long axis. Since z-axis crossings occur between the *inner foci* at $z=\pm\sqrt{\gamma-\beta}$ and the *outer foci* at $z=\pm\sqrt{\gamma-\alpha}$, we shall refer to it as an inner long axis tube.

(iii) *Outer Long Axis Tubes.* For

$$i_2>0, \qquad i_3>0, \qquad V_{\rm eff}(\lambda_0)<E<V_{\rm eff}(-\beta), \tag{68}$$

where λ_0 is the value of λ where $V_{\rm eff}$ reaches a minimum, the allowed values for λ, μ, and ν are (Fig. 7c)

$$-\gamma\leq\nu\leq-\beta, \qquad \mu_{\min}\leq\mu\leq-\alpha, \qquad \lambda_{\min}\leq\lambda\leq\lambda_{\max}. \tag{69}$$

The allowed volume lies outside and completely around the x-axis (Fig. 8c). The corresponding orbit crosses the (x, z)-plane outside the focal hyperbola; crossing of the (y, z)-plane takes place outside the focal ellipse. Again there are no turning points in ν so that a star in this orbit has a fixed sense of rotation around the x-axis. The z-axis is crossed outside the outer foci. We shall call this orbit an outer long axis tube.

(iv) *Short Axis Tubes.* For

$$i_2>0, \qquad i_3>0, \qquad \left.\begin{matrix} V_{\rm eff}(-\beta) \\ V_{\rm eff}(\lambda_0) \end{matrix}\right\}<E<0, \tag{70}$$

where λ_0 is the value of λ where $V_{\rm eff}$ reaches a minimum, motion is allowed for (Fig. 7d)

$$-\gamma\leq\nu\leq\nu_{\max}, \qquad -\beta\leq\mu\leq-\alpha, \qquad \lambda_{\min}\leq\lambda\leq\lambda_{\max}. \tag{71}$$

The corresponding orbit lies outside and around the z-axis (Fig. 8d). It crosses the (x, z)-plane in an area lying in that bounded by the focal hyperbola. The (y, z)-plane is crossed outside the focal ellipse. There are no turning points in μ so that a star in this orbit has a definite sense of rotation around the z-axis. It is a short axis tube.

It should be remarked that for all three tube orbit families both clockwise and anticlockwise motion around the appropriate axis is allowed, and in the same volume.

Before we can construct the full three-dimensional classification diagram in (E, i_2, i_3)-space we need to establish the precise boundaries of the four regions corresponding to the four families of general orbits we have found. These boundaries, and the corresponding limiting and transitional orbits, follow upon substitution of equality signs in all inequalities given in equations (64), (66), (68) and (70). They can, however, also be obtained by a careful investigation of the motion in the principal planes.

Of special importance are the orbits for which motion is in one coordinate only. These are the *simple periodic orbits*. They all lie in the principal planes. From the symmetry of the potential V with respect to these planes it follows that the oscillations along each of the principal axes are among the simple periodic orbits.

In the following three subsections we study, in turn, motion in each of the three principal planes. The symmetry of the potential ensures that a star moving in such a plane will remain in it, so that motion is two-dimensional. As a result, we can construct for each principal plane a two-dimensional classification diagram (Figs 10, 13 and 16). These diagrams are cross-sections of the full three-dimensional classification diagram Fig. 17. The reader who is not interested in the detailed description of the motion in the principal planes should turn his attention to Section 5.5.

5.2 ORBITS IN THE (x, y)-PLANE

All orbits in this plane must have $z=0$, i.e. $\nu=-\gamma$, and therefore require $p_\nu^2/2R^2=0$ for $\nu=-\gamma$. From equation (51) it then follows that for all orbits in the (x, y)-plane

$$i_3=0. \tag{72}$$

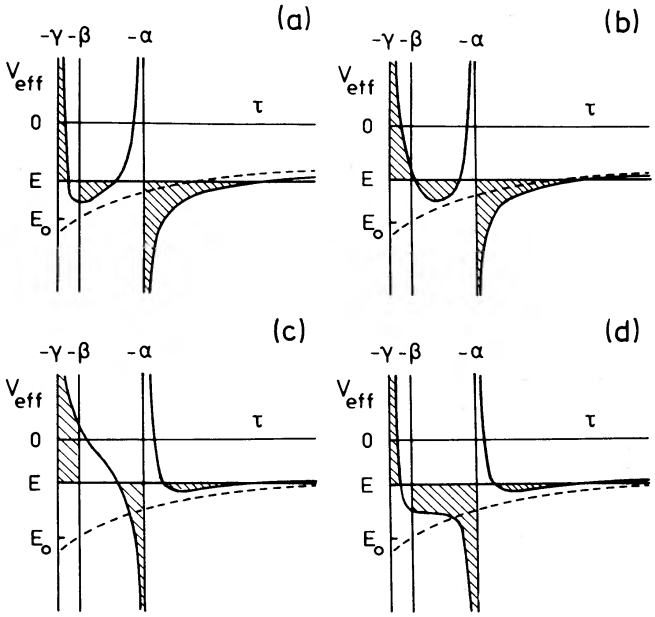

Figure 7. Effective potential curves for the four families of general orbits in the perfect ellipsoid. The dashed curve is $-G(\tau)$. The area between the line of constant E and $V_{\rm eff}(\tau)$ in the intervals where equation (54) is satisfied is hatched. (a) Box; (b) inner long axis tube; (c) outer long axis tube; (d) short axis tube.

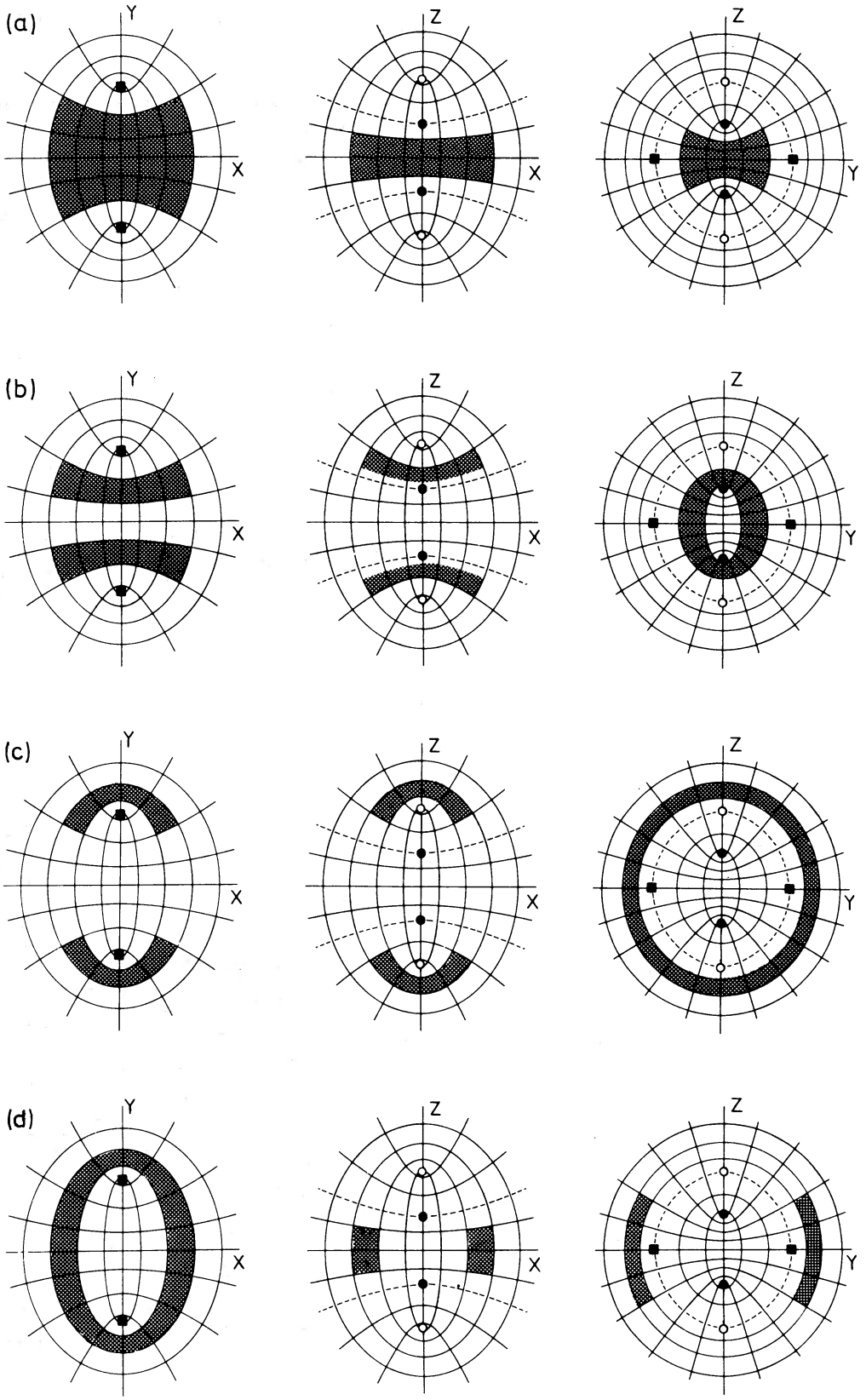

Figure 8. Cross-sections with the three principal planes of the volumes allowed to the four general orbits by the values of the integrals of motion. The dashed curves indicate the focal hyperbola [(x, z)-plane] and the focal ellipse [(y, z)-plane]. The foci are denoted by the same symbols as in Fig. 2. (a) Box orbit; (b) inner long axis tube; (c) outer long axis tube; (d) short axis tube.

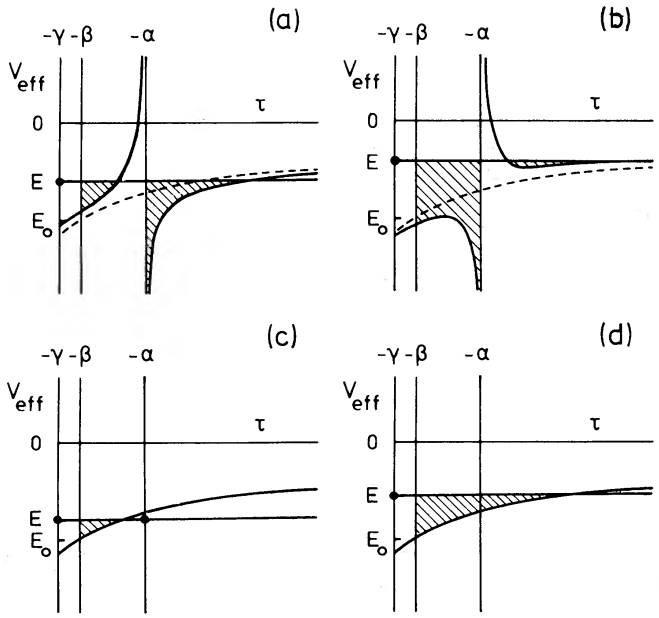

Figure 9. Effective potential curves for orbits in the (x, y)-plane of the perfect ellipsoid. (a) Butterfly; (b) loop; (c) stable y-axis orbit; (d) unstable y-axis orbit.

The remaining equations of motion are

$$p_\tau^2=\frac{E-\{i_2/(\tau+\alpha)\}+G(\tau)}{2(\tau+\beta)}, \qquad \tau=\lambda,\mu. \tag{73}$$

These two equations are identical to the equations of motion for strict two-dimensional separable motion in a potential $V(x, y, 0)$ given by

$$V(x, y, 0)=-\frac{(\lambda+\alpha)G(\lambda)-(\mu+\alpha)G(\mu)}{\lambda-\mu}, \tag{74}$$

which is of two-dimensional Stäckel form in the elliptic coordinates (λ, μ).

Fig. 9 shows effective potential curves for $i_3=0$. Since $1/R^2=0$ for $\nu=-\gamma$, the condition $\dot{z}^2=p_\nu^2/R^2=0$ for $\nu=-\gamma$ does not imply that $p_\nu^2=0$ in the (x, y)-plane. As a result, the line of constant E does not necessarily intersect the effective potential curve at $\nu=-\gamma$ [*cf.* equation (51)]. This can also be deduced by considering the effective potential curves shown in Fig. 7 and letting i_3 go to zero. The area filled by an orbit in the (x, y)-plane can be found for each value of i_2 and E in exactly the same way as described in Section 4.3 by comparing $V_{\rm eff}$ with lines of constant E, but only for λ and μ. We find two possible shapes for a general orbit in this plane:

Butterflies. For $i_2<0$ the orbits are boxes collapsed in the z-direction. They cross the y-axis always between the foci (compare Fig. 8a) and have no fixed sense of rotation. Following Binney (1982) we call them butterflies.

Loops. For $i_2>0$ the orbits are short axis tubes, collapsed in the (x, y)-plane. They cross the y-axis outside the foci (compare Fig. 8d) and have a fixed sense of rotation around the centre. They are loop orbits.

Next we consider the simple periodic orbits. Three types exist in the (x, y)-plane. In addition to the oscillations along the x- and y-axes, also the curves $\lambda=\lambda_0$ in this plane are solutions of the equations of motion. They are elliptic closed orbits.

The x-axis is given by $\nu=-\gamma$ and $\mu=-\beta$. An oscillation along this axis may be considered as a butterfly orbit collapsed in the y- (or μ-) direction. From Fig. 9a it follows that this is a solution of the equations of motion if and only if $E=V_{\rm eff}(-\beta)$. This results in the following conditions on the integrals of motion

$$i_2=(\alpha-\beta)(E-E_0), \qquad i_3=0, \qquad E_0\leq E\leq 0, \tag{75}$$

where

$$E_0=-G(-\beta). \tag{76}$$

The energy E_0 equals the value $V(0,0,0)$ of the gravitational potential in the centre. The value of $G(-\beta)$ for the perfect ellipsoid, and the other special values of $G(\tau)$ and $G'(\tau)$ which we shall encounter below, are all given in Appendix B. For a given value of E the amplitude ($\lambda_{\rm max}$ or $x_{\rm max}$) can be calculated by solving $p_\lambda^2=0$. Not surprisingly, the result is that $x_{\rm max}$ follows from $E=V(x_{\rm max},0,0)$ with

$$V(x,0,0)=-\frac{(\lambda+\alpha)G(\lambda)-(\alpha-\beta)G(-\beta)}{\lambda+\beta}, \qquad x^2=\lambda+\alpha, \tag{77}$$

Note that for $E=E_0$ we find $i_2=i_3=0$ and $x_{\rm max}=0$ so that the star is at rest in the centre.

The y-axis is given by

$$\begin{aligned} &\nu=-\gamma, \quad \lambda=-\alpha, \quad \text{for } 0\leq|y|\leq\sqrt{\beta-\alpha},\\ &\nu=-\gamma, \quad \mu=-\alpha, \quad \text{for } \sqrt{\beta-\alpha}\leq|y|. \end{aligned} \tag{78}$$

An oscillation along the y-axis is a solution of the equations of motion if and only if

$$i_2=0, \qquad i_3=0, \qquad E_0\leq E\leq 0. \tag{79}$$

The amplitude $y_{\rm max}$ is the solution of $E=V(0,y_{\rm max},0)$ where

$$V(0,y,0)=-G(\tau), \qquad y^2=\tau+\beta, \qquad \tau=\lambda \text{ or } \mu. \tag{80}$$

The orbit reaches the foci at $y=\pm\sqrt{\beta-\alpha}$ for an energy E_2 given by

$$E_2=-G(-\alpha). \tag{81}$$

Consider the region allowed by the values of the integrals given in (79). Fig. 9c shows the effective potential curve for the case $E_0<E<E_2$. Although the line of constant energy does not intersect the effective potential curve at $\lambda=-\alpha$, still $\dot{x}^2=p_\lambda^2/P^2=0$ there, since $1/P^2=0$ for $\lambda=-\alpha$. From Fig. 9c it follows that $p_\lambda^2<0$ for all $\lambda\neq-\alpha$, so that, as expected, the allowed region is a segment of the y-axis between the foci. Here the y-axis can be considered as a butterfly orbit, collapsed in the x-direction. However, for $E_2<E<0$ the situation is different (Fig. 9d). Now the allowed region is an area, bounded by the ellipse $\lambda=\lambda_{\rm max}$. As required, $p_\mu^2/Q^2=0$ for $\mu=-\alpha$, but $p_\mu^2>0$ for all $\mu\neq-\alpha$. This means that for these energies the oscillations along the y-axis are unstable to perpendicular perturbations. Any small perturbation in μ will make $p_\mu^2>0$ so that the star will keep moving away from the y-axis; it orbits in the allowed elliptic area. From the above it follows that for $E_0<E<E_2$ a y-axis oscillation is stable, so that the change of stability occurs at $E=E_2$, when the orbit just reaches the foci. Note that by a similar argument we find that the x-axis orbits are always stable.

The *elliptic closed orbits* are loop orbits collapsed in the λ-direction. They occur for values of E and i_2 for which $E=V_{\rm eff}(\lambda_0)$ and $V_{\rm eff}$ has a minimum at λ_0. Thus, a parametric representation of the relation between E and i_2 for these orbits is

$$i_2=-(\lambda_0+\alpha)^2G'(\lambda_0), \qquad E=-G(\lambda_0)-(\lambda_0+\alpha)G'(\lambda_0). \tag{82}$$

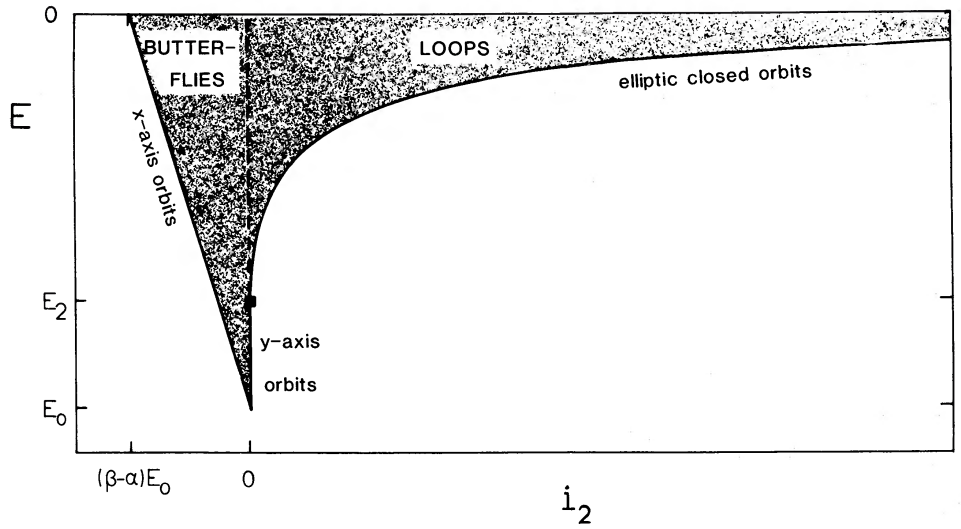

Figure 10. Classification of orbits in the (x, y)-plane of the perfect ellipsoid in terms of the integrals E and i_2. Each point in the shaded region corresponds with a bound orbit. The dashed line represents the unstable y-axis orbit.

The elliptic closed orbits are stable and exist for all energies in the range $E_2<E<0$. At $E=E_2$, i.e. $\lambda_0=-\alpha$, they branch off the y-axis orbit which at this energy becomes unstable, as we have seen. *This means that the foci are the points of bifurcation on the y-axis.*

Fig. 10 illustrates the relations between E and i_2 for the three families of simple periodic orbits in the (x, y)-plane. Together with the line $E=0$, these relations form the boundary of the area in the (E, i_2)-plane that corresponds to bound orbits in the (x, y)-plane of the perfect ellipsoid. Each point in the shaded region represents one orbital shape. Clearly, the general orbits are divided, by the unstable y-axis orbit, in two families, one having $i_2<0$, the other with $i_2>0$. These are just the two families mentioned earlier, the butterflies and the loops. This two-dimensional classification diagram Fig. 10 is the cross-section $i_3=0$ of the three-dimensional diagram Fig. 17.

We have seen that x-axis orbits are collapsed butterflies and that the elliptic closed orbits are collapsed loops. Conversely, we may consider these periodic orbits as the progenitors or *parents* of the general orbits. Butterflies are x-axis orbits with a superposed μ-oscillation and loops are elliptic closed orbits with a superposed λ-oscillation.

Finally, we remark that for all orbits in the (x, y)-plane the effective potential curves shown in Fig. 9 tell us that $p_\nu^2<0$ for all $\nu\neq-\gamma$. As a result, all orbits in this plane are stable against perpendicular perturbations (perturbations out of the plane).

5.3 ORBITS IN THE (x, z)-PLANE

Motion in this plane is identical to two-dimensional motion in the potential $V(x, 0, z)$ given by

$$V(x, 0, z)=-\frac{g(\lambda)-g(\sigma)}{\lambda-\sigma}, \qquad \sigma=\mu \quad \text{or} \quad \nu, \tag{83}$$

with

$$g(\tau)=\frac{(\tau+\alpha)(\tau+\gamma)\,G(\tau)-(\alpha-\beta)(\gamma-\beta)\,G(-\beta)}{\tau+\beta}. \tag{84}$$

$V(x, 0, z)$ is of Stäckel form in elliptic coordinates (λ, σ) with foci on the z-axis at $z=\pm\sqrt{\gamma-\alpha}$ (Table 1).

All orbits in the (x, z)-plane must have $y=0$, i.e. $\mu=-\beta$ or $\nu=-\beta$, which in either case requires $E=V_{\rm eff}(-\beta)$ or

$$E-E_0=\frac{i_2}{\alpha-\beta}+\frac{i_3}{\gamma-\beta}. \tag{85}$$

Classification of orbital shapes can be done as before, but now with (85) as constraint on the values of the integrals of motion. Effective potential curves for this case are shown in Fig. 11.

The general orbits in the (x, z)-plane are butterflies and loops. Unlike the case of the (x, y)-plane, here not all general orbits are stable against perturbations out of the plane. *Stable and unstable butterflies* occur for $i_2>0$. They are stable when $V_{\rm eff}$ has a minimum in the range of ν (Fig. 11a) and are just box orbits collapsed in the y-direction. They lie in the area between the two branches of the focal hyperbola (compare Fig. 8a). When $V_{\rm eff}$ has a minimum in the range of μ (Fig. 11b) the allowed volume is three-dimensional. Cross-sections of this volume are shown in Fig. 12a. These are butterfly-shaped areas in the (x, y)- and (x, z)-planes, the latter containing part of the focal hyperbola. In the (y, z)-plane these orbits cross in an elliptic area inside the focal ellipse. By a reasoning similar to that for the y-axis (Section 5.2) we conclude that these butterflies are unstable. Stable and unstable butterflies in the (x, z)-plane are separated by *critical butterflies*, which occur when $V_{\rm eff}$ has a minimum in $\mu=\nu=-\beta$, equal to E. We find for these orbits

$$i_2=\frac{(\alpha-\beta)^2}{\alpha-\gamma}(E-E_1), \qquad E_1<E<0, \tag{86}$$

where

$$E_1=-G(-\beta)-(\gamma-\beta)G'(-\beta), \tag{87}$$

and i_3 follows from (85). The critical butterflies are bounded by parts of the focal hyperbola. *Unstable loops* occur for $i_2>0$ (Fig. 11c). All loops are unstable to perturbations out of the plane (Fig. 12b). The allowed region is an ellipsoidal shell of finite thickness.

Now consider the simple periodic orbits. The x-axis oscillation was already discussed in Section 5.2. The z-axis is given by

$$\begin{aligned}
&\mu=-\beta,\ \lambda=-\alpha, \quad \text{for } 0\le|z|\le\sqrt{\gamma-\beta},\\
&\nu=-\beta,\ \lambda=-\alpha, \quad \text{for } \sqrt{\gamma-\beta}\le|z|\le\sqrt{\gamma-\alpha},\\
&\nu=-\beta,\mu=-\alpha, \quad \text{for } \sqrt{\gamma-\alpha}\le|z|.
\end{aligned} \tag{88}$$

An oscillation along the z-axis is a solution of the equations of motion if

$$i_2=0, \qquad i_3=(\gamma-\beta)(E-E_0), \qquad E_0\le E\le 0. \tag{89}$$

The amplitude $z_{\rm max}$ follows from $E=V(0, 0, z_{\rm max})$ with

$$V(0, 0, z)=-\frac{(\tau+\gamma)G(\tau)-(\gamma-\beta)G(-\beta)}{\tau+\beta}, \qquad z^2=\tau+\gamma. \tag{90}$$

For $E=E_1$, defined in (87), the orbit just reaches the inner foci at $z=\pm\sqrt{\gamma-\beta}$. The outer foci, at $z=\pm\sqrt{\gamma-\alpha}$, are reached for $E=E_3$ defined by

$$E_3=-\frac{(\gamma-\alpha)G(-\alpha)-(\gamma-\beta)G(-\beta)}{\beta-\alpha}. \tag{91}$$

From our experience with the y-axis orbits in Section 5.2 we expect that stability changes occur at

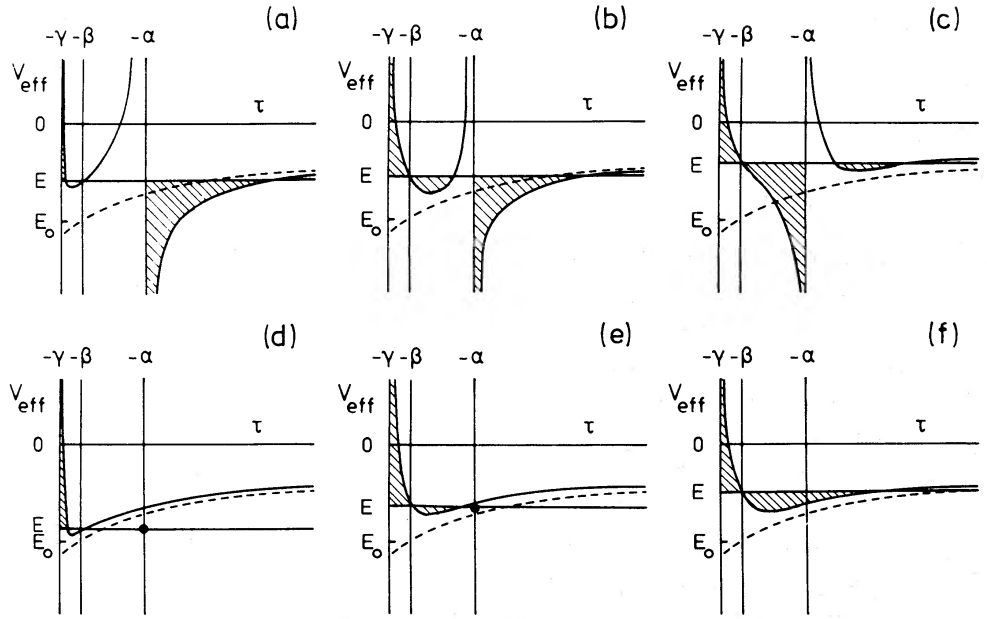

Figure 11. Effective potential curves for orbits in the (x, z)-plane of the perfect ellipsoid. (a) Stable butterfly; (b) unstable butterfly; (c) unstable loop; (d) stable z-axis orbit; (e) unstable z-axis orbit; (f) twice unstable z-axis orbit.

the foci. This is indeed the case, as inspection of the effective potential curves in Fig. 11d, e and f shows. For $E_0 \leq E < E_1$ a z-axis oscillation is stable and can be considered as a stable butterfly collapsed in the λ-direction. For $E_1 < E < E_3$ the allowed region is an area in the (y, z)-plane, bounded by the ellipse $\mu = \mu_{\max} = z^2_{\max} - \gamma$. For these energies a z-axis orbit is therefore unstable to perturbations in the y-direction. A z-axis orbit is unstable in both the y- and the z-direction for $E_3 < E < 0$. The region allowed by (89) is now a volume, bounded by the ellipsoid $\lambda = \lambda_{\max} = z^2_{\max} - \gamma$.

In the (x, z)-plane there are also *elliptic closed* orbits. The curves $\lambda = \lambda_0$ are solutions of the equations of motion (51) (compare Fig. 11c). The orbits exist for energies in the range $E_3 < E < 0$, and branch off the z-axis orbit at the outer foci. The relations between the integrals of motion for these orbits follows from $E = V_{\text{eff}}(\lambda_0)$ with V_{eff} having a minimum at λ_0. In parametric form

$$i_2 = -\frac{(\beta-\alpha)}{(\gamma-\alpha)}[(\lambda_0+\alpha)^2 \tilde{g}'(\lambda_0) + (\gamma-\beta)\, G(-\beta)],$$

$$E = -\tilde{g}(\lambda_0) - (\lambda_0+\alpha)\tilde{g}'(\lambda_0), \tag{92}$$

where $\tilde{g}(\tau) = g(\tau)/(\tau+\alpha)$ and $g(\tau)$ is defined in (84). The values of i_3 follow upon substitution of (92) in (85). Just as the loop orbits in this plane, the elliptic closed orbits are unstable to perturbations out of the plane. The values of the integrals given by (92) not only allow the ellipse $\lambda = \lambda_0$ in the plane, but instead allow the whole ellipsoid $\lambda = \lambda_0$ (compare Fig. 12b).

The above results are summarized in Fig. 13, an orbit classification diagram of E versus i_2. The simple periodic orbits and the line $E = 0$ bound the area that corresponds to bound orbits in the (x, z)-plane of the perfect ellipsoid. As long as we disregard perpendicular instability, the diagram is similar to Fig. 10 for the (x, y)-plane. This is as expected, since both describe strict two-dimensional motion in similar non-axisymmetric potentials. When considered as principal planes of the same three-dimensional potential, however, perpendicular instability becomes important for the (x, z)-plane. As a result, Fig. 13 is richer in structure than Fig. 10.

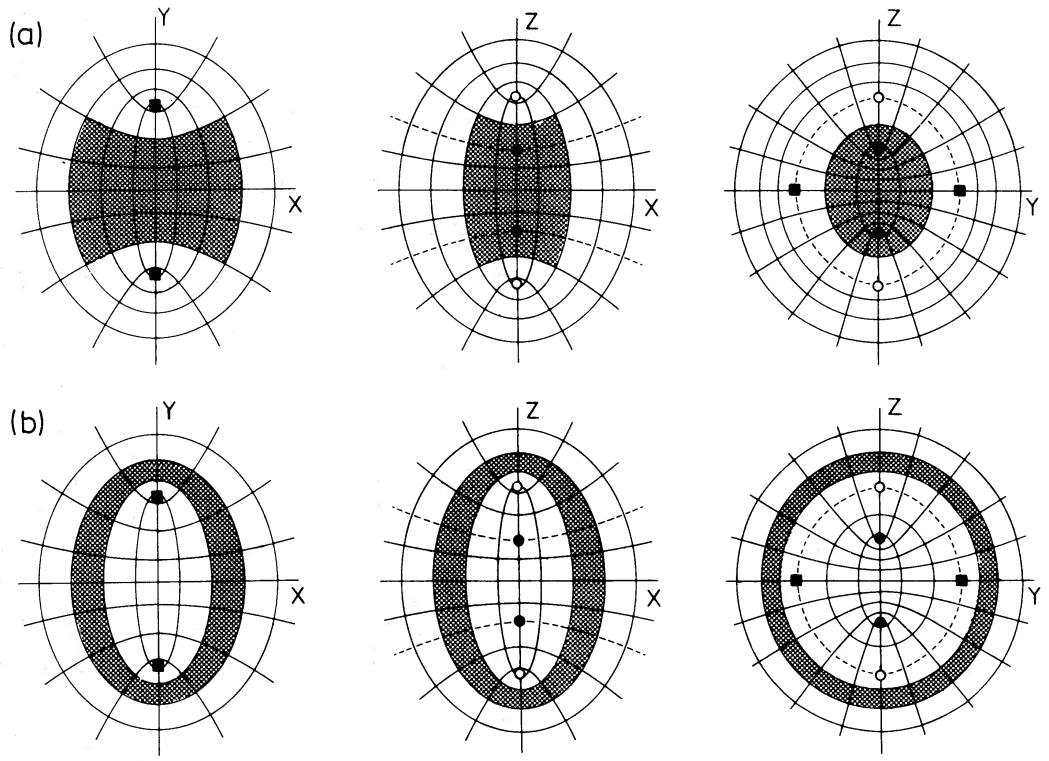

Figure 12. Cross-sections with the principal planes of the volume allowed by the values of the integrals of motion for the two unstable orbits in the (x, z)-plane of the perfect ellipsoid. (a) Unstable butterfly; (b) unstable loop.

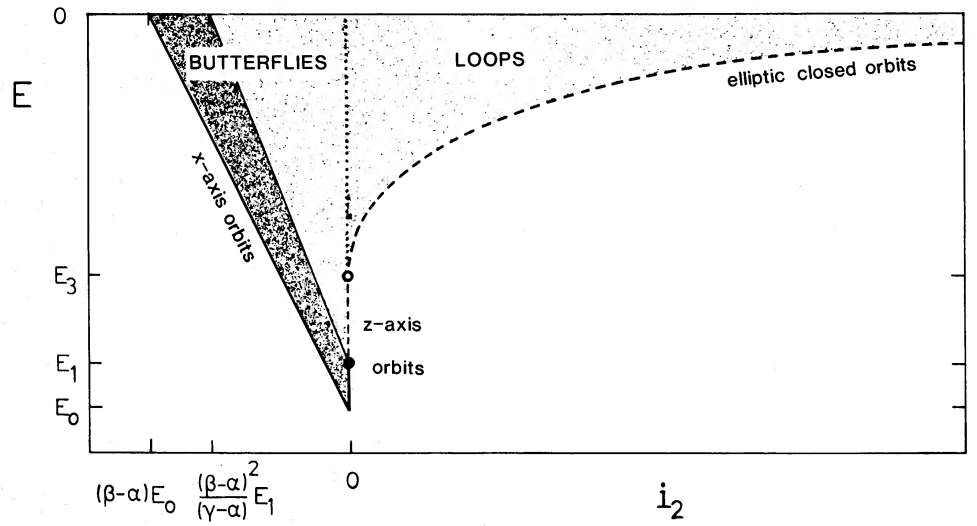

Figure 13. Classification of orbits in the (x, z)-plane of the perfect ellipsoid in terms of the integrals E and i_2. The shaded area corresponds with stable bound orbits, the light shaded area with unstable bound orbits. Dashed lines represent once unstable periodic orbits, the dotted line twice unstable periodic orbits.

5.4 ORBITS IN THE (y, z)-PLANE

Motion in this plane is identical to two-dimensional motion in the potential $V(0, y, z)$ given by

$$V(0, y, z) = -\frac{(\varkappa+\gamma)G(\varkappa)-(\nu+\gamma)G(\nu)}{\varkappa-\nu}, \qquad \varkappa=\lambda \quad \text{or} \quad \mu, \tag{93}$$

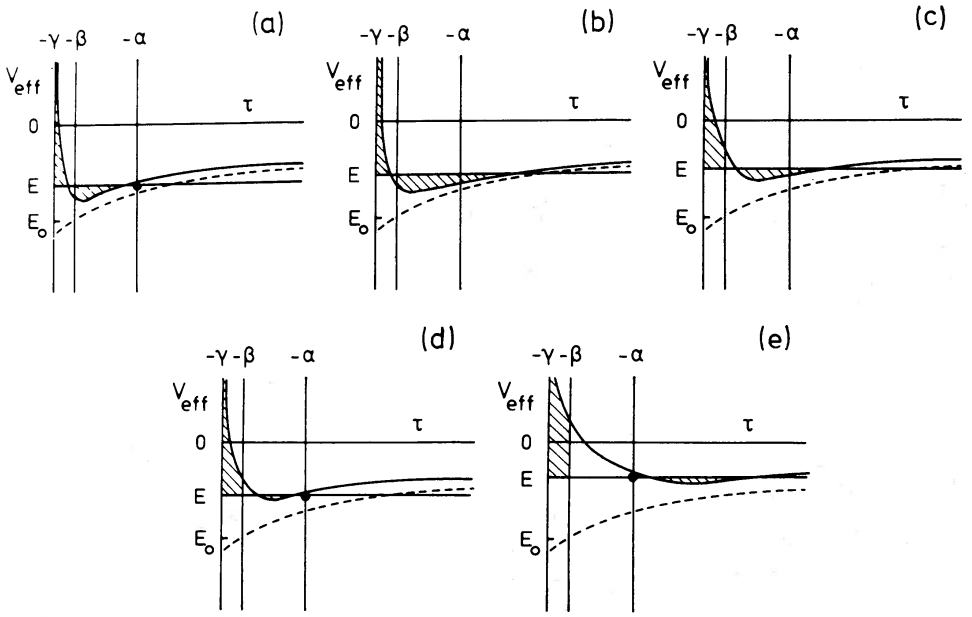

Figure 14. Effective potential curves for orbits in the (y, z)-plane of the perfect ellipsoid. (a) Stable butterfly; (b) unstable butterfly; (c) unstable loop; (d) inner stable loop; (e) outer stable loop.

which is of two-dimensional Stäckel form in elliptic coordinates $(\varkappa, \nu)$ with foci on the z-axis at $z=\pm\sqrt{\gamma-\beta}$ (*cf.* Table 1).

The condition $x=0$ for all orbits, i.e. $\lambda=-\alpha$ or $\mu=-\alpha$, requires

$$i_2=0. \tag{94}$$

The general orbits are butterflies and loops. Due to perpendicular instability we have to distinguish five types of general orbits in the (y, z)-plane. Effective potential curves are given in Fig. 14.

Stable and unstable butterflies. For $E<V_{\rm eff}(-\alpha)$ they are stable (Fig. 14a). They are box orbits collapsed in the x-direction, and lie inside the focal ellipse (compare Fig. 8a). For $E>V_{\rm eff}(-\alpha)$ the butterflies are unstable (Fig. 14b). The values of the integrals of motion now allow a three-dimensional volume, cross-sections of which are shown in Fig. 15a. The stable and unstable butterflies are separated by *critical* butterflies, which occur for $E=V_{\rm eff}(-\alpha)$, i.e.

$$i_3=(\gamma-\alpha)(E-E_2), \qquad E_2<E<0. \tag{95}$$

A critical butterfly is bounded by parts of the focal ellipse.

Stable and unstable loops. Unstable loops occur for $E>V_{\rm eff}(-\alpha)$ (Fig. 14c). The values of the integrals of motion allow the three-dimensional volume shown in Fig. 15b. This contains the focal ellipse. For $E<V_{\rm eff}(-\alpha)$ the loops are stable to perturbations out of the plane (Fig. 14d, e). They lie either inside or outside the focal ellipse, and are inner and outer long axis tubes collapsed in the x-direction (compare Fig. 8b, c). Stable and unstable loops are separated by *critical* loops, which occur for $E=V_{\rm eff}(-\alpha)$ [*cf.* (95)]. They touch the focal ellipse either on the inside or on the outside.

Of the simple periodic orbits the oscillations along the y- and z-axis have already been discussed in Sections 5.2 and 5.3. In the (y, z)-plane the z-axis orbit becomes unstable to perturbations in the y-direction at $z=\pm\sqrt{\gamma-\beta}$. Here *elliptic closed orbits* branch off; they exist for all energies in the range $E_1<E<0$. The relation between E and i_3 follows from $E=V_{\rm eff}(\varkappa_0)$ and the requirement that $V_{\rm eff}$ has a minimum at $\varkappa_0$ (compare Fig. 14d, e):

$$i_3=-(\varkappa_0+\gamma)^2 G'(\varkappa_0), \qquad E=-G(\varkappa_0)-(\varkappa_0+\gamma)G'(\varkappa_0), \qquad -\beta<\varkappa_0. \tag{96}$$

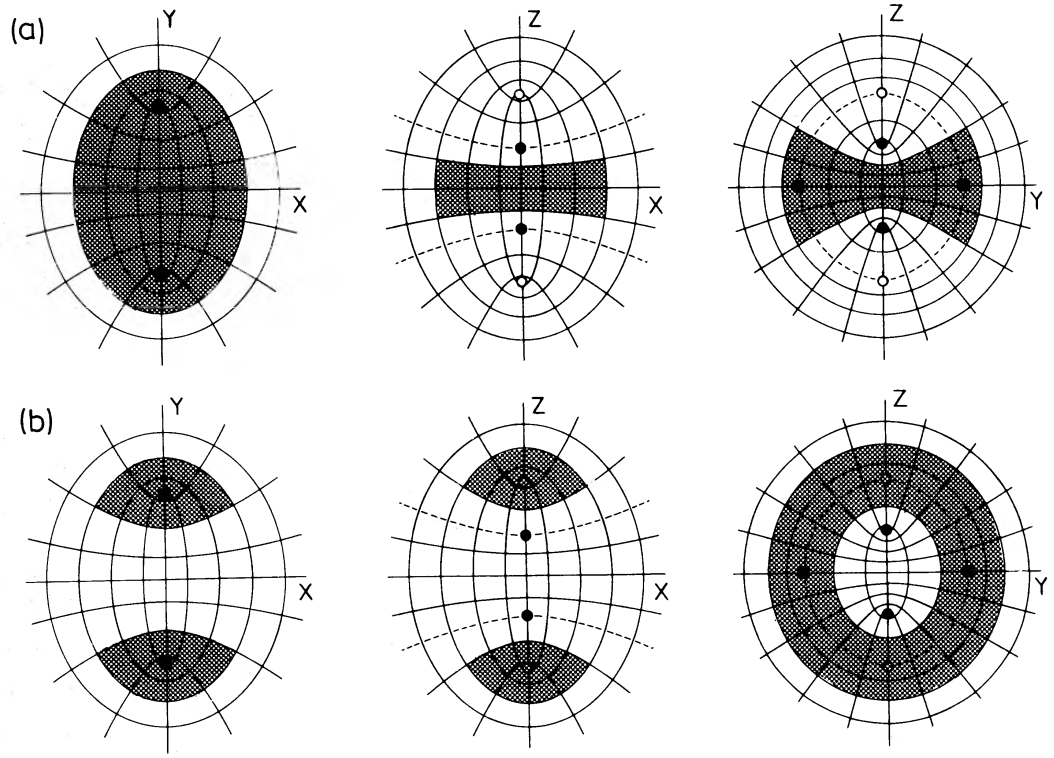

Figure 15. Cross-sections with the principal planes of the volume allowed by the values of the integrals of motion for the two unstable orbits in the (y, z)-plane of the perfect ellipsoid. (a) Unstable butterfly; (b) unstable loop.

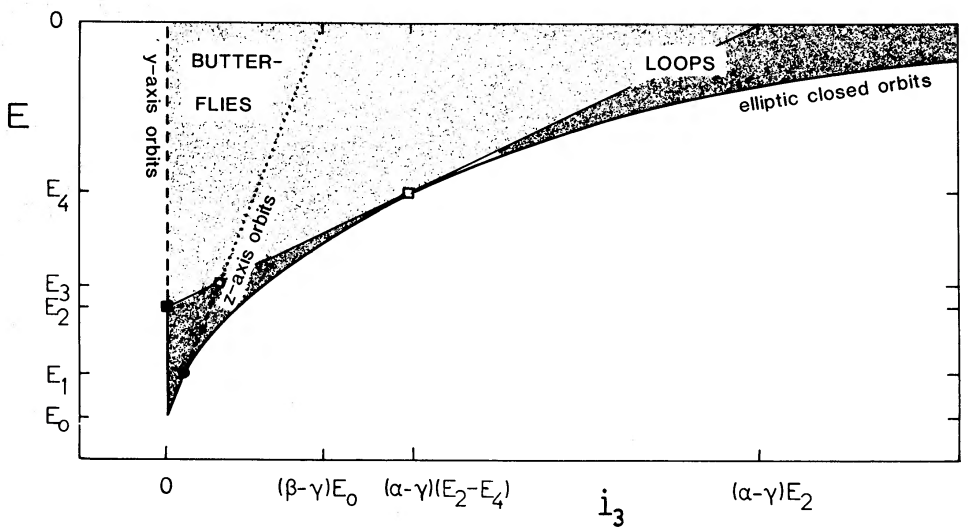

Figure 16. Classification of orbits in the (y, z)-plane of the perfect ellipsoid in terms of the integrals E and i_3. Shadings, dashed and dotted lines have the same meaning as in Fig. 13.

The elliptic closed orbit coincides with the focal ellipse for $\varkappa_0=-\alpha$. This occurs for $E=E_4$ where

$$E_4=-G(-\alpha)-(\gamma-\alpha)G'(-\alpha). \tag{97}$$

The corresponding value of i_3 is equal to $-(\gamma-\alpha)^2G'(-\alpha)$.

The classification diagram of E versus i_3 is shown in Fig. 16. It is the cross-section $i_2=0$ of the three-dimensional classification diagram Fig. 17. When we ignore the different shadings in Fig. 16 it is similar to the corresponding diagrams 10 and 13 for the other principal planes. The relatively

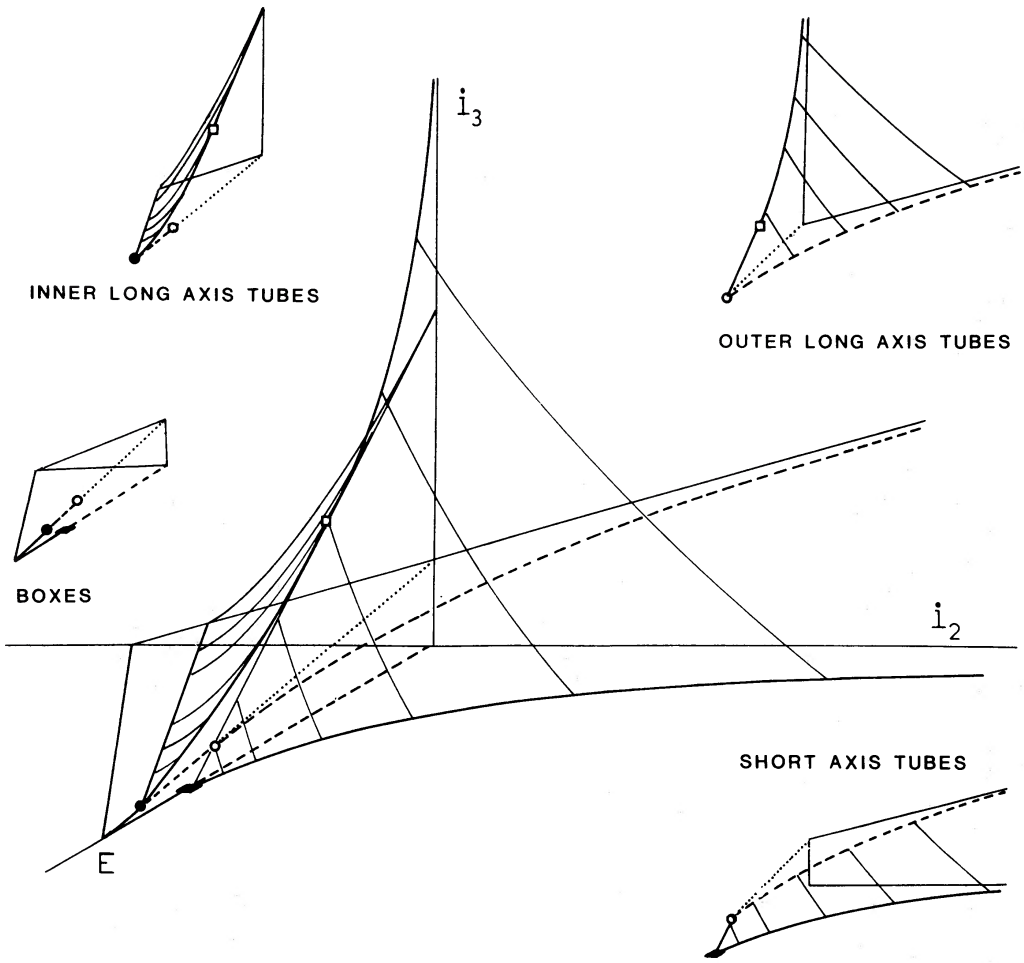

Figure 17. Three-dimensional classification of orbits in the perfect ellipsoid in terms of the integrals E, i_2 and i_3. Each point within the volume shown corresponds with a bound orbit. Dashed and dotted lines have the same meaning as in Fig. 13. The three planar cross-sections in which each point corresponds to an orbit in one of the principal planes, are shown with more detailed explanations in Figs 10, 13 and 16. They separate the four volumes, identified by separate insets, that correspond with the four families of three-dimensional orbits.

long (i.e. y-) axis orbits are the parents of the butterflies; the loops are generated by the elliptic closed orbits. The relatively short (i.e. z-axis) orbits, unstable, separate the two. Again it is the perpendicular instability that is responsible for a more complicated picture. Five different areas can be distinguished in the diagram, each corresponding to one of the five types of loops and butterflies we discussed in the above.

Finally we note that we have the following inequalities

$$E_0<E_1<E_3<E_4<0, \qquad E_0<E_2<E_3<E_4<0. \tag{98}$$

5.5 THE THREE-DIMENSIONAL CLASSIFICATION DIAGRAM

We have now completed the classification of the orbital shapes in the perfect ellipsoid. Figs 10, 13 and 16 are the classification diagrams for motion in each of the three principal planes. Figs 10 and 16 are cross-sections ($i_3=0$ and $i_2=0$, respectively) of the three-dimensional volume in (E, i_2, i_3)-space that corresponds to bound orbits in the perfect ellipsoid. This volume is shown in Fig. 17. The cross-section $E=V_{\rm eff}(-\beta)$ that described motion in the (x, z)-plane of the perfect ellipsoid, is similar to Fig. 13 which is the projection of this cross-section onto the plane $i_3=0$. It is evident that

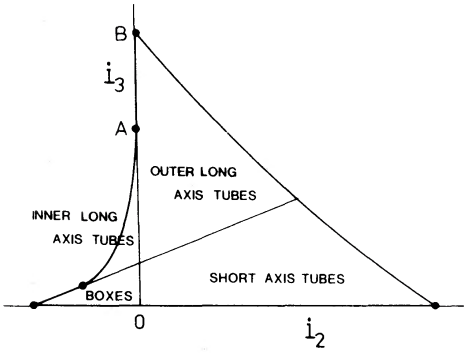

Figure 18. Cross-section of Fig. 17 with a plane of constant $E(E_4<E<0)$.

the planes $i_3=0$, $E=V_{\rm eff}(-\beta)$ and $i_2=0$ play an important role: they bound as well as separate the four volumes that correspond to the four families of general orbits. For clarity these four volumes are shown as separate insets in Fig. 17. Fig. 18 is a cross-section with a plane of constant E, where $E_4<E<0$. For $E_3<E<E_4$ the point B lies below the point A on the i_2-axis.

Box orbits occur for values of the integrals that lie in the volume bounded by the three planes just mentioned (as well as by the plane $E=0$). These three planes also form bounding surfaces of the volumes corresponding to the three tube orbit families. The latter are further bounded by two curved surfaces. Both of these have a parametric representation of the form

$$E=V_{\rm eff}(\varkappa_0),\ \frac{dV_{\rm eff}(\varkappa_0)}{d\varkappa}=0,\qquad -\beta<\varkappa_0, \tag{99}$$

or equivalently,

$$i_2=-(\varkappa_0+\alpha)^2\left\{\frac{i_3}{(\varkappa_0+\gamma)^2}+G'(\varkappa_0)\right\},$$

$$E=-G(\varkappa_0)-(\varkappa_0+\alpha)\,G'(\varkappa_0)+\frac{(\gamma-\alpha)\,i_3}{(\varkappa_0+\gamma)^2},\qquad -\beta<\varkappa_0. \tag{100}$$

For $-\beta<\varkappa_0<-\alpha$ this describes the curved surface in Fig. 17 for which $i_2<0$. Inspection of Fig. 7b reveals that the values (100) of the integrals of motion in this case correspond to *infinitesimally thin inner long axis tubes*. For $-\alpha<\varkappa_0$ equation (100) describes the curved surface in Fig. 17 with $i_2>0$. Values of the integrals of motion on this surface give *infinitesimally thin outer long axis tubes* or *infinitesimally thin short axis tubes* as can be seen from Fig. 7c and d. When the values of the integrals lie not only on the surface (100), but also on one of the surfaces $i_2=0$, $i_3=0$ or $E=V_{\rm eff}(-\beta)$ the infinitesimally thin tubes are confined to a principal plane of the perfect ellipsoid, and hence are elliptic closed orbits. Thus, the surface (100) contains the curves in Figs 10, 13 and 16 that describe these simple periodic orbits.

Fig. 17 also illustrates why various orbits in the (x, z)- and (y, z)-planes are unstable to perpendicular perturbations. When a part of the appropriate classification diagram separates two general orbit families, the corresponding planar orbits are unstable. The orbits are stable when they lie on the boundary of one family of general orbits. This can be deduced also by a comparison of the cross-sections with the principal planes of the various orbit families encountered in the preceding sections. Fig. 17 makes this result transparent in terms of the integrals of motion.

Any combination of integrals of motion is also an integral. One may therefore choose three independent combinations of H, I_2 and I_3 such that the orbit classification diagram becomes

simple to draw. All such diagrams are equivalent. We shall see in Section 9 that the simplest classification is obtained in terms of the three action integrals.

The orbital structure that we have derived in this section depends on the form of the function $G(\tau)$ which – via (22) and (20) – defines the potential. It is not difficult to show that the orbital structure is the same for all functions $G(\tau)$ that are smooth, monotonically decreasing with increasing τ. Furthermore, at $\tau=-\gamma$, $G(\tau)$ should be finite, or diverge slower than $1/\tau+\gamma$. Similarly, at large values of τ, $G(\tau)$ should fall off slower than $1/\tau$. This means that the orbit classification presented here is valid for many Stäckel potentials, and not only for the perfect ellipsoid. In fact, *all centrally concentrated triaxial mass models that have a finite density in the centre and a Stäckel potential possess an orbital structure that is identical to that of the perfect ellipsoid*; it is summarized in Fig. 17.

6 Special cases

The orbital structure of the perfect ellipsoid simplifies for the various special cases that were introduced in Section 3.4, and studied further in Section 4.4.

6.1 PROLATE SPHEROID

For $a>b=c$ we have $\beta=\gamma$ and the Hamilton–Jacobi equation separates in oblate spheroidal coordinates (*cf.* Section 2.3). The classification of orbital shapes can be done by using the method decribed in Section 4.4. This is identical to taking $\nu=-\gamma=-\beta$ in all formulae, effective potential diagrams and classification diagrams of the general case.

Of the four families of general orbits that exist in the triaxial model, only two occur in the perfect prolate spheroid: inner and outer long axis tubes. There are no box orbits or short axis tubes. The effective potential curves for both cases are shown in Fig. 19. The cross-sections of the allowed volume with the meridional plane and with the equatorial plane are shown in Fig. 20.

Inner Long Axis Tubes occur for (Fig. 19a):

$$i_2<0, \qquad i_3>0, \qquad V_{\rm eff}(\mu_0)<E<0, \tag{101}$$

where μ_0 is the value of μ for which $V_{\rm eff}$ reaches a minimum. The allowed values of λ and μ are (Fig. 20a)

$$\mu_{\rm min}\leq\mu\leq\mu_{\rm max}, \qquad -\alpha\leq\lambda\leq\lambda_{\rm max}. \tag{102}$$

The orbit crosses the $\tilde{z}$-axis inside the foci, i.e. within the focal circle in the equatorial plane.

Outer Long Axis Tubes occur for values of the integrals that satisfy (Fig. 19b)

$$i_2>0, \qquad i_3>0, \qquad V_{\rm eff}(\lambda_0)<E<0, \tag{103}$$

where λ_0 is the value of λ where $V_{\rm eff}$ reaches its minimum. The allowed values of λ and μ are (Fig. 20b):

$$\mu_{\rm min}\leq\mu\leq-\alpha, \qquad \lambda_{\rm min}\leq\lambda\leq\lambda_{\rm max}. \tag{104}$$

The orbit crosses the $\tilde{z}$-axis outside the foci, so it remains outside the focal circle in the equatorial plane.

In each of the above cases there are no turning points in χ, since $i_3>0$. Thus, a given tube orbit has a definite sense of rotation around the x-axis. Both clockwise and anticlockwise motion around the long axis may occur, filling the same volume.

For $i_3=\frac{1}{2}I_x^2=0$ the orbits are constrained to remain in a meridional plane since $\dot{\chi}=0$ and hence

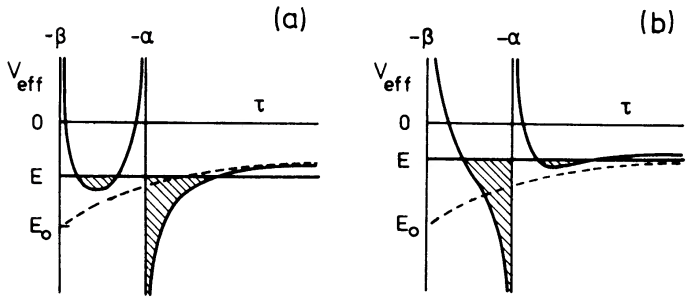

Figure 19. Effective potential curves for the two families of general orbits in the perfect prolate spheroid. The dashed curve is $-G(\tau)$. (a) Inner long axis tube; (b) outer long axis tube.

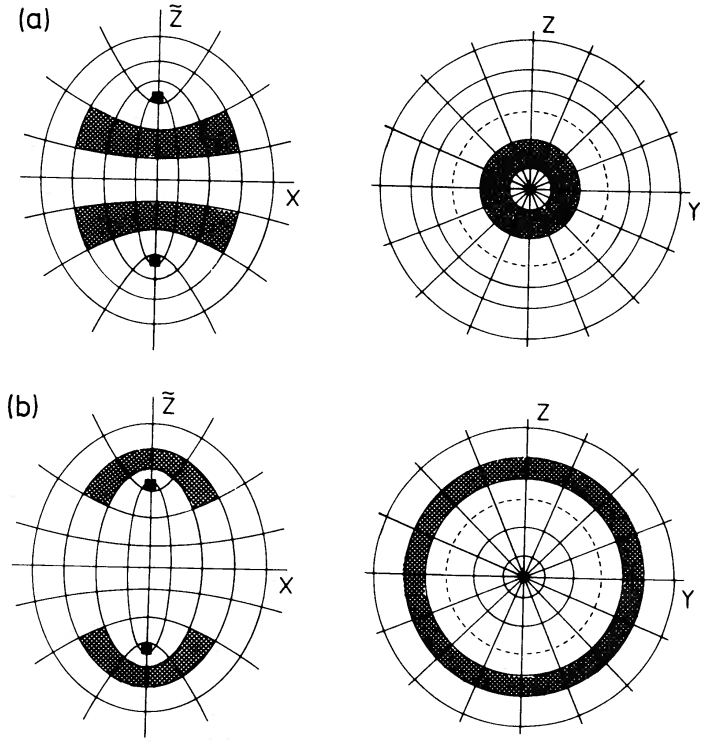

Figure 20. Cross-section with a meridional plane and with the equatorial plane of the volumes allowed to the two general orbits by the values of the integrals of motion. The focal circle is dashed. The filled squares are the foci. (a) Inner long axis tube; (b) outer long axis tube.

χ=constant. Motion in this plane is equivalent to motion in the (x, y)-plane of the triaxial model. The detailed orbit classification in this plane can therefore be taken verbatim from Section 5.2. The relevant effective potential curves are given in Fig. 9; since $\gamma=\beta$, we can ignore the ν-part of the diagrams. A small change in $i_3=\frac{1}{2}l_x^2$ will make $\dot{\chi}$ zero and cause an orbit to leave the meridional plane and circulate around the x-axis. Thus, all orbits in this plane are unstable to perturbations out of it. The only exception is the x-axis oscillation. The orbit classification diagram of E versus i_2 for the meridional plane is equivalent to Fig 10, except for the perpendicular instability just mentioned.

All orbits in the equatorial plane have $i_2=0$. Motion in this plane may be compared with that in the (y, z)-plane of the triaxial model described in Section 5.4. Effective potential curves follow from those given in Fig. 14, where again we can ignore the ν-part. We note that the three kinds of loops that occur in the (y, z)-plane of the triaxial model all have their counterparts in the prolate model. This is not true for butterflies. Neither stable nor unstable butterflies exist in the

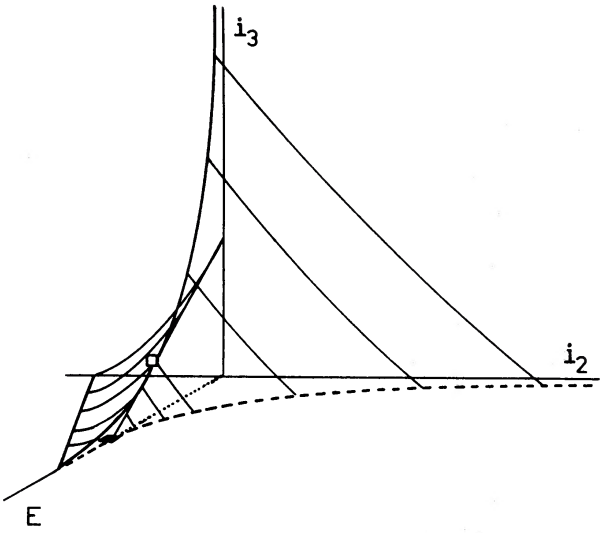

Figure 21. Three-dimensional classification of orbits in the perfect prolate spheroid in terms of the integrals E, i_2 and $i_3=\frac{1}{2}l_x^2$. Each point within the volume shown corresponds to a bound orbit. Dashed and dotted lines have the same meaning as in Fig. 13.

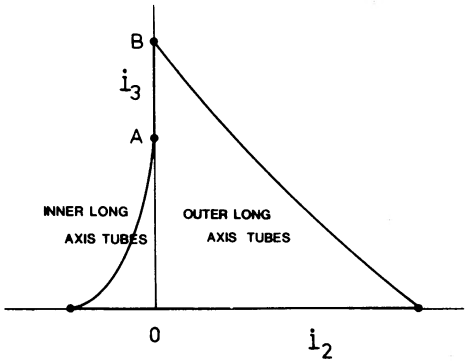

Figure 22. Cross-section of Fig. 21 with a plane of constant $E(E_4<E<0)$.

equatorial plane of the perfect prolate spheroid. The orbit classification diagram for the equatorial plane – E versus $i_3=\frac{1}{2}l_x^2$ – follows from Fig. 16, by taking $\beta=\gamma$.

The three-dimensional volume in (E, i_2, i_3)-space that corresponds to all bound orbits in the perfect prolate spheroid is shown in Fig. 21. Fig. 22 is a cross-section with a plane of constant E, where $E_4<E<0$. For $E_2<E<E_4$ the point B lies below the point A on the i_3-axis. The volume is limited by the planes $E=0$, $i_3=0$ and a curved surface, the parametric representation of which is given by equation (100), provided we take $\nu=-\gamma=-\beta$. Values of the integrals of motion on this surface give rise to infinitesimally thin inner and outer long axis tubes. The former are inner long axis tubes collapsed in the μ-direction, the latter are outer long axis tubes collapsed in the direction of λ (see Figs 19 and 20).

Fig. 21 may be compared with Fig. 17. Taking $\beta=\gamma$ is equivalent to merging the plane $E=V_{\rm eff}(-\beta)$ with that of $i_2=0$ in that figure. The result is Fig. 21; all boxes and short axis tubes disappear. We remark that of the five special energies E_0, E_1, E_2, E_3 and E_4 that occur in the general case, only three are left. For $\beta=\gamma$ one finds $E_1=E_0$ and $E_3=E_2$.

6.2 OBLATE SPHEROID

For $a=b>c$ we have $\alpha=\beta$ and the Hamilton–Jacobi equation separates in prolate spheroidal coordinates (*cf.* Section 2.3). The classification of orbital shapes (Section 4.4) is identical to

taking $\mu=-\beta=-\alpha$ in all formulae, effective potential diagrams, and classification diagrams of Section 5.

Of the four families of general orbits that exist in the triaxial model, only one exists in the perfect oblate spheroid. All general orbits are short axis tubes. No box orbits, inner or outer long axis tubes occur.

The *short axis tubes* exist for values of the integrals of motion that satisfy (Fig. 23)

$$i_2>0, \qquad i_3>0, \qquad V_{\rm eff}(\lambda_0)<E<0, \tag{105}$$

where λ_0 is the value of λ for which $V_{\rm eff}$ reaches a minimum. The allowed values of λ and ν are

$$-\gamma\leq\nu\leq\nu_{\max}, \qquad \lambda_{\min}\leq\lambda\leq\lambda_{\max}. \tag{106}$$

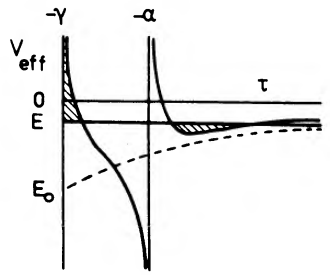

Figure 23. Effective potential curve for a short axis tube in the perfect oblate spheroid. The dashed curve is $-G(\tau)$.

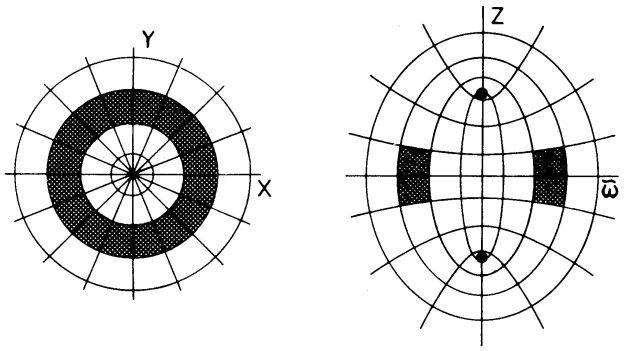

Figure 24. Cross-section with a meridional plane and with the equatorial plane of the volume allowed to a short axis tube by the values of the integrals of motion. The filled circles are the foci.

Cross-sections of the allowed volume defined by (106) with the equatorial and meridional planes are shown in Fig. 24. A given short axis tube has a definite sense of rotation around the z-axis ($\dot\phi>0$). Both clockwise and anticlockwise tubes may occur, filling the same volume.

For $i_2=\frac{1}{2}l_z^2=0$ the orbits lie in a meridional plane. Motion in this plane may be compared with that in the (y, z)-plane of the triaxial model discussed in Section 5.4. However, in the present case all orbits in this plane, with the exception of the x-axis oscillation, are unstable to perturbations out of this plane. Any change in i_2 will cause the orbits to leave the plane $\phi=$constant and circulate around the z-axis. The classification diagram of E versus i_3 follows from Fig. 16 upon taking $\beta=\alpha$.

All orbits in the equatorial plane have $i_3=0$. The general orbits are loops, and are always stable. They are short axis tubes collapsed in the z-axis direction. At each radius there exists a circular orbit. The relation between E and i_2 for this orbit is given by equation (82). The classification diagram of E versus i_2 follows from Figs 10 or 13, upon taking $\beta=\alpha$.

The three-dimensional volume in (E, i_2, i_3)-space that corresponds to bound orbits in the perfect oblate spheroid is given in Fig. 25. A cross-section with a plane of constant E is shown in Fig. 26. This volume is limited by the planes $E=0$, $i_3=0$, $i_2=0$ and a curved surface for which the

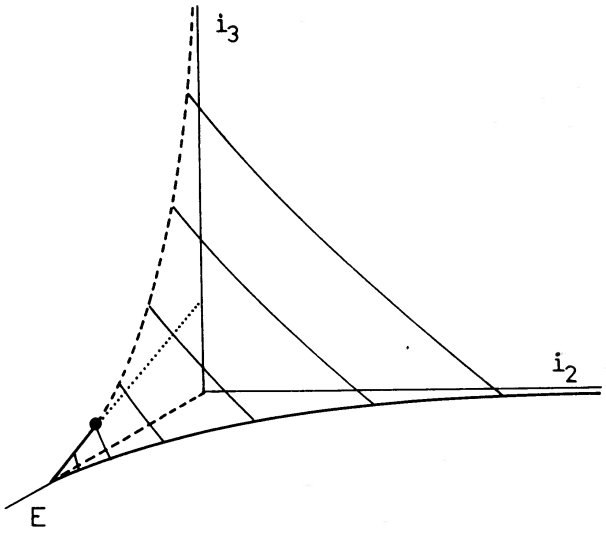

Figure 25. Three-dimensional classification of orbits in the perfect oblate spheroid in terms of the integrals E, $i_2=\frac{1}{2}l_z^2$ and i_3. Each point within the volume shown corresponds to a bound orbit. Dashed and dotted lines have the same meaning as in Fig. 13.

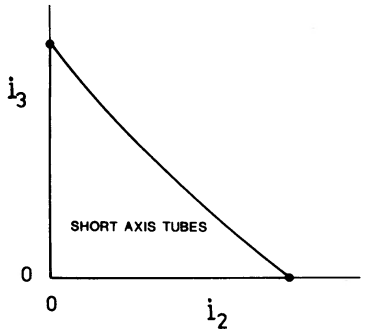

Figure 26. Cross-section of Fig. 25 with a plane of constant E.

parametric representation is given in equation (100), where we have to take $\mu=-\beta=-\alpha$. Values of the integrals of motion on this surface give rise to infinitesimally thin short axis tubes, i.e. short axis tubes that are collapsed in the λ-direction.

Fig. 25 can be obtained from the similar classification diagram for the general case, Fig. 17, by taking $\beta=\alpha$. This is equivalent to merging the plane $E=V_{\rm eff}(-\beta)$ with that of $i_3=0$ in that figure. This causes all boxes and inner and outer long axis tubes to disappear. Also, of the five energies $E_0, \ldots, E_4$ that play a special role in Section 5, only two remain, since $E_0=E_2$ and $E_1=E_3=E_4$.

6.3 SPHERE

For $a=b=c$ we have $\alpha=\beta=\gamma$, and the Hamilton–Jacobi equation separates in spherical coordinates. The classification of orbital shapes can be done as decribed in Section 4.4. The results are identical to those obtained by taking $\mu=\nu=-\gamma=-\beta=-\alpha$ in all formulae, effective potential diagrams and classification diagrams of Section 5. Equivalently, one can take $\nu=-\gamma=-\alpha$ in the results for the oblate case, presented in the above.

From the conservation of the total angular momentum it follows that every orbit lies in a plane through the origin. In each such plane the general orbits are loops, as inspection of $V_{\rm eff}(\lambda)$ shows.

At every radius $r=r_0=\sqrt{\lambda_0+\alpha}$, there exists a circular orbit. The parametric relation between $i_2+i_3=\frac{1}{2}l^2$ and E for this orbit is

$$i_2+i_3=-(\lambda_0+\alpha)^2G'(\lambda_0), \qquad E=-G(\lambda_0)-(\lambda_0+\alpha)G'(\lambda_0). \tag{107}$$

For $i_2+i_3=0$ each orbit is a straight line through the origin (ϕ and θ both constant). This orbit is unstable. Any small change in l^2 will cause the orbit to circulate about the centre. Evidently, the motion in each plane through the origin is equivalent to that in the equatorial plane of the perfect oblate spheroid, except that here all orbits are marginally unstable against perpendicular perturbations. A small change in the direction of **L** changes the inclination of the orbital plane.

The three-dimensional orbit classification diagram for the sphere is similar to Fig. 25, if we merge the dotted line in that figure with the axis $i_2=i_3=0$.

For $a=b=c=0$ the 'perfect sphere' is a point mass M at the origin. Taking the limit $a\rightarrow 0$ in equation (28) produces $V=-GM/r$, as it should. Motion in such a Keplerian potential is described in every textbook on classical mechanics (e.g. Goldstein 1980, §3).

6.4 ELLIPTIC DISC

As the potential of the perfect elliptic disc is of Stäckel form in ellipsoidal coordinates (λ,μ,ν), it admits the three integrals of motion H, I_2 and I_3 defined in equations (47)–(49). For $\gamma=0$ we find

$$I_2=\alpha H+J+\frac{K}{\alpha}, \qquad I_3=-\frac{K}{\alpha}. \tag{108}$$

The equations of motion are given in (51), where we have to take $\gamma=0$ and use the appropriate form of $G(\tau)$. Motion can be analysed in exactly the same way as was described in Section 4.3 for the general case.

A comparison of the effective potential curves with lines of constant energy for all values of E, i_2 and i_3 reveals that the three-dimensional orbits in the potential of the perfect elliptic disc have exactly the same variety of shapes as the orbits in the triaxial model. The fact that in the present case $G(\tau)$ diverges proportionally to $1/\sqrt{\tau}$ for $\tau\rightarrow -\gamma=0$, whereas in the general case $G(-\gamma)$ is finite, does not change the orbit classification. The behaviour of $V_{\rm eff}$ at $\tau=-\gamma$ is in both cases determined by the term $i_3/(\tau+\gamma)$. Thus, the detailed orbit classification, as well as the relations between the integrals of motion for all orbits, can be taken verbatim from Section 5, by taking $\gamma=0$ in all equations.

In particular, the bound orbits that remain *in* the perfect elliptic disc are identical to those found in the (x,y)-plane of the triaxial model. The classification diagram of E versus i_2 is similar to Fig. 10. The only difference is the precise form of the relation between E and i_2 for the elliptic closed orbits, which is due to the difference between the functions $G(\tau)$ in the two cases.

6.5 KUZMIN'S DISC

Just as the classification of the orbital shapes in the potential of the perfect elliptic disc turned out to be identical to that in the triaxial model, we find that the orbit classification for motion in the potential (35) is identical to that presented in Section 6.2 for the perfect oblate spheroid.

The volumes allowed to the three-dimensional orbits are the same as for the perfect oblate spheroid, but for the case at hand we also know that these orbits must consist of pieces of Keplerian ellipses around the appropriate foci (*cf.* Section 4.4). An obvious example is the closed elliptic orbit over the pole.

6.6 NEEDLE

The needle has the same relation to the perfect prolate speroid as Kuzmin's disc has to the perfect oblate spheroid. Motion in the potential of this perfect cigar is equivalent to that in the perfect prolate spheroid. The orbit classification can be taken verbatim from Section 6.1, by writing $\beta=\gamma=0$ in all equations. The only orbits that remain *in* the needle are the x-axis oscillations.

Finally, we remark that the orbit classification for the special cases of the perfect ellipsoid is valid for a wide class of models with Stäckel potentials.

7 The self-consistent problem

7.1 THE DISTRIBUTION FUNCTION

A dynamical model for a collisionless stellar system such as an elliptical galaxy is determined completely by a specification of the phase-space distribution function, f, which gives the distribution of stars over position and momentum. Clearly, $f\geq 0$, and it must satisfy the collisionless Boltzmann equation. If the stellar system is in a steady state, f does not depend on time explicitly, and $\partial f/\partial t=0$. The problem of finding a distribution function for a stellar system is the fundamental problem of stellar dynamics (Chandrasekhar 1942), and is often referred to as the *self-consistent problem*.

The density ϱ of the system is related to the integral of f over the momenta. In ellipsoidal coordinates we have

$$\left\{\int_{p_\lambda^2\geq 0}\int_{p_\mu^2\geq 0}\int_{p_\nu^2\geq 0} f(\lambda,\mu,\nu;p_\lambda,p_\mu,p_\nu)\,dp_\lambda\,dp_\mu\,dp_\nu\right\}d\lambda\,d\mu\,d\nu=\varrho(\lambda,\mu,\nu)\,PQR\,d\lambda\,d\mu\,d\nu. \tag{109}$$

Here we have used the fact that the volume element $dx\,dy\,dz$ equals $PQR\,d\lambda\,d\mu\,d\nu$ [*cf.* (10)]. For density distributions with a gravitational potential of Stäckel form all orbits have three exact isolating integrals of motion. Jeans' theorem applies; it states that in this case f is a function of the phase-space coordinates only through the isolating integrals, i.e. $f=f(H, I_2, I_3)$ (Jeans 1915; Lynden-Bell 1962b). Thus, we may write

$$\varrho(\lambda,\mu,\nu)=\frac{1}{PQR}\int\int\int f(H,I_2,I_3)\left|\frac{\partial(p_\lambda,p_\mu,p_\nu)}{\partial(H,I_2,I_3)}\right|dH\,dI_2\,dI_3. \tag{110}$$

With the aid of the equations of motion (51) we find

$$\varrho(\lambda,\mu,\nu)=C(\lambda,\mu,\nu)\int\int\int\frac{f(H,I_2,I_3)\,dH\,dI_2\,dI_3}{\sqrt{N(\lambda)}\sqrt{N(\mu)}\sqrt{-N(\nu)}} \tag{111}$$

where

$$N(\tau)=H-\frac{I_2}{\tau+\alpha}-\frac{I_3}{\tau+\gamma}+G(\tau) \tag{112}$$

and

$$C(\lambda,\mu,\nu)=\frac{(\gamma-\alpha)}{2\sqrt{2}\sqrt{(\lambda+\alpha)(\mu+\alpha)(\nu+\alpha)}\sqrt{(\lambda+\gamma)(\mu+\gamma)(\nu+\gamma)}}. \tag{113}$$

For given (λ, μ, ν), the integration in (111) is over all values of H, I_2 and I_3 for which the expressions under the square roots are non-negative.

Two main approaches towards the solution of the self-consistent problem for mass models with separable potentials may be identified. In the first method, one specifies a function $f(H, I_2, I_3)$

and calculates $\varrho(\lambda, \mu, \nu)$ by means of (111). This f is the distribution function of a self-gravitating stellar system in equilibrium only if the potential of $\varrho(\lambda, \mu, \nu)$ that follows from Poisson's equation ($\nabla^2 V = 4\pi G\varrho$) is identical to the potential defined by $G(\tau)$ in the right-hand side of (111). The alternative approach is to specify $\varrho(\lambda, \mu, \nu)$ – and hence $G(\tau)$ – and regard (111) as an integral equation for $f(H, I_2, I_3)$. One may then attempt to solve this equation by direct inversion, or by means of a (numerical) approximation technique.

7.2 INDIVIDUAL ORBIT DENSITIES

For a single orbit with $H=E$, $I_2=i_2$ and $I_3=i_3$ the density is given by (110) or (111) with $f=f(H, I_2, I_3)=\delta(H-E)\delta(I_2-i_2)\delta(I_3-i_3)$. The mass in the element $dx\,dy\,dz$ is given by $\varrho_{\rm orb} PQR\,d\lambda\,d\mu\,d\nu$ with

$$\varrho_{\rm orb}(\lambda, \mu, \nu; E, i_2, i_3) = \left| \frac{\partial(p_\lambda, p_\mu, p_\nu)}{\partial(H, I_2, I_3)} \right|_{(H=E,\, I_2=i_2,\, I_3=i_3)}$$

$$= \frac{C(\lambda, \mu, \nu)}{\sqrt{-N(\lambda)N(\mu)N(\nu)}}, \tag{114}$$

where $C(\lambda, \mu, \nu)$ is given in (113), and $N(\tau)$ in (112). The expression (114) is valid for all values of λ, μ and ν for which $p_\lambda^2 \geq 0$, $p_\mu^2 \geq 0$ and $p_\nu^2 \geq 0$, so that the square roots are well defined [*cf.* (51)]. For all other points (λ, μ, ν) the orbit density $\varrho_{\rm orb}$ is zero. Clearly, $\varrho_{\rm orb}$ can be simply evaluated; *no (numerical) integration of the equations of motion is required.*

We remark that, if one is interested in the mass of the element $d\lambda\,d\mu\,d\nu$, the expression (114) has to be multiplied by PQR.

The orbital densities should be interpreted as follows. In general, the frequencies of the motions in each of the three coordinates λ, μ and ν are incommensurable and $\varrho_{\rm orb}$ is the time-averaged density of the orbit as it fills the whole area allowed by the integrals. When two of the frequencies are commensurable, the phase difference between the corresponding oscillations is a fourth independent isolating integral of motion. The orbit breaks up in a continuum of semi-periodic orbits parametrized by this fourth integral. In this case $\varrho_{\rm orb}$ applies to this whole collection of orbits. Similarly, when all three frequencies are commensurable, there are two isolating integrals in addition to H, I_2 and I_3. The orbit is now a two-parameter family of periodic orbits. Again, $\varrho_{\rm orb}$ applies to this whole family.

For orbits in one of the principal planes expression (114) simplifies. For an orbit in the (x, y)-plane the mass in the element $dx\,dy$ is $\Sigma_{\rm orb}\,dx\,dy$, where the surface density $\Sigma_{\rm orb}$ is given by

$$\Sigma_{\rm orb}(\lambda, \mu; E, i_2) = \frac{PQ}{\lambda-\mu} \times \frac{1}{p_\lambda p_\mu}$$

$$= \frac{1}{2\sqrt{(\lambda+\alpha)(\mu+\alpha)}\sqrt{E - i_2/(\lambda+\alpha) + G(\lambda)}\sqrt{E - i_2/(\mu+\alpha) + G(\mu)}}. \tag{115}$$

Similar expressions can be written down for the (x, z)- and (y, z)-planes.

For the simple periodic orbits $\varrho_{\rm orb}$ becomes a line density $\xi_{\rm orb}$. For example, for the x-axis orbit the mass in the element dx is $\xi_{\rm orb} P d\lambda$ with

$$\xi_{\rm orb}(\lambda; E) = \frac{1}{2\sqrt{(\lambda+\alpha)}\,p_\lambda}, \tag{116}$$

where p_λ is given in (73), and $i_2 = i_2(E)$ given in (75).

In Fig. 27 we show some examples of densities of strict two-dimensional orbits in the $(x,$

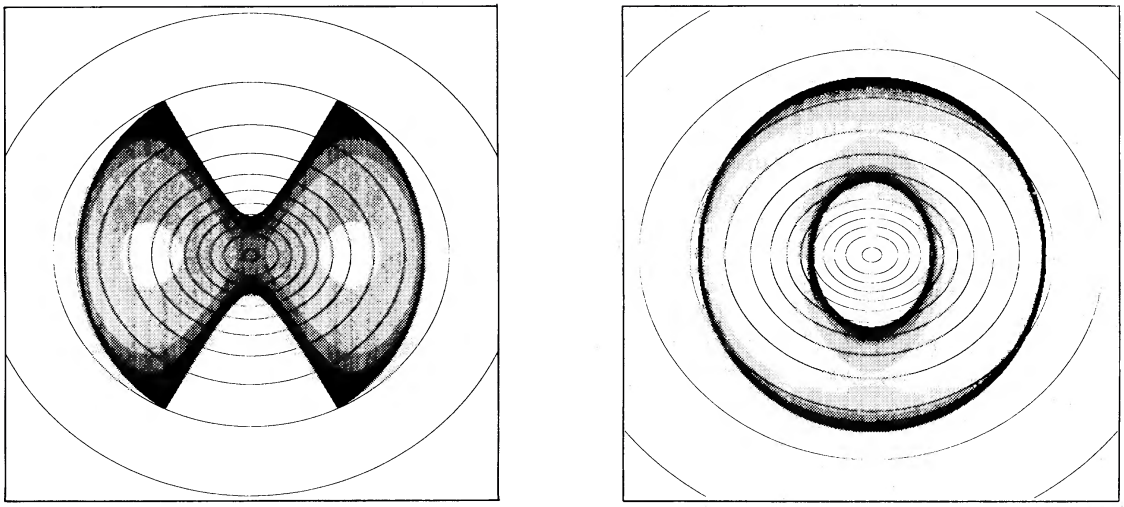

(a) (b)

Figure 27. Densities of two orbits in the (x, y)-plane. The curves are contours of constant potential energy. A darker shading indicates a higher density. (a) Butterfly; (b) loop.

y)-plane of the perfect ellipsoid, computed with equation (115). The density is highest at the boundary of the area filled by the orbit. The star spends most of its time where the velocity is lowest, so the density peaks at the turning points, where p_λ and p_μ are zero (or both, at the four corners of a butterfly). We remark that although this means that $\varrho_{\rm orb}$ is infinite at the orbital boundaries, the integral of $\varrho_{\rm orb}$ over a finite region is always finite, even if this region contains the boundaries.

It follows from the above that (111) can be rewritten as

$$\varrho(\lambda,\mu,\nu)=\int\int\int f(H,I_2,I_3)\varrho_{\rm orb}(\lambda,\mu,\nu;H,I_2,I_3)\,dH\,dI_2\,dI_3. \tag{117}$$

This shows explicitly that the solution of the self-consistent problem is equivalent to populating individual orbits in such a way that the orbital densities add up to the total mass density.

Various numerical techniques for the reconstruction of a given mass model from the orbits in it have been developed recently (Schwarzschild 1979; Newton & Binney 1984). For general systems, such as the Schwarzschild ellipsoid, the orbital densities have to be calculated by numerical integration of the equations of motion and subsequent averaging of the time spent by each orbit in a large number of cells. It is evident that the same methods can be applied to the construction of self-consistent models with Stäckel potentials. In this case, however, laborious numerical integrations can be avoided, since the orbital densities $\varrho_{\rm orb}$ can be written down explicitly.

Finally, we remark that the special forms of the fundamental integral equation (111) for the axisymmetric, spherical, disc and needle limits can be deduced easily. The appropriate expressions for the individual orbit densities follow immediately.

8 Actions and frequencies

We have obtained a complete classification of orbits in a Stäckel potential without integration of the equations of motion. In what follows we introduce *action-angle* variables, which in many respects are the natural variables for a description of the motion. It will be seen in Section 9 that the orbit classification of Section 5 becomes particularly transparent in these variables.

8.1 ACTIONS AND ANGLES

The definition of action-angle variables for completely separable Hamiltonian systems has been discussed *in extenso*, e.g. by Goldstein (1980) in the context of Hamilton–Jacobi theory. We briefly outline the procedure for the case of motion separable in ellipsoidal coordinates. The results apply to all Stäckel potentials, and not only to the particular case of motion in the perfect ellipsoid.

We define *action variables* J_λ, J_μ and J_ν by

$$J_\tau = \frac{1}{2\pi}\oint \frac{\partial W_\tau}{\partial \tau}\, d\tau = \frac{1}{2\pi}\oint p_\tau\, d\tau, \qquad \tau=\lambda,\mu,\nu, \tag{118}$$

where $p_\tau = p_\tau(\tau; E, i_2, i_3)$ is given in (51), and the integration is over all values of τ for which $p_\tau^2 \geq 0$. For an orbit with $H=E$, $I_2=i_2$ and $I_3=i_3$ we find

$$J_\tau = J_\tau(E, i_2, i_3). \tag{119}$$

This confirms that the actions are integrals of motion. The orbit classification can therefore equally well be performed in terms of J_λ, J_μ and J_ν.

Upon inversion of the equations (119) we find expressions for E, i_2 and i_3 in terms of the actions. This means that we can write Hamilton's characteristic function W, given in (41), as

$$W = \sum_\tau W_\tau(\tau; J_\lambda, J_\mu, J_\nu). \tag{120}$$

The *angle variables* θ_τ, which are canonically conjugate to the actions, then follow from

$$\theta_\tau = \frac{\partial W}{\partial J_\tau} = \sum_{\tau'} \frac{\partial W_{\tau'}(\tau; J_\lambda, J_\mu, J_\nu)}{\partial J_\tau}. \tag{121}$$

The equations of motion in action-angle variables have a simple form. Since $H = H(J_\lambda, J_\mu, J_\nu)$, Hamilton's equations are

$$\dot{J}_\tau = 0, \qquad \dot{\theta}_\tau = \frac{\partial H}{\partial J_\tau} = \omega_\tau. \tag{122}$$

The solution is

$$J_\tau = J_\tau(0), \qquad \theta_\tau = \omega_\tau t + \theta_\tau(0), \qquad \tau=\lambda,\mu,\nu, \tag{123}$$

where $J_\tau(0)$ and $\theta_\tau(0)$ are constants determined by the initial conditions, and t denotes time. Equations (123) represent the complete solution of the equations of motion in a Stäckel potential (20).

The quantities $\omega_\tau = \partial H/\partial J_t$ are the *frequencies* of the motions in each of the coordinates. If all three frequencies are incommensurable, the orbit completely fills the volume allowed to it by the values of the integrals of motion, i.e. the region where p_λ^2, p_μ^2 and p_ν^2 are non-negative. If there is one relation of the form $l\omega_\lambda + m\omega_\mu + n\omega_\nu = 0$, where l, m and n are integers, an appropriate phase difference is a fourth isolating integral of motion. The orbit now breaks up in a continuum of orbits, each of which fills a two-dimensional region in the allowed volume. If two such relations exist between the frequencies, so that all three are commensurable, two independent phase differences are conserved, and the orbit is a two-parameter family of periodic orbits (Lissajous figures) that together fill the allowed volume.

8.2 FREQUENCIES

The calculation of the fundamental orbital frequencies ω_λ, ω_μ and ω_ν via inversion of (119) and subsequent differentiation, is cumbersome. Fortunately, the inversion may be avoided (see, e.g. van de Hulst 1962). We may write

$$\begin{aligned}
\frac{\partial H}{\partial H} &= \omega_\lambda \frac{\partial J_\lambda}{\partial H} + \omega_\mu \frac{\partial J_\mu}{\partial H} + \omega_\nu \frac{\partial J_\nu}{\partial H} = 1, \\
\frac{\partial H}{\partial I_2} &= \omega_\lambda \frac{\partial J_\lambda}{\partial I_2} + \omega_\mu \frac{\partial J_\mu}{\partial I_2} + \omega_\nu \frac{\partial J_\nu}{\partial I_2} = 0, \\
\frac{\partial H}{\partial I_3} &= \omega_\lambda \frac{\partial J_\lambda}{\partial I_3} + \omega_\mu \frac{\partial J_\mu}{\partial I_3} + \omega_\nu \frac{\partial J_\nu}{\partial I_3} = 0.
\end{aligned} \tag{124}$$

Then

$$\omega_\lambda = \frac{1}{\Delta} \frac{\partial(J_\mu, J_\nu)}{\partial(I_2, I_3)}, \qquad \omega_\mu = \frac{1}{\Delta} \frac{\partial(J_\nu, J_\lambda)}{\partial(I_2, I_3)}, \qquad \omega_\nu = \frac{1}{\Delta} \frac{\partial(J_\lambda, J_\mu)}{\partial(I_2, I_3)}, \tag{125}$$

where we have written

$$\Delta = \frac{\partial(J_\lambda, J_\mu, J_\nu)}{\partial(H, I_2, I_3)}. \tag{126}$$

The partial derivatives that occur in the expressions (125) and (126) can be evaluated by differentiating under the integrals (118)

$$\begin{aligned}
\frac{\partial J_\tau}{\partial H} &= \frac{1}{8\pi} \oint \frac{d\tau}{(\tau+\beta) p_\tau}, \\
\frac{\partial J_\tau}{\partial I_2} &= -\frac{1}{8\pi} \oint \frac{d\tau}{(\tau+\alpha)(\tau+\beta) p_\tau}, \\
\frac{\partial J_\tau}{\partial I_3} &= -\frac{1}{8\pi} \oint \frac{d\tau}{(\tau+\beta)(\tau+\gamma) p_\tau}.
\end{aligned} \tag{127}$$

The above formulae allow a calculation of the actions J_τ and frequencies ω_τ without the necessity of completely solving the equations of motion. For a given Stäckel potential, e.g. specified by the function $G(\tau)$, and given values E, i_2 and i_3 of the integrals of motion, the actions follow from (51) and (118), and the frequencies can be computed by means of (125)–(127). In practice, the integrations that are needed in (118) and (127) will often have to be performed by numerical means.

8.3 TWO-DIMENSIONAL MOTION

Motion in the (x, y)-plane of the perfect ellipsoid is strictly two-dimensional, and separable in elliptic coordinates (λ, μ). For subsequent use, we briefly consider how the expressions derived in the above simplify.

We have seen in Section 5.2 that in this case $\nu = -\gamma$ and $i_3 = 0$;. In general $p_\nu \neq 0$ for $\nu = -\gamma$, so

that we find [*cf.* (127)]

$$J_\nu=0, \qquad \frac{\partial J_\nu}{\partial H}=0, \qquad \frac{\partial J_\nu}{\partial I_2}=0. \tag{128}$$

Substitution of these expressions in the formulae for ω_λ and ω_μ then produces

$$\omega_\lambda=\frac{1}{D}\frac{\partial J_\mu}{\partial I_2}, \qquad \omega_\mu=-\frac{1}{D}\frac{\partial J_\lambda}{\partial I_2}, \tag{129}$$

with

$$D=\frac{\partial(J_\lambda, J_\mu)}{\partial(H, I_2)}=\frac{\partial J_\lambda}{\partial H}\frac{\partial J_\mu}{\partial I_2}-\frac{\partial J_\lambda}{\partial I_2}\frac{\partial J_\mu}{\partial H}, \tag{130}$$

and the partial derivatives of J_τ are given in (127). We note that

$$\frac{\omega_\lambda}{\omega_\mu}=-\frac{\partial J_\mu}{\partial I_2}\Big/\frac{\partial J_\lambda}{\partial I_2}=-\left(\frac{\partial J_\mu}{\partial J_\lambda}\right)_{(H=E)}. \tag{131}$$

Here J_λ and J_μ are defined as in (118), but p_τ is given by (73).

We remark that the separation of the Hamilton–Jacobi equation, and the introduction of action-angle variables, for the case of two-dimensional separable motion in elliptic coordinates has been discussed in many textbooks, in the context of the famous problem of motion in the field of force of two fixed centres of attraction (e.g. Jacobi 1866; Charlier 1927; Landau & Lifshitz 1976).

9 Orbit classification in action space

9.1 ACTION DIAGRAMS

The actions J_λ, J_μ and J_ν for the orbits in the perfect ellipsoid are

$$J_\lambda=\frac{2}{\pi}\int_{\lambda_{\min}}^{\lambda_{\max}} p_\lambda\, d\lambda, \qquad J_\mu=\frac{2}{\pi}\int_{\mu_{\min}}^{\mu_{\max}} p_\mu\, d\mu, \qquad J_\nu=\frac{2}{\pi}\int_{-\gamma}^{\nu_{\max}} p_\nu\, d\nu, \tag{132}$$

where the p_τ are given in (51). For a *box orbit* we have $\lambda_{\min}=-\alpha$ and $\mu_{\min}=-\beta$; for an *inner long axis tube* $\lambda_{\min}=-\alpha$ and $\nu_{\max}=-\beta$; for an *outer long axis tube* $\mu_{\max}=-\alpha$ and $\nu_{\max}=-\beta$, and for a *short axis tube* $\mu_{\max}=-\alpha$ and $\mu_{\min}=-\beta$. The other integration limits follow from solving $p_\tau=0$ ($\tau=\lambda$, μ or ν). The actions for the various limiting and transitional orbits that we encountered in Section 5 can be found by taking the appropriate limits in (132). These can be deduced easily from the effective potential diagrams of Section 5.

For the evaluation of the loop integrals in (118) we have taken in (132) *four* times the integrals from $\lambda_{\min}$ to $\lambda_{\max}$, from $\mu_{\min}$ to $\mu_{\max}$ and from $\nu_{\min}$ to $\nu_{\max}$. We do the same for the calculation of the frequencies ω_λ, ω_μ and ω_ν by means of (127). For a box orbit this choice covers one complete oscillation in all three variables. For the three kinds of tube orbits, however, the oscillations in two of the three coordinates are covered once, but the rotation in the remaining coordinate is covered *twice*. This ensures that the actions and frequencies are continuous across the transitions from one orbit family to another. The situation is analogous to that for the well-known case of the pendulum.

Since the actions are integrals of motion, we can represent the orbit classification of Section 5 by means of a three-dimensional *action-diagram*. The result is given in Fig. 28; it is equivalent to

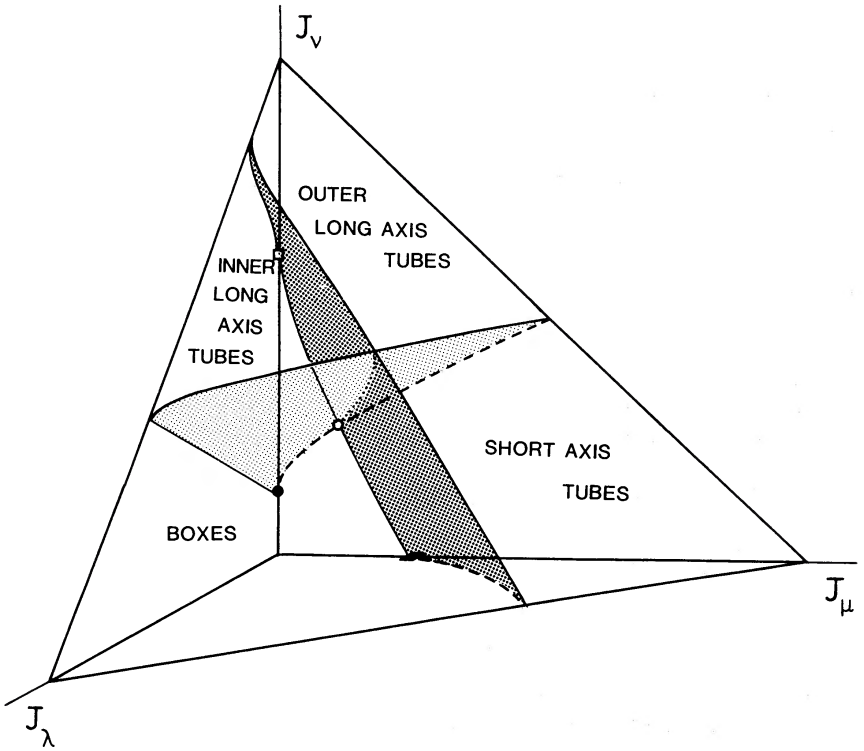

Figure 28. Action-diagram for the three-dimensional orbits in the perfect ellipsoid. The volumes occupied by the four families of general orbits are indicated. The locations of all limiting and transitional orbits are described in the text. The light and dark shaded surfaces correspond to the unstable orbits in the (x, z)- and (y, z)-plane, respectively. Dashed lines indicate simple periodic orbits that are unstable in one direction. The dotted line represents the z-axis orbits that are unstable in two directions. The filled and open circles and squares have the same meaning as in Section 5. The diagram is equivalent to Fig. 17.

Fig. 17. Each point in the diagram corresponds to an orbit. The tilted triangular surface is a surface of constant energy. Fig. 29 shows a detailed map of this surface, with the locations of the various limiting and transitional orbits indicated. It is directly comparable to Fig. 18.

Four distinct volumes may be recognized in Fig. 28, one for each family of general orbits. These volumes are separated by two curved surfaces. Values of the actions on these surfaces correspond with orbits in the (x, z)- and (y, z)-planes that are unstable to perpendicular perturbations (i.e. to perturbations out of it). Box orbits and inner long axis tubes are separated by the unstable butterflies in the (x, z)-plane. The unstable loops in this plane divide the outer long axis tubes and the short axis tubes. The inner and outer long axis tubes are separated by the unstable loops in the (y, z)-plane; the unstable butterflies in that plane separate the short axis tubes from the boxes.

The orbits in the (x, y)-plane are all stable to perpendicular perturbations and have $J_\nu=0$, so that they correspond to the points in the (J_λ, J_μ)-plane (compare Fig. 30). The stable butterflies in the (x, z)-plane are located in the (J_λ, J_ν)-plane on the boundary of the volume allotted to boxes. The similar boundary in the (J_μ, J_ν)-plane is occupied by the stable butterflies in the (y, z)-plane. The inner stable loops in this plane lie also in the (J_μ, J_ν)-plane; they bound the volume of the inner long axis tubes. The outer stable loops in the (y, z)-plane form the boundary of the volume reserved for the outer long axis tubes in the (J_λ, J_ν)-plane. The remaining areas in the planes $J_\lambda=0$ and $J_\mu=0$ are occupied by the three varieties of infinitesimally thin tubes.

Finally, points on the axes in the action-diagram correspond to the stable simple periodic orbits. The x-axis orbits lie along the J_λ-axis. The stable y-axis orbits and the elliptic closed orbits in the (x, y)-plane together occupy the J_μ-axis. The J_ν-axis is reserved for the stable z-axis oscillations – up to the filled circle – and, at larger values of J_ν, for the elliptic closed orbits in the

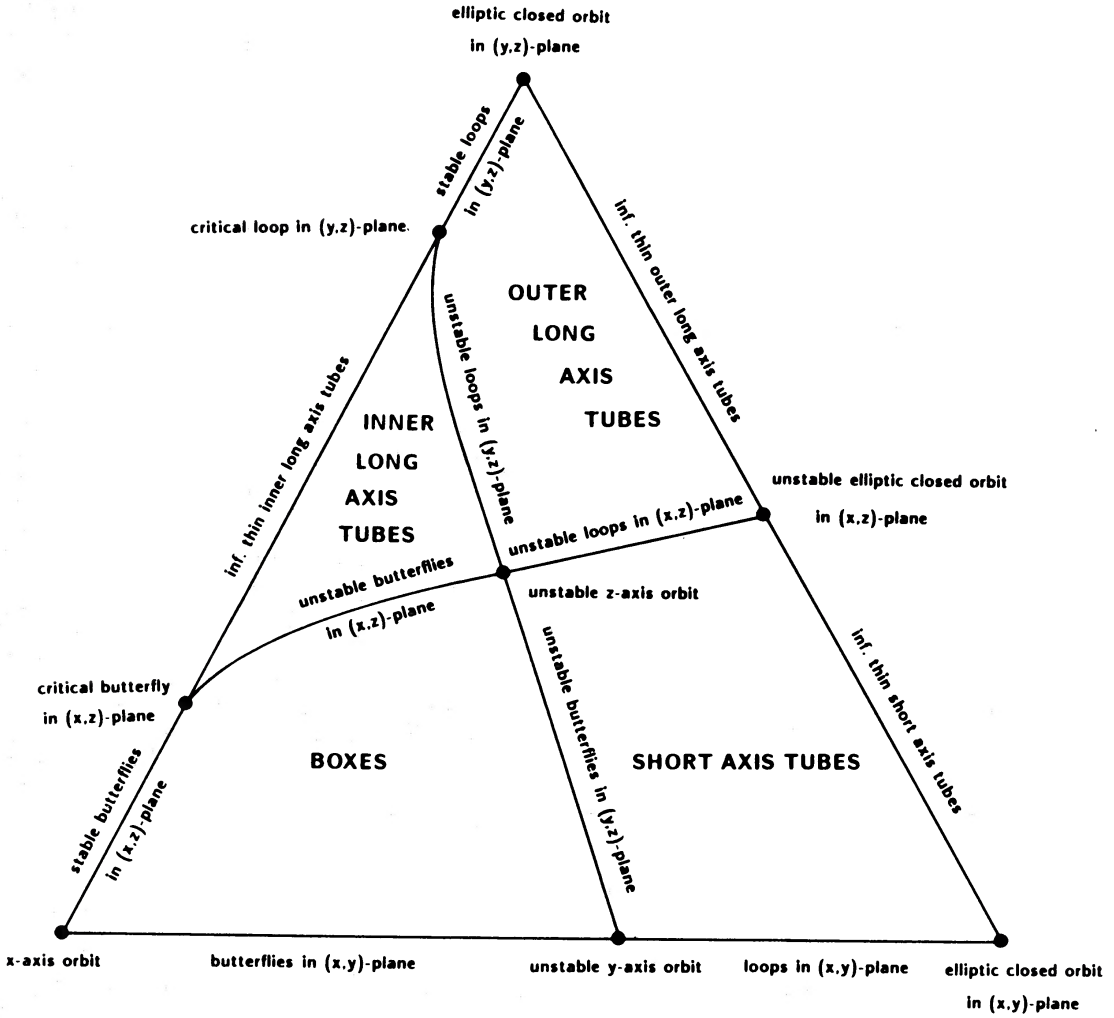

Figure 29. Cross-section of Fig. 28 with a plane of constant E. It may be compared with Fig. 18.

(y, z)-plane. The dashed line in the (J_μ, J_ν) plane indicates the z-axis orbits that are unstable to perturbations in the y-direction, and the unstable elliptic closed orbits in the (x, z)-plane. The two times unstable z-axis orbits occupy the dotted line, which is the curve of intersection of the two shaded surfaces in Fig. 28.

We emphasize that *this whole classification is valid* not only for the perfect ellipsoid, but *for all triaxial mass models that are relevant for elliptical galaxies and have a Stäckel potential.*

9.2 PHASE-SPACE VOLUMES

The phase-space volume occupied by a family of general orbits is a useful quantity. It is equal to $(2\pi)^3$ times the volume occupied by that family in the three-dimensional action space (e.g. Arnold 1978).

In order to obtain the actions for the tube orbits we have taken twice the loop integral in (118) for the rotating variable. One might therefore think that the volume in action-space allotted to tubes is too large by a factor of two. However, as Binney & Spergel (1984) point out, this is not the case, since each set of values $(J_\lambda, J_\mu, J_\nu)$ appropriate for a tube orbit represents in fact *two* orbits, one clockwise, and the other counter-clockwise.

The boundaries of the volumes occupied by the various orbit families are most easily written down in terms of the integrals H, I_2 and I_3. It is therefore convenient to evaluate the volume

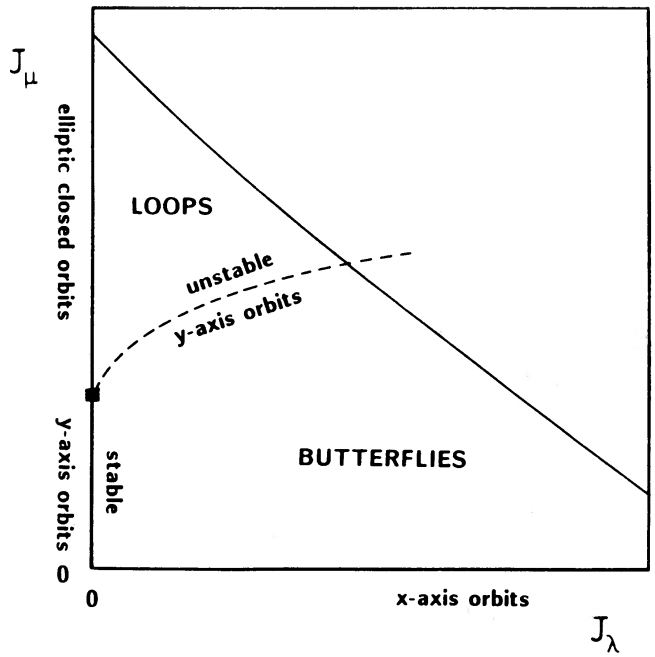

Figure 30. Action-diagram for the orbits in the (x, y)-plane of the perfect ellipsoid. The locations of the various orbit families are indicated. The filled square represents the y-axis orbit that just reaches the foci of the elliptic coordinates. The figure is equivalent to Fig. 10. The drawn curve is a line of constant energy.

integral in action-space as an integral in (H, I_2, I_3)-space, by writing

$$\int_{J_\lambda \geq 0}\int_{J_\mu \geq 0}\int_{J_\nu \geq 0} dJ_\lambda\, dJ_\mu\, dJ_\nu = \int\int\int |\Delta(H, I_2, I_3)|\, dH\, dI_2\, dI_3, \tag{133}$$

where the Jacobian $\Delta(H, I_2, I_3)$ was defined in (126). The integration over H is from E_0 [*cf.* (76)] to 0. The limits on the integration in the (I_2, I_3)-plane can be deduced from Fig. 18 and the equations (75), (82), (85), (86), (92) and (100).

9.3 TWO-DIMENSIONAL MOTION

It is of interest to take a more detailed look at the two-dimensional motion in the (x, y)-plane.

Fig. 31 shows the frequencies of the simple periodic orbits in the (x, y)-plane of the perfect ellipsoid as function of energy, calculated numerically for the axis ratios 1:⅝:½. It may be compared with the similar figure given by de Zeeuw & Merritt (1983) for Schwarzschild's (1979) non-separable triaxial potential.

Due to the non-axisymmetry of the potential in the (x, y)-plane, the frequencies of the two axial oscillations differ at all energies. They decrease as the energy increases, and their ratio approaches one, in accordance with the fact that the potential is anharmonic and becomes more nearly spherical at large radii. At $E = E_2$ the elliptic closed orbits branch off the y-axis orbits, which are unstable above this energy. At a given energy the elliptic closed orbit has the highest frequency. The reason is that the axial orbits have turning points, so that a star in such an orbit will spend a relatively long time at large amplitudes. The elliptic closed orbits do not have turning points.

Fig. 32 shows the action-diagram for this case, with lines of constant energy and lines of constant frequency ratios added. It follows from equation (131) that the slope of a line of constant energy equals minus $\omega_\lambda / \omega_\mu$. In the calculation we have taken a factor $2\pi G\varrho_0$ in the potential equal to one [*cf.* equation (17)].

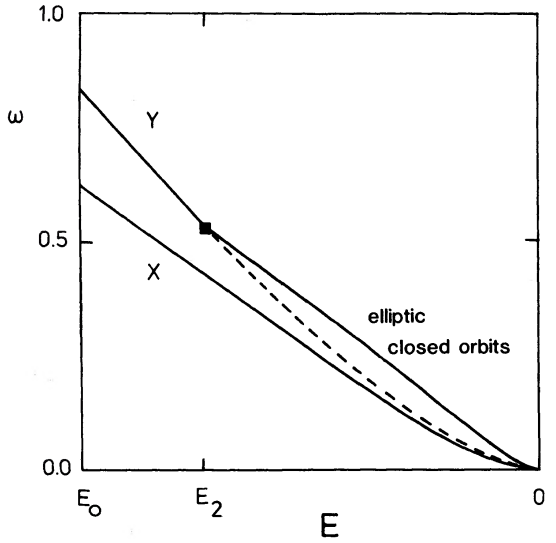

Figure 31. Frequencies of the simple periodic orbits in the (x, y)-plane of the perfect ellipsoid as function of the energy. The dashed line indicates the unstable y-axis oscillation.

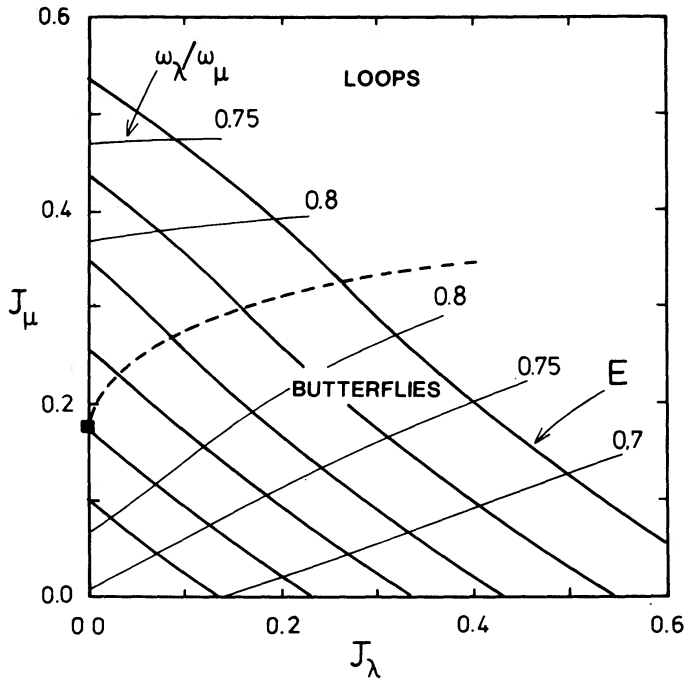

Figure 32. Action-diagram with curves of constant frequency $\omega_\lambda/\omega_\mu$ (thin), and curves of constant energy (thick). Energy increases towards the upper right.

The action-diagram is equivalent to the integral diagram Fig. 10. In both cases the line $E=0$ and the curves representing the stable simple periodic orbits limit the area in the diagram that corresponds to bound orbits in the (x, y)-plane. The general orbits are divided in loops and butterflies by the unstable y-axis orbits. In the action diagram the stable simple periodic orbits all lie along the axes, but the line $E=0$ may be at infinity, depending on the form of the function $G(\tau)$ that defines the potential.

Binney & Spergel (1984) have constructed action-diagrams for two-dimensional motion in a variety of non-axisymmetric potentials by means of the techniques of spectral stellar dynamics (Binney & Spergel 1982). For non-rotating potentials that are not too far from round, their

diagrams are closely similar to Fig. 32. Motion in such potentials can therefore be approximated quite accurately as motion separable in elliptic coordinates.

The action-diagram for motion in the (x, y)-plane of the Schwarzschild ellipsoid is given by Ratcliff, Chang & Schwarzschild (1984). It is similar to our Fig. 32, but contains a small stochastic region in the area around the unstable y-axis orbits, in agreement with the results obtained by de Zeeuw & Merritt (1983). Ratcliff *et al.* also display geometrical properties of the orbits in an action-diagram, relating to the positions of the corners of the butterflies, and to the points between which loops cross the y-axis. For the motion in a Stäckel potential we can construct a similar diagram by drawing curves of constant $\mu_{\max}$, $\lambda_{\max}$ and $\lambda_{\min}$ in an action-diagram. The result is shown in Fig. 33. All orbits on a curve of constant $\mu_{\max}$ are butterflies bounded by the same hyperbola $\mu=\mu_{\max}$ in the (x, y)-plane. Orbits on a curve of constant $\lambda_{\max}$ are either butterflies bounded by the ellipse $\lambda=\lambda_{\max}$, or they are loops, bounded at the outside by the same ellipse. With increasing J_μ the value of J_λ on a curve of constant $\lambda_{\max}$ decreases until it becomes zero. Here the loop has shrunk to an elliptic closed orbit at $\lambda=\lambda_{\max}$. At this point in the action diagram a curve of constant $\lambda_{\min}$ begins. Orbits on this curve are all loops, bounded on the inside by the ellipse $\lambda=\lambda_{\min}$.

The phase-space volume allotted to the butterflies and loops equals $(2\pi)^2$ times the area occupied by these orbits in the (J_λ, J_μ)-plane. It follows that the fractions of butterflies and loops as function of energy are given by $f_B/(f_B+f_L)$ and $f_L/(f_B+f_L)$, respectively, with

$$f_B(E)=\int_{(\alpha-\beta)(E-E_0)}^{0} |D(E,I_2)|\,dI_2, \qquad f_L(E)=\int_0^{\infty} |D(E,I_2)|\,dI_2, \tag{134}$$

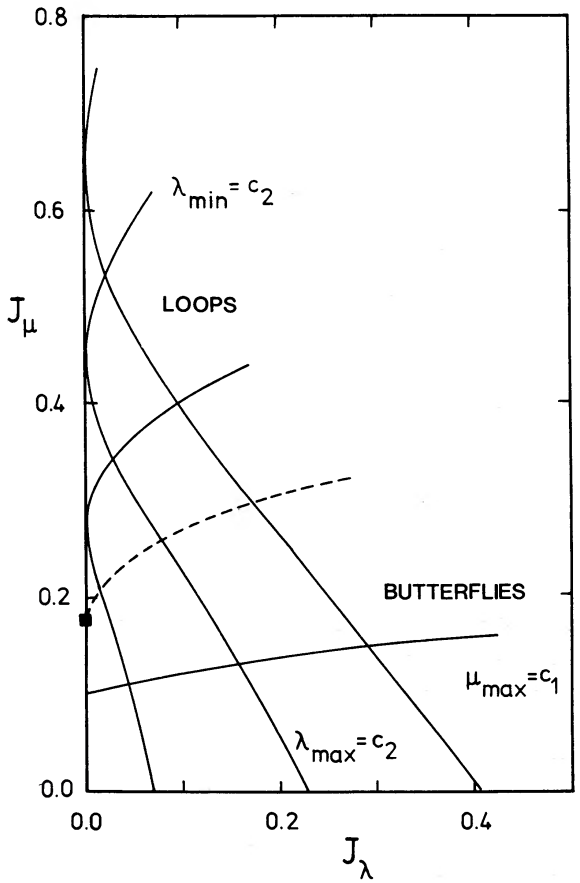

Figure 33. Action-diagram with curves of constant values of $\lambda_{\max}$, $\lambda_{\min}$ and $\mu_{\max}$.

where D is the Jacobian of the transformation from (J_λ, J_μ) to (H, I_2), given in (130). For $E_0 \leq E \leq E_2$ only butterflies exist.

9.4 PROLATE SPHEROID

When the short and intermediate axes of the perfect ellipsoid are equal it is a prolate spheroid with the x-axis as symmetry axis. Now $\beta=\gamma$, and the ellipsoidal coordinates are oblate spheroidal coordinates (λ, μ, χ). In each meridional plane χ=constant the variables λ and μ are elliptic coordinates. In this case I_3 is a classical integral of motion, equal to $\frac{1}{2}L_x^2$, where L_x is the component of the angular momentum parallel to the symmetry axis.

The orbit classification is given in Section 6.1. Of the four families of general orbits of the triaxial model only two remain: inner and outer long axis tubes. No box orbits or short axis tubes occur in the perfect prolate spheroid.

The actions can be calculated by means of equation (132). We find

$$J_\nu = J_\chi = \frac{2}{\pi}\int_0^{\pi/2} p_\chi \, d\chi = l_x = \sqrt{2i_3}, \tag{135}$$

where l_x is the value of L_x. It follows that

$$\frac{\partial J_\chi}{\partial H} = \frac{\partial J_\chi}{\partial I_2} = 0. \tag{136}$$

Substitution of (136) in the expressions (125) for the frequencies shows that ω_λ and ω_μ are in this case given by the two-dimensional expressions (129). This is not surprising since the three-dimensional motion in the perfect prolate spheroid can also be described as two-dimensional motion in a meridional plane, in a reduced potential that is separable in elliptic coordinates (λ, μ).

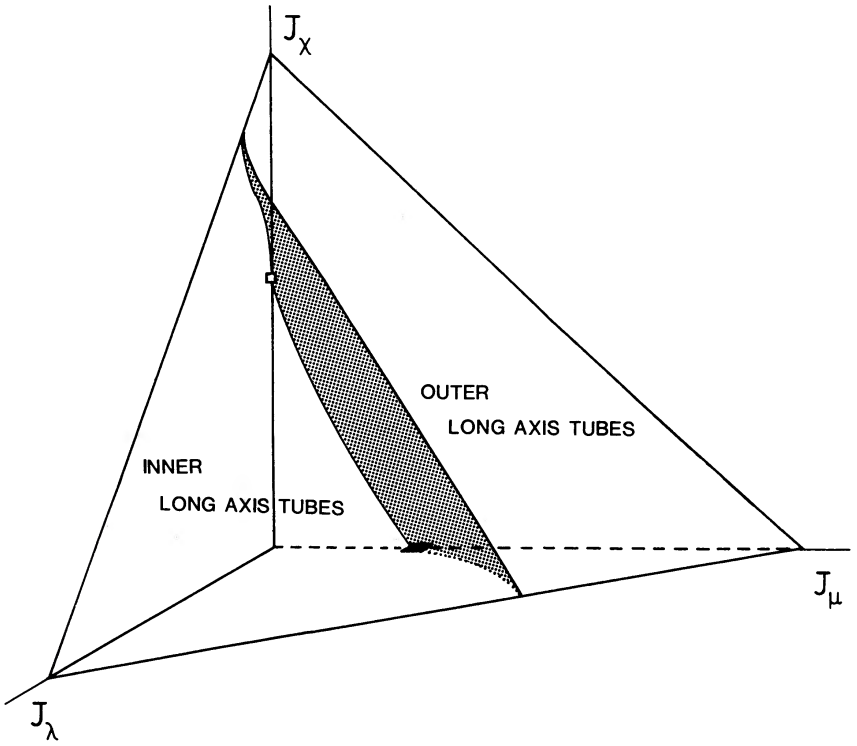

Figure 34. Action-diagram for the orbits in the perfect prolate spheroid. The diagram is equivalent to Fig. 21.

Fig. 34 is the action-diagram for the perfect prolate spheroid. As in Section 4.1, each point in it may be related to a general orbit, or to a limiting or transitional orbit. This can be done easily by a comparison with the equivalent integral diagram, Fig. 21.

Fig. 34 can be obtained as a limiting case of the diagram for the triaxial case (Fig. 28) quite easily. Since the model is axisymmetric with respect to the x-axis, the motion in the (x, y)- and (x, z)-plane is identical. This means that, when $\beta \rightarrow \gamma$, the light shaded surface in Fig. 28 drops onto the plane $J_\nu = 0$. The result is Fig. 34.

9.5 OBLATE SPHEROID

When the intermediate axis equals the long axis, the perfect ellipsoid is an oblate spheroid, with the z-axis as symmetry axis. In this case $\alpha = \beta$ and the ellipsoidal coordinates are prolate spheroidal coordinates (λ, ϕ, ν). In each meridional plane ϕ=constant the variables λ and ν are elliptic coordinates. The integral I_2 is now a classical integral, $I_2 = \frac{1}{2}L_z^2$, where L_z is the angular momentum component parallel to the symmetry axis.

The orbit classification is given in Section 6.2. The general orbits are all short axis tubes. No boxes, inner and outer long axis tubes exist in the perfect oblate spheroid.

The actions can be calculated by means of (132). We find

$$J_\mu = J_\phi = \frac{2}{\pi} \int_0^{\pi/2} p_\phi \, d\phi = l_z = \sqrt{2 i_2}, \tag{137}$$

where l_z is the value of L_z. It follows that

$$\frac{\partial J_\phi}{\partial H} = \frac{\partial J_\phi}{\partial I_3} = 0. \tag{138}$$

Substitution of (138) in the expressions (125) shows that ω_λ and ω_μ are given by expressions

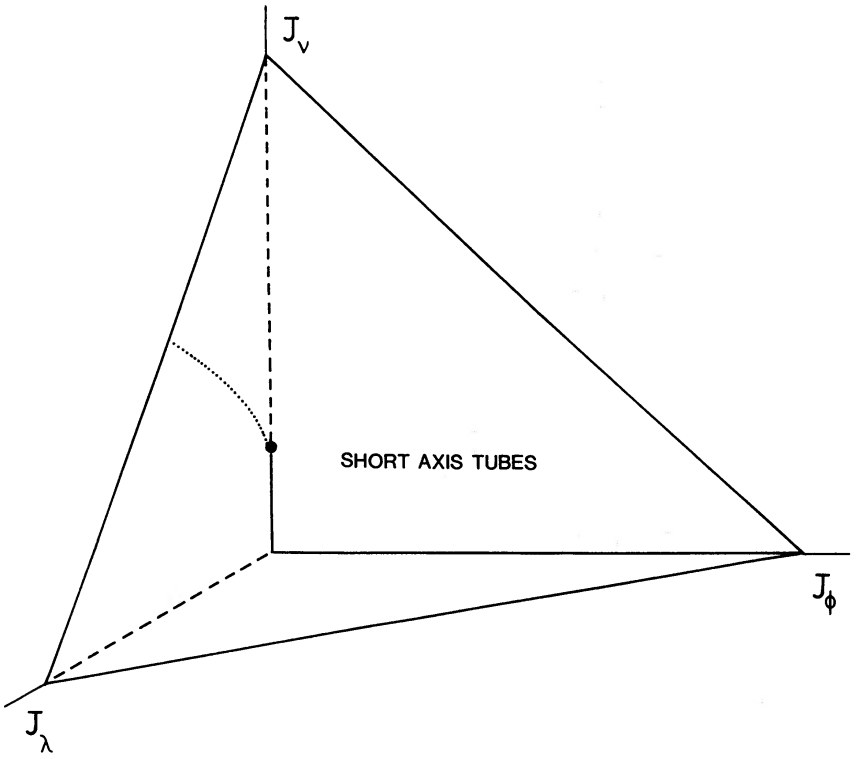

Figure 35. Action-diagram for the orbits in the perfect oblate spheroid. The diagram is equivalent to Fig. 25.

similar to (129). Just as in the prolate case, the motion in the axisymmetric potential may be described as two-dimensional motion in a meridional plane in a reduced potential that is separable in the elliptic coordinates (λ, ν).

Fig. 35 is the action-diagram for the perfect oblate spheroid. It is equivalent to the integral diagram shown in Fig. 25. The orbital structure evidently is rather simple, compared with the triaxial case.

Fig. 35 can be obtained from Fig. 28 by noting that in the oblate model motion in the (x, z)- and (y, z)-planes is identical. When $\beta \rightarrow \alpha$, the light shaded as well as the dark shaded surface in Fig. 28 merge with the (J_λ, J_ν)-plane, so that only the short axis tubes remain.

10 Discussion

10.1 COMPARISON WITH THE SCHWARZSCHILD ELLIPSOID

Schwarzschild (1979, 1982) has constructed realistic models of elliptical galaxies by means of linear programming. In the potential of a given mass model stellar orbits and their individual densities are calculated. The latter are added in such a way that the mass model is reproduced with non-negative occupation numbers for all orbits. These occupation numbers represent the phase-space distribution function that is consistent with the assumed mass model.

The mass model chosen by Schwarzschild is roughly ellipsoidal with axial ratios 1:5/8:1/2. The radial density profile is $\varrho(r) \sim (1+r^2)^{-3/2}$, which falls off as r^{-3} at large radii r, and gives a finite density in the centre. Following Tremaine (1983), we refer to this model as the Schwarzschild ellipsoid.* Schwarzschild first constructed a self-consistent solution for this ellipsoid in the absence of figure rotation, and later also with rotation.

The basic periodic orbits that occur in the Schwarzschild ellipsoid are the three oscillations along the principal axes – and closed, nearly elliptic, orbits in the three principal planes. These are exactly the six simple periodic orbits that exist in the perfect ellipsoid, and they have identical stability properties (Heiligman & Schwarzschild 1979; Schwarzschild 1981).

Schwarzschild concluded that three major families of general orbits exist in his model, each one related to a stable periodic orbit family: boxes, short axis tubes and long axis tubes. Cross-sections with the principal planes of the volume filled by a typical box orbit and by a typical short axis tube are shown in figs 2 and 3, respectively, of Schwarzschild (1979). They are nearly identical with the similar cross-sections for these orbits in the perfect ellipsoid, which are shown in Figs 8a and d. After it became clear that in the perfect ellipsoid there are *two* distinct families of long axis tubes, Schwarzschild (private communication) kindly re-investigated the orbits in his non-rotating model. He found that the long axis tubes in his model are also of two kinds, both of which occur in the self-consistent solution. The cross-sections with the principal planes of the volumes filled by these orbits are very similar to those shown in Figs 8b and c for the perfect ellipsoid.

In each of the principal planes of the Schwarzschild ellipsoid there are two major families of general orbits: butterflies and loops. Representative orbits in the (x, y)-plane are shown in Fig. 7 of de Zeeuw & Merritt (1983). By analogy with the analysis in Sections 5.3 and 5.4 of the present paper we conclude that the butterflies and loops in the (x, z)- and (y, z)-planes of the Schwarzschild ellipsoid are not all stable to perpendicular perturbations.

In addition to the four major families of three-dimensional orbits, the transitional orbits between them and the simple periodic orbits, the Schwarzschild ellipsoid also contains minor orbit families connected with higher order periodic orbits, and a small fraction of stochastic orbits, related to unstable orbits (Goodman & Schwarzschild 1981; de Zeeuw & Merritt 1983). These are the signature of a non-integrable potential.

*This ellipsoid should not be confused with the velocity ellipsoid introduced by K. Schwarzschild in 1907.

The perfect ellipsoid has all orbit families that are the major building blocks of Schwarzschild's non-rotating model galaxy. This model is thought to be representative of triaxial elliptical galaxies. We conclude that *the perfect ellipsoid contains all orbit families that are of major importance for the structure and dynamics of non-rotating triaxial elliptical galaxies*. It follows that, *if* a phase space distribution function $f(H, I_2, I_3)$ exists that is consistent with the perfect ellipsoid – i.e. that satisfies (111) – then the resulting equilibrium model deserves to be called the *perfect elliptical galaxy*.

10.2 SOME IMPLICATIONS

Real ellipticals are nearly perfect (or, depending on one's taste: perfect ellipticals are nearly real). Some imperfections are:

(i) The radial brightness profile of elliptical galaxies is represented well by a de Vaucouleurs or a King law (e.g. Kormendy 1982). Assuming that the ratio of mass-to-light is constant, this means that the underlying density distribution differs from that of the perfect ellipsoid, given in (13).

(ii) The contours of constant surface brightness of ellipticals are usually well approximated by concentric ellipses (Carter 1978). The position angle of the major axis, as well as the axis ratios, of these isophotes in many cases vary with radius (King 1978; Williams & Schwarzschild 1979; Leach 1981). This requires that in the underlying mass distribution the surfaces of constant density are not all similar aligned concentric ellipsoids (Contopoulos 1956; Stark 1977). This means that the perfect ellipsoid will not show twisting isophotes and ellipticity changes.

(iii) Although observationally one cannot distinguish star streaming within the figure from rotation of the figure – but see Tremaine & Weinberg (1984) – it is generally believed that the figures of ellipticals rotate, albeit slowly (Binney 1978b; Illingworth 1981). The perfect ellipsoid has a non-rotating figure.

(iv) Not all stellar orbits in an elliptical galaxy will belong to the four families present in the perfect ellipsoid. In other words, it is unlikely that elliptical galaxies have gravitational potentials that lead to exactly separable equations of motion. As in Schwarzschild's ellipsoid, there will be minor families trapped around higher order periodic orbits, as well as some stochastic orbits.

In what follows we shall discuss these points in some detail, and argue that *all these defects detract little from the advantage of having mass models with arbitrary axis ratios that have all important orbit families, and in which motion can be described by analytic means.*

Many other triaxial mass models exist with potentials of Stäckel form. These models are not stratified exactly on similar aligned concentric ellipsoids (since the perfect ellipsoid is the only such one) and have radial density profiles different from that given in equation (13). It is not at all unlikely that triaxial mass models exist with Stäckel potentials that come closer to being realistic than the perfect ellipsoid. We have seen in Section 6 that all centrally concentrated models of this kind have exactly the same orbital structure as the perfect ellipsoid.

Kuzmin (1956) showed that axisymmetric mass models with separable potentials have remarkable properties, and that elegant methods exist for the construction of such models. Triaxial models can be constructed by similar methods (de Zeeuw 1985b), and we will discuss these in a future paper (de Zeeuw, Peletier & Franx 1985, in preparation).

Rotation of the figure is probably unimportant for the structure of large elliptical galaxies (Binney 1978b; Illingworth 1981). Slowly rotating models resemble non-rotating ones in many respects (Schwarzschild 1982; Wilkinson & James 1982). Therefore, a description of at least the large ellipticals based on non-rotating mass models like the perfect ellipsoid should be adequate for many purposes. Furthermore, the close analogy between the orbits in the perfect ellipsoid and those in Schwarzschild's non-rotating models leads one to wonder whether a similar analogy

exists in case of rotation. In other words, are there inhomogeneous triaxial mass models that rotate and have potentials that admit three integrals for all orbits in them? In contrast with the case of no rotation, little is known concerning this problem (e.g. Lynden-Bell 1962c). At present only two such potentials are known: the three-dimensional uniformly rotating harmonic oscillator and a special case found recently by Vandervoort (1979). The former is the gravitational potential inside a uniformly rotating homogeneous triaxial ellipsoid, and has been used by Freeman (1966) when he constructed simple models for rotating stellar systems (see also Hunter 1974). Vandervoort (1979) showed that no other rotating potentials exist with an integral quadratic in the velocities in addition to the energy integral. Whether potentials exist with extra integrals that are not quadratic in the velocities is unclear (e.g. Binney 1984), but it is certainly a problem that deserves attention.

No ellipticals flatter than about E6 exist (Binney & de Vaucouleurs 1981). As a result, the gravitational potentials of these galaxies are not only of nearly Stäckel form, but they are also not too far from spherical. It is *precisely* in this case that the small perturbations that cause a Stäckel potential to become non-separable, do not induce a drastic change in the phase-space structure (de Zeeuw 1985a). Minor orbit families will occur, and some stochastic orbits. Goodman & Schwarzschild (1981) showed that these orbits are unlikely to play an important role in the dynamics of ellipticals. The major orbit families are still the four found in the perfect ellipsoid, although their shapes may be a little different. Thus, for many purposes it is adequate to use the separable models for a description of the structure and dynamics of (non-rotating) triaxial elliptical galaxies.

10.3 THE SPECIAL CASES

From the analysis presented in Sections 5 and 6 it is clear that the orbital structure in centrally concentrated mass models with separable potentials becomes progressively richer with a decrease in the degree of symmetry of the models. In spherical models all orbits are loops in planes through the centre. (Note that the distinction 'of Stäckel form' is redundant in this case, since every spherical potential is a Stäckel potential.) In the axisymmetric models the loops become three-dimensional tube orbits around the symmetry axis. The triaxial models not only contain tubes around both the short and the long axis, but also contain box orbits.

In all cases there are three quadratic integrals of motion for each orbit. The non-classical integrals are natural generalizations of the angular momentum integrals that exist in axisymmetric and spherical potentials. The existence of the three independent isolating integrals makes it possible to derive the orbital shapes, and their individual densities, without integrating the equations of motion. The method we have employed for this – comparison of effective potential curves with lines of constant energy – reduces in a natural way to the customary method for the determination of the motion in a spherical potential, and is just as easy to use.

For centrally concentrated triaxial mass models with Stäckel potentials that are not too far from spherical, a small perturbation that causes the potential to become non-separable will not change the orbital structure drastically (*cf.* Section 10.2). This is also true for the oblate and prolate degeneracies. Indeed, numerical orbit calculations in oblate axisymmetric potentials show that most orbits are short axis tubes (e.g. Ollongren 1962; Martinet & Hayli 1971).

The disc-like degeneracies deserve some special attention. Kuzmin's disc is a convenient mass model for the understanding of the dynamics of infinitely thin axisymmetric discs (Kuzmin 1953). It can represent an exponential disc reasonably well to about 4.5 scale lengths (Toomre 1963). The simple form of the potential allows the explicit calculation of many properties. An example is the recent use by Schweizer, Whitmore & Rubin (1983) of the velocity of a star in the elliptic

closed orbit over the pole of the disc as function of radius for the interpretation of observations of polar dust rings around S0 galaxies.

The perfect elliptic disc is the non-axisymmetric separable generalization of Kuzmin's disc. The orbital structure in the disc is generic for all non-rotating non-axisymmetric centrally concentrated infinitesimally thin discs, provided that the axis ratio is not smaller than about 1/3. It follows that the perfect elliptic disc, and more generally, infinitesimally thin discs with Stäckel potentials, are useful mass models for the description of mildly ovally distorted discs, and also for some barred stellar systems.

10.4 SPECTRAL STELLAR DYNAMICS

Actions and angles are the natural variables for the description of separable motion. Recently, Binney & Spergel (1982, 1984) have developed a numerical method, termed *spectral stellar dynamics*, for the calculation of actions and frequencies of a given orbit in a non-separable potential. By a Fourier analysis of the time-dependence of the coordinates of a star in a given orbit they obtain the spectrum of the orbit, from which the fundamental orbital frequencies and the action integrals are deduced. Ratcliff *et al.* (1984) turned this procedure around, and computed the orbits, for given frequencies or actions, in a given potential. In both cases, the orbits can be studied and classified in terms of the numerical values that are obtained for the integrals of motion.

The action-diagrams found by Binney & Spergel for motion in two-dimensional non-rotating potentials that are not too far from round, are essentially equivalent to the action-diagram presented here for the (x, y)-plane of the perfect ellipsoid (Figs 32–33). For all such potentials motion is therefore quite accurately described as slightly perturbed separable motion in a Stäckel potential. The potentials of (at least) the non-rotating elliptical galaxies are nearly of three-dimensional Stäckel form, and at most moderately triaxial. When spectral dynamics will be applied to motion in such potentials, the action diagrams presented in Section 9 should be useful guides in the investigation of the orbital structure.

Actions are adiabatic invariants, so they are the natural variables to use when studying secular evolution in stellar systems (e.g. Norman 1983). Binney & Spergel find that in the two-dimensional potentials that have action diagrams equivalent to our Fig. 32, the actions are well conserved during a slow evolution of the potential, even when, in the process, the orbit changes from loop to butterfly, or vice versa. However, when the potential is very elongated, or rotating, actions may change discontinuously across the transition from one orbit family to another. It is to be expected that in the three-dimensional potentials of triaxial elliptical galaxies the actions of the individual stellar orbits are well conserved during a slow evolution.

Binney & Spergel first numerically compute an orbit in a given potential, and then Fourier analyse the resulting $x(t)$ and $y(t)$ in order to obtain the spectrum of the orbit which in turn yields the frequencies and the actions. Ratcliff *et al.* (1984) reverse this procedure and compute the orbit for given actions or frequencies. They transform the equations of motion to angle variables and represent the coordinates x and y as truncated Fourier series in the angles. The Fourier coefficients are determined by the requirement that the series satisfy the equations of motion on a grid of points in angle-space. An important advantage of this method for the calculation of orbits in a given potential is that a solution covers only a finite region in angle-space, since both angles are periodic. As a result, a bound on the numerical error in the procedure immediately translates to a bound on the error in the orbit valid for all times. This is in contrast with the usual procedure in which x and y are calculated directly as function of time.

Unfortunately, Ratcliff *et al.* find that a relatively large number of terms is needed in order to obtain good accuracy. They estimate that an application to three-dimensional motion, although

straightforward in principle, will be rather costly in computer time. It seems worthwhile to investigate whether the calculations required can be reduced drastically, especially in three-dimensions, by use of properly chosen ellipsoidal coordinates, instead of Cartesian coordinates. Such a procedure might be considered as a numerical perturbation technique for the study of motion in slightly perturbed Stäckel potentials.

10.5 SELF-CONSISTENT MODELS

The construction of self-consistent models for density distributions that have a gravitational potential of Stäckel form is straightforward by means of Schwarzschild's (1979) linear programming technique. The orbital densities needed for this can be simply evaluated from expressions given in Section 7, without even calculating the orbits themselves. This speeds up the construction process considerably. If one or more self-consistent solutions exist for a given mass model, then the occupation numbers of the orbits that make up the model, together with their known integrals of motion, will provide a discrete numerical approximation to the distribution function $f(H, I_2, I_3)$. Whether it is possible to derive distribution functions by analytic means remains to be seen. Experience with spherical and axisymmetric models (Eddington 1915b; Lynden-Bell 1962a; Hunter 1975; Lake 1981; DeJonghe 1984) makes it rather unlikely that an explicit inversion of the fundamental integral equation (111) is possible. Derivation of at least some of the properties of f by analytic means would already be extremely useful, since it would allow the study, if not the construction, of whole classes of equilibrium models at once, and bring a delineation of the full variety of such models for elliptical galaxies within reach.

Before attempting to solve the triaxial problem it is worthwhile to try to solve the similar problem for the perfect elliptic disc. The appropriate integral equation can be derived easily from equation (115). This problem is 'only' two-dimensional, and has many aspects of the three-dimensional problem. There is more than one family of general orbits, and every orbit enjoys a non-classical integral of motion in addition to the energy. Furthermore, for the limiting case of Kuzmin's disc, distribution functions already exist (Shu 1969; Miyamoto 1971, 1974; Kalnajs 1976). From the arguments given above it follows that such a solution would be useful for the understanding of disc-like stellar systems as well.

10.6 CONCLUDING REMARKS

From the preceding arguments we conclude that:

(i) The ellipsoidal coordinates discovered by Lamé and Jacobi are the natural coordinates for the description of non-rotating triaxial elliptical galaxies.

(ii) The orbit families that are of major importance for the structure and dynamics of triaxial elliptical galaxies are precisely those found in Stäckel potentials. Thus, potentials of ellipticals are well approximated by Stäckel potentials. The integrals of motion enjoyed by most stars in these systems, two non-classical ones in addition to the energy, are well approximated by the quadratic integrals admitted by Stäckel potentials.

(iii) Study of exactly separable models is worthwhile for the understanding of the equilibrium structures of elliptical galaxies.

It is appropriate to recall a statement made by Jacobi (1866) in his 'Vorlesungen über Dynamik'. In the first paragraph of chapter 26, devoted to ellipsoidal coordinates, he writes: 'Die Hauptschwierigkeit bei der Integration gegebener Differentialgleichungen scheint in der Einführung der richtigen Variabeln zu bestehen, zu deren Auffindung es keine allgemeine Regel giebt. Man muss daher das umgekehrte Verfahren einschlagen und nach erlangter Kenntniss

einer merkwürdigen Substitution die Probleme aufsuchen bei welchem dieselbe mit Glück zu brauchen ist.' Then he discusses one such remarkable set of variables, the ellipsoidal coordinates (in n dimensions) and the problems where – at that time, 1842 – he had already used them with success. Among these is the determination of the geodesics on a triaxial ellipsoid, and his rederivation of Euler's (1760) solution of the problem of motion in the field of force of two point masses. The elucidation of the dynamics of triaxial ellipticals may now be added to Jacobi's list. Chandrasekhar's (1942) remark in the preface of his book on 'Principles of Stellar Dynamics', that 'several of the problems of modern stellar dynamical theory are so severely classical that it is difficult to believe that they are not already discussed, for example, in Jacobi's Vorlesungen', clearly applies.

Acknowledgments

It is a great pleasure to thank H. C. van de Hulst for his continued interest and encouragement during the course of this work. His comments, together with those of M. Schwarzschild, M. Franx and the referee, J. Binney, considerably improved both the contents and the presentation of the paper. D. Lynden-Bell's suggestion that 'it might be interesting to look at ellipsoidal coordinates and Stäckel potentials' is appreciated very much. M. Schwarzschild kindly re-investigated the stellar orbits in his non-rotating model. Discussions with C. A. Norman were stimulating. C. de Vries assisted with the use of the Westerbork routines for the preparation of Fig. 27. The hospitality of the Institute of Astronomy in Cambridge, where part of this work was done, is gratefully acknowledged. The final part of this work was partially supported by NSF Grants PHY-82-17352 and PHY-84-40263.

References

Arnold, V., 1978. *Mathematical Methods of Classical Mechanics,* Springer, New York.
Bertrand, J., 1852. *J. de Math.*, **17,** 121.
Binney, J. J., 1978a. *Mon. Not. R. astr. Soc.*, **183,** 501.
Binney, J. J., 1978b. *Comments Astrophys.*, **8,** 27.
Binney, J. J., 1982. In: *Morphology and Dynamics of Galaxies,* Proc. Twelfth Adv. Course of the Swiss Society of Astr. and Astrophys., p. 1, eds Martinet, L. & Mayor, M., Observatoire de Genève, Sauverny.
Binney, J. J., 1984. In: *Essays in Theoretical Physics*, ed. Parry, W. E., Pergamon Press, Oxford.
Binney, J. J. & Spergel, D., 1982. *Astrophys. J.*, **252,** 308.
Binney, J. J. & Spergel, D., 1984. *Mon. Not. R. astr. Soc.*, **206,** 159.
Binney, J. J. & de Vaucouleurs, G., 1981. *Mon. Not. R. astr. Soc.*, **194,** 679.
Byrd, P. F. & Friedman, M. D., 1971. *Handbook of Elliptic Integrals for Engineers and Scientists*, Springer Verlag, Berlin.
Carter, D., 1978. *Mon. Not. R. astr. Soc.*, **182,** 797.
Chandrasekhar, S., 1942. *Principles of Stellar Dynamics*, University of Chicago Press.
Chandrasekhar, S., 1969. *Ellipsoidal Figures of Equilibrium*, Yale University Press, New Haven.
Charlier, C. L., 1927. *Die Mechanik des Himmels*, Vol. 1, de Gruyter, Berlin.
Clark, G. L., 1936. *Mon. Not. R. astr. Soc.*, **97,** 182.
Contopoulos, G., 1956. *Z. Astrophys.*, **39,** 126.
Contopoulos, G., 1960. *Z. Astrophys.*, **49,** 273.
Dall'Acqua, F. A., 1908. *Math. Ann.*, **66,** 394.
DeJonghe, H., 1984. *PhD thesis*, Gent University, Belgium.
de Zeeuw, P. T., 1985a. *Mon. Not. R. astr. Soc.*, **215,** 729.
de Zeeuw, P. T., 1985b. *Mon. Not. R. astr. Soc.*, in press.
de Zeeuw, P. T. & Lynden-Bell, D., 1985. *Mon. Not. R. astr. Soc.*, **215,** 711.
de Zeeuw, P. T. & Merritt, D. R., 1983. *Astrophys. J.*, **267,** 571.
Eddington, A. S., 1915a. *Mon. Not. R. astr. Soc.*, **76,** 37.
Eddington, A. S., 1915b. *Mon. Not. R. astr. Soc.*, **76,** 572.

Euler, L., 1760. *Mem. de l'Acad. de Berlin.*
Freeman, K. C., 1966. *Mon. Not. R. astr. Soc.,* **134,** 1.
Goldstein, H., 1980. *Classical Mechanics,* 2nd edn, Addison Wesley, London.
Goodman, J. & Schwarzschild, M., 1981. *Astrophys. J.,* **245,** 1087.
Heiligman, G. & Schwarzschild, M., 1979. *Astrophys. J.,* **233,** 872.
Hori, G., 1962. *Publs astr. Soc. Japan,* **14,** 353.
Hunter, C., 1974. *Mon. Not. R. astr. Soc.,* **166,** 633.
Hunter, C., 1975. *Astr. J.,* **80,** 783.
Hunter, C., 1980. *Publs astr. Soc. Japan,* **32,** 33.
Illingworth, G., 1981. In: *The Structure and Evolution of Normal Galaxies*, p. 27, eds Fall, S. M. & Lynden-Bell, D., Cambridge University Press.
Jacobi, C. G. J., 1839. *J. für Math.*, **19,** 309.
Jacobi, C. G. J., 1866. *Vorlesungen über Dynamik*, given at Königsberg 1842–3, published by A. Clebsch, Reimer, Berlin, Ch. 26.
Jeans, J. H., 1915. *Mon. Not. R. astr. Soc.,* **76,** 71.
Kalnajs, A. J., 1976. *Astrophys. J.,* **205,** 751.
King, I. R., 1978. *Astrophys. J.,* **222,** 1.
Kormendy, J., 1982. In: *Morphology and Dynamics of Galaxies*, Proc. Twelfth Adv. Course of the Swiss Society of Astr. and Astrophys., p. 113, eds Martinet, L. & Mayor, M., Observatoire de Genève, Sauverny.
Kuzmin, G. G., 1953. *Tartu Astr. Obs. Teated,* **1.**
Kuzmin, G. G., 1956. *Astr. Zh.,* **33,** 27.
Lake, G., 1981. *Astrophys. J.,* **243,** 111.
Lamé, G., 1837. *J. de Math.,* **2,** 147.
Landau, L. D. & Lifshitz, E. M., 1976. *Mechanics*, 3rd edn, Pergamon Press, Oxford.
Leach, R., 1981. *Astrophys. J.,* **248,** 485.
Levi Civita, T., 1904. *Math. Ann.,* **59,** 383.
Liouville, J., 1846. *J. de Math.,* **11,** 345.
Lynden-Bell, D., 1962a. *Mon. Not. R. astr. Soc.,* **123,** 447.
Lynden-Bell, D., 1962b. *Mon. Not. R. astr. Soc.,* **124,** 1.
Lynden-Bell, D., 1962c. *Mon. Not. R. astr. Soc.,* **124,** 95.
Lyttleton, R. A., 1953. *The Stability of Rotating Liquid Masses*, Cambridge University Press.
Martinet, L. & Hayli, A., 1971. *Astr. Astrophys.,* **14,** 103.
Merritt, D. R., 1980. *Astrophys. J. Suppl.,* **43,** 435.
Miyamoto, M., 1971. *Publs astr. Soc. Pacif.,* **23,** 21.
Miyamoto, M., 1974. *Astr. Astrophys.,* **30,** 441.
Morse, P. M. & Feshbach, H., 1953. *Methods of Theoretical Physics*, McGraw Hill, New York, Ch. 5.
Newton, A. J. & Binney, J. J., 1984. *Mon. Not. R. astr. Soc.,* **210,** 711.
Norman, C. A., 1983. In: *Formation and Evolution of Galaxies and Large Structures in the Universe*, p. 327, eds Audouze, J. & Tran Thanh Van, J., Reidel, Dordrecht, Holland.
Ollongren, A., 1962. *Bull. astr. Inst. Neth.,* **16,** 241.
Oort, J. H., 1928. *Bull. astr. Inst. Neth.,* **4,** 269.
Ratcliff, S. J., Chang, K. M. & Schwarzschild, M., 1984. *Astrophys. J.,* **279,** 610.
Richstone, D. O., 1980. *Astrophys. J.,* **238,** 103.
Schwarzschild, K., 1907. *Göttingen Nachr.,* K1, p. 614.
Schwarzschild, M., 1979. *Astrophys. J.,* **232,** 236.
Schwarzschild, M., 1981. In: *The Structure and Evolution of Normal Galaxies*, p. 43, eds Fall, S. M. & Lynden-Bell, D., Cambridge University Press.
Schwarzschild, M., 1982. *Astrophys. J.,* **263,** 599.
Schweizer, F., Whitmore, B. C. & Rubin, V. C., 1983. *Astr. J.,* **88,** 909.
Shu, F. H., 1969. *Astrophys. J.,* **158,** 505.
Stäckel, P., 1890. *Math. Ann.,* **35,** 91.
Stäckel, P., 1891. *Über die Integration der Hamilton–Jacobischen Differential gleichung mittelst Separation der Variabeln*, Habilitationsschrift, Halle.
Stäckel, P., 1893. *Math. Ann.,* **42,** 537.
Stark, A. A., 1977. *Astrophys. J.,* **213,** 368.
Toomre, A., 1963. *Astrophys. J.,* **138,** 385.
Tremaine, S., 1983. In: *Internal Kinematics and Dynamics of Galaxies, IAU Symp. No. 100*, p. 411, ed. Athanassoula, E. O., Reidel, Dordrecht, Holland.
Tremaine, S. & Weinberg, M., 1984. *Astrophys. J. Lett.,* **282,** L5.

van Albada, T. S., 1982. *Mon. Not. R. astr. Soc.*, **201**, 939.
van de Hulst, H. C., 1962. *Bull. astr. Inst. Neth.*, **16**, 235.
Vandervoort, P. O., 1979. *Astrophys. J.*, **232**, 91.
Weinacht, J., 1924. *Math. Ann.*, **91**, 279.
Whittaker, E. T. & Watson, G. N., 1902. *A Course of Modern Analysis*, Cambridge University Press.
Wilkinson, A. & James, R. A., 1982. *Mon. Not. R. astr. Soc.*, **199**, 171.
Williams, T. B. & Schwarzschild, M., 1979. *Astrophys. J.*, **227**, 56.

Appendix A: Ellipsoidal coordinates at large radii

We briefly describe the behaviour of the coordinates (λ, μ, ν) at large distances from the origin. Define spherical coordinates (r, θ, ϕ) by $x=r\sin\theta\cos\phi$, $y=r\sin\theta\sin\phi$ and $z=r\cos\theta$. Then it follows from equations (7) and (8) that for $r^2\gg1$,

$$\lambda=r^2-\alpha-(\beta-\alpha)\sin^2\theta\sin^2\phi-(\gamma-\alpha)\cos^2\theta+O(1/r^2),$$

$$\mu=\tfrac{1}{2}(\beta-\alpha)\sin^2\theta\sin^2\phi+\tfrac{1}{2}(\gamma-\alpha)\cos^2\theta-\tfrac{1}{2}(\beta+\gamma)+\tfrac{1}{2}\sqrt{\Delta}+O(1/r^2),$$

$$\nu=\tfrac{1}{2}(\beta-\alpha)\sin^2\theta\sin^2\phi+\tfrac{1}{2}(\gamma-\alpha)\cos^2\theta-\tfrac{1}{2}(\beta+\gamma)-\tfrac{1}{2}\sqrt{\Delta}+O(1/r^2), \quad \text{(A1)}$$

with

$$\Delta=[(\gamma-\alpha)\cos^2\theta-(\beta-\alpha)\sin^2\theta\sin^2\phi+(\beta-\gamma)]^2+4(\beta-\alpha)(\gamma-\alpha)\sin^2\theta\cos^2\theta\sin^2\phi. \quad \text{(A2)}$$

This shows that at *large radii* λ becomes equal to r^2, and μ and ν each depend on both angles θ and ϕ. Curves of constant μ and ν on a sphere with radius $r\gg1$ are illustrated in Fig. A1.

The (x, y)-plane is given by $\theta=\pi/2$. Then equation (A1) reduces to

$$\lambda=r^2-\alpha-(\beta-\alpha)\sin^2\phi+O(1/r^2),$$

$$\mu=(\beta-\alpha)\sin^2\phi-\beta+O(1/r^2),$$

$$\nu=-\gamma. \quad \text{(A3)}$$

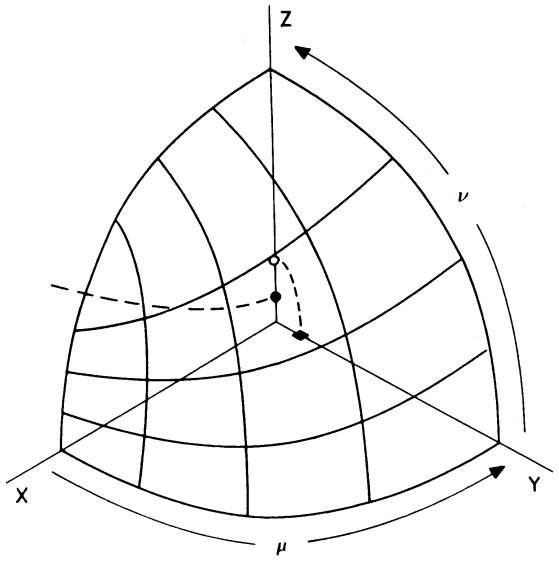

Figure A1. Behaviour of the ellipsoidal coordinates at large radii. The intersections of the hyperboloids of one (μ) and two (ν) sheets with a sphere of radius $r\gg1$ are shown. The dashed curves indicate the focal ellipse and the focal hyperbola.

For the (x, z)-plane ($\phi=0$) we find

$$\left.\begin{aligned}\lambda&=r^2-\alpha-(\gamma-\alpha)\cos^2\theta+O(1/r^2),\\ \mu&=(\gamma-\alpha)\cos^2\theta-\gamma+O(1/r^2),\\ \nu&=-\beta,\end{aligned}\right\}\quad \text{for}\quad 0\le\theta\le\theta_f,$$

$$\left.\begin{aligned}\mu&=-\beta,\\ \nu&=(\gamma-\alpha)\cos^2\theta-\gamma+O(1/r^2),\end{aligned}\right\}\quad \text{for}\quad \theta_f\le\theta\le\pi/2, \tag{A4}$$

where

$$\theta_f=\arccos\sqrt{\frac{\gamma-\beta}{\gamma-\alpha}} \tag{A5}$$

is the angle between the z-axis and the asymptote of the focal hyperbola. For the (y, z)-plane we have $\phi=\pi/2$ and (A1) reduces to

$$\begin{aligned}\lambda&=r^2-\gamma+(\gamma-\beta)\sin^2\theta+O(1/r^2),\\ \mu&=-\alpha,\\ \nu&=-\beta-(\gamma-\beta)\sin^2\theta+O(1/r^2).\end{aligned} \tag{A6}$$

Appendix B: The function $G(\tau)$

The gravitational potential V contains the function $G(\tau)$ defined in equation (23)

$$G(\mathrm{t})=\pi G\varrho_0 abc\int_0^\infty \frac{\sqrt{u-\beta}}{\sqrt{(u-\alpha)(u-\gamma)}}\times\frac{du}{u+\tau},$$

with $\alpha=-a^2, \beta=-b^2$ and $\gamma=-c^2$. Both $G(\tau)$ and its derivative $G'(\tau)$ can be expressed in terms of the incomplete elliptic integrals of the three kinds (see e.g. Byrd & Friedman 1971)

$$G(\tau)=\frac{2\pi G\varrho_0 bc}{\sin l}\frac{1}{\tau+\alpha}\left\{(\tau+\beta)\Pi\left(l,\frac{\tau+\alpha}{\alpha-\gamma},m\right)+(\alpha-\beta)F(l,m)\right\}, \tag{B1}$$

and

$$\begin{aligned}G'(\tau)=&\frac{\pi G\varrho_0 bc}{\sin l}\frac{1}{(\tau+\alpha)(\tau+\gamma)}\\ &\times\left[\frac{\{(\tau+\alpha)(\tau+\gamma)-(\tau+\alpha)(\tau+\beta)-(\tau+\beta)(\tau+\gamma)\}}{\tau+\alpha}\Pi\left(l,\frac{\tau+\alpha}{\alpha-\gamma},m\right)\right.\\ &\left.+\frac{\{(\tau+\alpha)(\beta-\gamma)+(\tau+\gamma)(\beta-\alpha)\}}{\tau+\alpha}F(l,m)-\frac{\tau+\alpha}{\alpha}bc\sin l+(\gamma-\alpha)E(l,m)\right],\end{aligned} \tag{B2}$$

with

$$F(l,\,m)=\int_0^l \frac{d\theta}{\sqrt{1-\sin^2 m\sin^2\theta}},$$

$$E(l,\,m)=\int_0^l \sqrt{1-\sin^2 m\sin^2\theta}\,d\theta,$$

$$\Pi(l,s^2,m)=\int_0^l \frac{d\theta}{(1-s^2\sin^2\theta)\sqrt{1-\sin^2 m\sin^2\theta}}. \tag{B3}$$

Here we have introduced the angles l and m by

$$c=a\cos l, \qquad b=a\sqrt{1-\sin^2 m\sin^2 l}, \tag{B4}$$

so that

$$\beta-\alpha=a^2\sin^2 l\sin^2 m, \qquad \gamma-\alpha=a^2\sin^2 l, \qquad \gamma-\beta=a^2\sin^2 l\cos^2 m. \tag{B5}$$

Important special values are

$$G(-\alpha)=\frac{2\pi G\varrho_0 bc}{\sin l}E(l,\,m),$$

$$G(-\beta)=\frac{2\pi G\varrho_0 bc}{\sin l}F(l,\,m),$$

$$G(-\gamma)=\frac{2\pi G\varrho_0 bc}{\sin l}\left\{F(l,m)-E(l,m)+\frac{b}{c}\sin l\right\}, \tag{B6}$$

and

$$G'(-\alpha)=-\frac{2\pi G\varrho_0 bc}{3\alpha^2\sin^3 l\sin^2 m}\left\{\cos^2 mF(l,\,m)+(2\sin^2 m-1)\,E(l,m)-\frac{b}{a}\sin^2 m\sin l\cos l\right\},$$

$$G'(-\beta)=-\frac{2\pi G\varrho_0 bc}{a^2\sin^3 l\sin^2 m\cos^2 m}\left\{E(l,\,m)-\cos^2 mF(l,\,m)-\frac{c}{b}\sin^2 m\sin l\right\},$$

$$G'(-\gamma)=-\frac{\pi G\varrho_0 bc}{3a^2\sin^3 l\cos^2 m}\left\{-\cos^2 mF(l,m)+(2\cos^2 m-1)\,E(l,m)+\frac{b}{c}\sin l\left(\frac{b^2}{c^2}-\cos^2 m\right)\right\}. \tag{B7}$$

For values of $\tau\gg a^2$ the behaviour of $G(\tau)$ is

$$G(\tau)=\frac{2\pi G\varrho_0 abc}{\sqrt{\tau+\gamma}}\arctan\sqrt{\frac{\tau+\gamma}{-\gamma}}+\mathrm{O}(1/\tau)$$

$$=\frac{\pi^2 G\varrho_0 abc}{\sqrt{\tau}}+\mathrm{O}(1/\tau). \tag{B8}$$

The coefficients of the terms of order $1/\tau$ and higher can be written as an infinite series in $\sin^2 m$.

Extensive tables of E and F exist, but calculation of Π requires the evaluation of an infinite series. In practice it is much easier to evaluate $G(\tau)$ and $G'(\tau)$ by direct numerical integration. We

found it handy to rewrite the integrals by the substitution $s=c/\sqrt{u+c^2}$. The result is

$$G(\tau)=2\pi G\varrho_0 abc^2\int_0^1 \frac{\sqrt{c^2+(b^2-c^2)s^2}}{\sqrt{c^2+(a^2-c^2)s^2}}\times\frac{ds}{c^2+(\tau-c^2)s^2},\qquad \tau>c^2. \tag{B9}$$

The integrand now is regular and smooth. The corresponding function $G'(\tau)$ follows immediately upon differentiation of the integrand with respect to τ.

For the perfect prolate spheroid $\beta=\gamma$ so that $m=\pi/2$. $G(\tau)$ is given in (25). Special values are:

$$G(-\alpha)=2\pi G\varrho_0 b^2,$$

$$G(-\beta)=2\pi G\varrho_0 a^2\frac{(1-e^2)}{2e}\ln\frac{1+e}{1-e},$$

$$G'(-\alpha)=-\frac{2}{3}\pi G\varrho_0(1-e^2),$$

$$G'(-\beta)=-\frac{\pi G p_0}{e^2}\left\{-1+\frac{(1-e^2}{2e}\ln\frac{1+e}{1-e}\right\}, \tag{B10}$$

where e is defined by $e=\sin l$, so that $b^2=a^2(1-e^2)$.

For the perfect oblate spheroid $\alpha=\beta$, so that $m=0$. $G(\tau)$ is given in (27). Special values are:

$$G(-\alpha)=2\pi G\varrho_0 a^2\frac{\sqrt{1-e^2}}{e}\arcsin e.$$

$$G(-\gamma)=2\pi G\varrho_0 a^2,$$

$$G'(-\alpha)=\pi G\varrho_0\frac{\sqrt{1-e^2}}{e^2}\left\{\sqrt{1-e^2}-\frac{\arcsin e}{e}\right\},$$

$$G'(-\gamma)=-\frac{2\pi G\varrho_0}{3(1-e^2)}, \tag{B11}$$

with $e=\sin l$, so that $c^2=a^2(1-e^2)$.

For the perfect sphere we have $\alpha=\beta=\gamma$ and $G(\tau)$ is given in (28). Thus,

$$G(-\alpha)=2\pi G\varrho_0 a^2,\qquad G'(-\alpha)=-\frac{2}{3}\pi G\varrho_0. \tag{B12}$$

For the perfect elliptic disc we have $\alpha<\beta<\gamma=0$, so that $l=\pi/2$ and $b=a\cos m$. We find

$$G(\tau)=\frac{4G\Sigma_0 b}{\tau+\alpha}\left\{(\tau+\beta)\Pi\left(\frac{\tau+\alpha}{\alpha},m\right)+(\alpha-\beta)F(m)\right\},$$

$$G'(\tau)=\frac{2G\Sigma_0 b}{\tau(\tau+\alpha)^2}\left[\{\tau(\alpha-\beta)-(\tau+\alpha)(\tau+\beta)\}\Pi\left(\frac{\tau+\alpha}{\alpha},m\right)\right.$$

$$\left.+\{(\tau+\alpha)\beta+\tau(\beta-\alpha)\}F(m)-\alpha(\tau+\alpha)E(m)\right], \tag{B13}$$

where $F(m)=F(\pi/2,\,m)$, $E(m)=E(\pi/2,\,m)$ and $\Pi(s^2,\,m)=\Pi(\pi/2,\,s^2,\,m)$ are the complete

elliptic integrals of the three kinds [*cf.* (B3)]. Special values are

$$G(-\alpha)=4G\Sigma_0 bE(m),$$

$$G(-\beta)=4G\Sigma_0 bF(m),$$

$$G'(-\alpha)=-\frac{4G\Sigma_0 b}{3a^2\sin^2 m}\{\cos^2 mF(m)+(2\sin^2 m-1)\,E(m)\},$$

$$G'(-\beta)=-\frac{4G\Sigma_0 b}{a^2\sin^2 m\cos^2 m}\{E(m)-\cos^2 mF(m)\}. \tag{B14}$$

For $0\leq\tau\ll a^2$ we find

$$G(\tau)=\frac{bGM}{a\sqrt{\tau}}+\mathrm{O}(1/\tau). \tag{B15}$$

For numerical calculations of $G(\tau)$ and $G'(\tau)$ it is useful to rewrite the integrals by the substitution $\sin t=b/\sqrt{u+b^2}$. Then

$$G(\tau)=4G\Sigma_0 ab^3\int_0^{\pi/2}\frac{1}{b^2+(\tau-b^2)\sin^2 t}\times\frac{dt}{\sqrt{b^2+(a^2-b^2)\sin^2 t}}. \tag{B16}$$